

MEMS Generator Study for an Embedded Energy Harvesting System

THÈSE N° 8380 (2018)

PRÉSENTÉE LE 16 FÉVRIER 2018

À LA FACULTÉ DES SCIENCES ET TECHNIQUES DE L'INGÉNIEUR
LABORATOIRE D'ACTIONNEURS INTÉGRÉS
PROGRAMME DOCTORAL EN ROBOTIQUE, CONTRÔLE ET SYSTÈMES INTELLIGENTS

ÉCOLE POLYTECHNIQUE FÉDÉRALE DE LAUSANNE

POUR L'OBTENTION DU GRADE DE DOCTEUR ÈS SCIENCES

PAR

Jasha POLIAKINE

acceptée sur proposition du jury:

Prof. J. A. Schiffmann, président du jury
Prof. Y. Perriard, Dr Y. R. C. Civet, directeurs de thèse
Prof. B. Dehez, rapporteur
Dr E. Onillon, rapporteur
Dr D. Briand, rapporteur



ÉCOLE POLYTECHNIQUE
FÉDÉRALE DE LAUSANNE

Suisse
2018

It's a dangerous business, Frodo, going out your door... You step into the Road, and if you don't keep your feet, there is no knowing where you might be swept off to.

— *Gandalf the Grey*

A mia moglie e ai nostri figli, quelli che sono e quelli che verranno

Remerciements

Cette thèse représente le point d'arrivée d'un chemin de croissance humaine et professionnelle qui a duré quatre ans et demi, un chemin qui n'aurait pu être entrepris sans la contribution de nombreuses personnes.

Tout d'abord, je tiens à remercier Yves pour la chaleur avec laquelle il m'a accueilli dans son groupe et la confiance qu'il m'a toujours témoignée tout au long de la thèse - y compris les phases les plus critiques - en soutenant pleinement mon travail tout en me laissant en même temps une grande autonomie. Sa capacité extraordinaire de motiver et susciter l'esprit de collaboration chez ses collaborateurs est un talent inestimable qui sera bien difficile à retrouver dans ma vie professionnelle. Je voudrais également remercier Yoan pour l'immense quantité de temps qu'il m'a consacré, avec un soutien quotidien technique et scientifique, mais aussi et surtout humain: son engagement a largement dépassé sa fonction de co-directeur de thèse.

Un grand merci également à Paolo, pour son énorme disponibilité à trouver des solutions créatives et efficaces pour toute expérience ou mesure, et à Christian pour avoir toujours partagé son énorme expérience dans le domaine des machines électriques. Sans oublier Magda et Myriam, pour leur patience et leur efficacité.

Il faut aussi mentionner tous les collègues qui, selon un parcours plus ou moins long, ont fait partie de l'équipe du LAI, et avec qui j'ai partagé des moments inoubliables: Omar, Daniel, Chris, Tophe, François, Romain, Dan, Xinchang, Cécile, Florian, Jonathan, Louis, Guillaume, Douglas, Patricio, Sean et Raphaël. Merci à vous tous!

Finalement, je voudrais remercier ma famille du fond de mon cœur. Mes parents Miki et Patrizia et ma sœur Mila, pour l'incommensurable quantité d'amour et le soutien inconditionnel qu'ils m'ont toujours donné malgré la distance physique. Ma femme Letizia, qui a rendu tout cela possible en me soutenant sans relâche jour par jour, de toutes les manières possibles. Enfin, le petit Aron, notre rayon de soleil qui avec ses sourires et sa joie de vivre remplit nos journées de lumière.

Ringraziamenti

Questa tesi rappresenta il punto di arrivo di un percorso di crescita umana e professionale durato quattro anni e mezzo, un percorso che non sarebbe stato possibile intraprendere senza il contributo di moltissime persone.

In primo luogo, vorrei ringraziare Yves per il calore con cui mi ha accolto nel suo gruppo e la fiducia che ha sempre riposto in me durante tutto lo svolgimento della tesi -comprese le fasi più critiche- supportando pienamente il mio lavoro e lasciandomi allo stesso tempo una grande autonomia. La sua straordinaria capacità di motivare e suscitare spirito di collaborazione nei suoi collaboratori è una dote impagabile che ben difficilmente avrò modo di apprezzare ancora nella mia vita professionale. Vorrei inoltre ringraziare Yoan per la mole immensa di tempo che mi ha dedicato, supportandomi quotidianamente a livello tecnico e scientifico, ma anche e soprattutto umano: il suo coinvolgimento ha largamente ecceduto la sua funzione di codirettore di tesi.

Un sentito ringraziamento va inoltre a Paolo, per la sua enorme disponibilità a trovare soluzioni creative ed efficaci per ogni esperimento o misura, e a Christian per aver sempre condiviso la sua enorme esperienza nel campo delle macchine elettriche. Senza dimenticare Magda e Myriam, per la loro pazienza ed efficienza.

Come non menzionare poi tutti i colleghi che, secondo un percorso più o meno lungo, hanno fatto parte della squadra del LAI, e con i quali ho condiviso momenti indimenticabili: Omar, Daniel, Chris, Tophe, François, Romain, Dan, Xinchang, Cécile, Florian, Jonathan, Louis, Guillaume, Douglas, Patricio, Sean et Raphaël. Grazie a tutti voi!

Infine, vorrei ringraziare dal più profondo del cuore la mia famiglia. I miei genitori Miki e Patrizia e mia sorella Mila, per la quantità incommensurabile di amore ed il supporto incondizionato che mi hanno sempre dato e che continuano darmi nonostante la lontananza fisica. Mia moglie Letizia, che ha reso possibile tutto questo sostenendomi senza sosta ogni singolo giorno, in ogni modo possibile. E, infine, il piccolo Aron, il nostro raggio di sole che con i suoi sorrisi e la sua gioia di vivere riempie di luce le nostre giornate.

Abstract

This work has been triggered by an industrial project targeting the development of a novel regulation system for a mechanical watch. Mechanical watches have been known for over a century as one of the finest example of energy autonomous devices, embodying an exceptional amount of human knowledge and high craftsmanship. Nevertheless, the accuracy of a mechanical timepiece keeps being significantly lower with respect to a quartz watch powered by a chemical battery. The aim of the study is thus filling such gap without compromising energy independence.

The new regulation concept revolves around a small scale electromagnetic generator, the development of which is severely constrained at different levels. A major key point is miniaturization, which is needed in order allow the embedding of the generator in a watch movement. In fact, the overall size of the generator falls in the millimeter range, while some inner features might reach a micrometric critical dimension. A first important consequence is that not all the mathematical models that are used for conventional scale applications are suitable when it comes to the design of small scale devices. Another fundamental aspect concerns the technology associated to the fabrication of the device, which heavily affects the solutions that can actually be considered. In this sense, the adoption of the ensemble of the latest MEMS (acronym for Micro Electro-Mechanical System) technologies plays a fundamental role. The research presented within this thesis aims to address such topics in the most comprehensive way as possible, with the ambition of providing scientific tools of general use.

After a brief review of the state of art in the vast domain of microscale power generation, an electromechanical model for the time-dependent description of the dynamics of synchronous machines is derived. In this context, the main issues associated with size reduction are discussed in detail, with a particular emphasis on how the manufacturing technique affects the overall functionality of this class of devices. The model is then refined accordingly and used for the analysis of an existing MEMS machine. Then, the design of the MEMS generator for the watchmaking application is addressed. On the basis of the theoretical structure defined, an algorithm is conceived in order to perform the optimization of the device. The dissertation will then digress on the modeling and manufacturing of single layer planar coils. In this framework, two different fabrication

processes, based on copper and aluminum respectively, are explored and the limits of each technology are compared. The experimental data resulting from this pilot study are then used for finalizing the design of the MEMS generator, in particular by determining the most suitable configuration among the ones identified by the optimization routine. The last part of the thesis will be dedicated to the fabrication and characterization of a functional prototype. In order to pursue this objective, the copper process that was already used for the single layer planar coils is upgraded for enabling the manufacturing of multilayer structures. Morphological and electrical measurements will be performed throughout all the fabrication process as well as on the final prototype.

Key words: MEMS, generator, microfabrication, copper, aluminum, energy harvesting, electromechanical modeling, coils.

Résumé

Ce travail de thèse a été initié dans le cadre d'un projet industriel visant le développement d'un nouveau système de régulation pour une montre mécanique. Depuis plus d'un siècle, les montres mécaniques sont connues comme de remarquables exemples de dispositifs énergétiquement autonomes, incarnant une quantité exceptionnelle de connaissances humaines. Néanmoins, la précision de ces pièces d'horlogerie reste nettement inférieure à celle d'une montre à quartz alimentée par une batterie chimique. Le but de l'étude est donc d'ajuster cette différence sans compromettre l'indépendance énergétique.

Le nouveau concept de régulation est basé sur un générateur électromagnétique dont le développement est soumis à des fortes contraintes sur plusieurs niveaux. La difficulté majeure est la miniaturisation qui est nécessaire pour permettre l'intégration du générateur dans un mouvement horloger. En effet, la taille globale du générateur se trouve dans la plage millimétrique, tandis que certains composants internes peuvent atteindre des dimensions micrométriques. La première conséquence importante est que tous les modèles mathématiques utilisés pour les applications conventionnelles doivent être adaptés à la conception de dispositifs de petite taille. Un autre aspect essentiel est la technologie associée à la fabrication du générateur qui affecte fortement les solutions réellement envisageables. En ce sens, l'adoption de l'ensemble des dernières technologies MEMS (Micro Electro-Mechanical System) joue un rôle fondamental. La recherche présentée dans le cadre de cette thèse vise à aborder ces sujets de la manière la plus complète possible avec l'ambition de fournir des outils scientifiques à usage général.

Après un bref rappel de l'état de l'art concernant la génération électrique à petite échelle, un modèle électromécanique pour la description de la dynamique des machines synchrones dans le domaine du temps est proposé. Dans ce contexte, les principaux problèmes liés à la réduction de taille sont discutés en détail, avec un accent particulier sur la manière dont la technique de fabrication affecte la fonctionnalité de cette catégorie d'appareils. Le modèle est ensuite affiné en conséquence et utilisé pour l'analyse d'une machine MEMS existante. Ensuite, la conception du générateur MEMS pour l'application horlogère est abordée et sur la base de la structure théorique définie, un algorithme est implémenté pour effectuer le dimensionnement. Le travail

porte ensuite sur la modélisation et la fabrication de bobines planaires avec une seule couche de conducteur. Dans ce cadre, deux procédés de fabrication différents, basés respectivement sur le cuivre et l'aluminium, sont explorés et les limites de chaque technologie sont comparées. Les données expérimentales issues de cette étude pilote sont ensuite utilisées pour finaliser l'optimisation du générateur, notamment en déterminant la configuration la plus appropriée parmi celles préliminairement identifiées par l'algorithme. La dernière partie de la thèse est consacrée à la fabrication et à la caractérisation d'un prototype fonctionnel. Afin de poursuivre cet objectif, le processus basé sur le cuivre, déjà utilisé pour les bobines planaires, est amélioré pour permettre la fabrication de structures comprenant plusieurs couches de métal. Des mesures morphologiques et électriques sont effectuées tout au long du processus de fabrication ainsi que sur le prototype final intégré dans son mouvement horloger.

Mots clés: MEMS, générateur, microfabrication, cuivre, aluminium, systèmes autonomes, modélisation électromécanique, bobines.

Contents

Abstract (English/Français)	v
List of figures	xiii
List of tables	xvii
1 Introduction	1
1.1 Context and motivation	2
1.1.1 Escapement systems in mechanical watches	3
1.1.2 Novel regulation method	5
1.1.3 Industry oriented applications	6
1.2 An introduction to power generation at small scale	7
1.2.1 General Applications	7
1.2.2 Mechanical to electrical energy conversion	7
1.3 Choice of the solution	14
1.4 Content of the thesis	15
2 Modeling of MEMS synchronous machines	17
2.1 Conceptual modeling of electromechanical systems	18
2.2 Evolution equations for synchronous machines	19
2.2.1 Hamilton's principle and Lagrange's formulation	19
2.2.2 Energy expressions for synchronous machines	21
2.2.3 Derivation of the equations	25
2.2.4 Physical interpretation	28
2.2.5 Extension to multi-phase machines	29
2.2.6 Advantages and drawbacks	30
2.3 Scaling laws and MEMS devices	31
2.3.1 Design problem	31
2.3.2 Mechanical parameters	32
2.3.3 Electrical and magnetic parameters	32
2.3.4 Functional implications	37
2.4 Practical application	37
2.4.1 Description of the device	38

Contents

2.4.2	Evolution equations	38
2.4.3	Parameters evaluation	40
2.4.4	System simulations	43
2.4.5	Measurements and comparison	47
2.5	Summary and conclusion	48
3	MEMS Generator for the regulation of a mechanical movement	51
3.1	Technical requirements	52
3.2	Preliminary design choices	53
3.2.1	Generator features	53
3.2.2	Single-phase vs three-phase	56
3.2.3	Controlled state simulation	60
3.3	Optimization	62
3.3.1	Construction parameters	62
3.3.2	Definition of the objective function	64
3.3.3	Optimization variables	67
3.3.4	Variables reduction	68
3.3.5	Optimization routine	70
3.3.6	Evaluation domain	72
3.3.7	Inner and outer radius	73
3.3.8	Flux linkage and resistance	74
3.3.9	Electromagnetic torque	76
3.4	Summary and conclusion	78
4	Modeling and manufacturing of single layer planar coils	79
4.1	Applications of small scale inductors	80
4.2	Design	81
4.2.1	Definition of the objective function	81
4.2.2	Lumped element models	81
4.2.3	Analytic formulas	82
4.2.4	Influence of interwinding spacing	84
4.2.5	Finite element simulations	84
4.2.6	Evaluation domain	86
4.2.7	Results and comparison	86
4.3	Fabrication	89
4.3.1	Aluminum vs Copper	89
4.3.2	Copper based process	90
4.3.3	Aluminum process	96
4.3.4	Key aspects and comparison	98
4.4	Characterizations and Measurements	100
4.4.1	Fabrication results	100
4.4.2	Electrical measurements	103
4.4.3	Comparison with previous works	105

4.4.4 Additional indicators evaluation	106
4.5 Summary and conclusion	107
5 MEMS generator prototyping	109
5.1 Choice of the fabrication method	110
5.2 Multilayer coils fabrication	111
5.2.1 Design modifications	111
5.2.2 Connection scheme	113
5.2.3 Wafer layout	114
5.2.4 First layer measurements	115
5.2.5 Updated process flow	118
5.2.6 Second Layer measurements	123
5.3 Stator Liberation	124
5.4 Assembly and Measurements	129
5.4.1 Flexible PCB	130
5.4.2 Rotor	131
5.4.3 Induced voltage	132
5.4.4 Comparison with previous work	134
5.5 Summary and conclusions	135
6 Conclusions and perspectives	137
6.1 Original contributions	138
6.2 Outlook	140
A Proximity effects in MEMS conductor	143
B Single and double yoke configuration - Field lines distribution	145
C Equivalent magnetic circuit	147
Nomenclature	151
Bibliography	157
Curriculum Vitae	169

List of Figures

1.1	Exploded components of a mechanical watch [enc06].	3
1.2	Kinematics of a swiss lever escapement [RBSB17].	4
1.3	Energy flow in a mechanical watch.	4
1.4	Replacement of the traditional escapement with an electronic system.	6
1.5	Novel electronic escapement operating principle.	6
1.6	Different geometries for electrostatic capacitors: (a) in-plane overlap [MMA ⁺ 01], (b) in-plane gap closing [DJJ ⁺ 05] and (c) out-of-plane gap closing [TKK ⁺ 02].	9
1.7	Rotating electret generators by (a) Jefimenko [JW78] and (b) Boland [BCST03].	9
1.8	Schematic of a cantilever piezoelectric generator [RW04].	11
1.9	Compressive load piezoelectric generators from (a) [KKPG98] and (b) [SP01].	11
1.10	Electromagnetic generators with different geometries: (a) bending cantilever [EhGJW ⁺ 01], (b) vibrating membrane [ACN ⁺ 05], (c) movable coil [BTK ⁺ 04].	13
1.11	The small scale synchronous generator by [DAZ ⁺ 05].	13
2.1	Conceptual flow for the modeling of synchronous machines at small scale.	18
2.2	Schematic of a single-phase synchronous machine.	21
2.3	Example of a synchronous machine.	22
2.4	Functional scheme of a single phase synchronous rotating machine	22
2.5	Linear development of a single-phase synchronous machine.	27
2.6	Functional scheme of three phase synchronous rotating machine.	29
2.7	Homotetic size reduction for a factor $k = 2$	33
2.8	Cross section of a three turns coil with different magnetic paths: (a) full circuit , (b) circuit with air gap, (c) ferromagnetic core, (d) air.	36
2.9	The PM synchronous generator by Merzaghi <i>et al.</i> [MKP09, KMP10, MKP11]: schematic outlook (a), full microfabricated stator (b), detail of one copper coil (c).	39
2.10	Flux linkage between the magnet and the coils (one phase)	43
2.11	Rotor speed (open circuit)	44
2.12	Induced voltages for the three phases (open circuit)	45

List of Figures

2.13	Electromagnetic couple (short circuit)	46
2.14	Rotor speed (short circuit)	46
2.15	Induced voltages for the three phases (short circuit)	47
2.16	Induced voltages at different velocities for one phase (timescale for reference only)	47
3.1	Retained solution: rotational electromagnetic generator with PMs as the primary excitation source.	53
3.2	Rotor yoke and its ring shaped permanent magnet with alternating axial magnetization.	54
3.3	Possible rotor configuration: (a) single yoke and (b) double yoke.	54
3.4	Magnetic induction in the air gap ($300\ \mu\text{m}$) for single and double yoke systems ($p = 3, B_0 = 1.2\ \text{T}$).	55
3.5	Wire bonder manufacturing technique [BKB ⁺ 09]: (a) copper conductor wiring and (b) a completed coil.	55
3.6	Schematic of a multilayer coil.	56
3.7	Simulated rotor speed for the two configurations: (a) single-phase and (b) three-phase.	59
3.8	Simulated back EMF for the two configurations: (a) single-phase and (b) three-phase.	59
3.9	Simulated electromagnetic torque for the two configurations: (a) single-phase and (b) three-phase.	60
3.10	Controlled behavior and targeted speed.	61
3.11	Cross section of the rotor and main construction parameters.	63
3.12	Shape of a planar coil (one layer).	64
3.13	Cross section of two adjacent turns.	64
3.14	Optimization routine.	72
3.15	Superposition of one magnet pole and a coil sector.	73
3.16	Total flux linkage for different values of the stator outer radius.	74
3.17	Flux linkage (sector) as a function of the number of turns for the three coils configurations.	75
3.18	Conductor length (sector) as a function of the number of turns for the three coils configurations.	75
3.19	Electromagnetic torque (sector) as a function of the number of turns for the three coils configurations.	77
4.1	Schematic of a square planar inductor (adapted from [MdmHBL99]).	83
4.2	Number of turns as a function of turns spacing for different χ values ($d_{out} = 3\ \text{mm}, d_{in} = 300\ \mu\text{m}$).	85
4.3	Self-inductance as a function of turns number according to the three analytic formulas and FEM: (a) type A coils, (b) type B coils.	87
4.4	Relative error between FEM data and analytic formulas for a type A coil with conductor width and spacing equal to $2\ \mu\text{m}$	88

4.5	Schematic of the Cu process flow: (a) 150 nm Al + 10 μm PI + 200 nm SiO_2 deposition on Si substrate, (b) PI mold structuration, (c) 40 nm Ta + 350 nm Cu deposition, (d) Cu electroplating, (e) CMP + IBE cleaning.	90
4.6	PI etching: (a) properly etched trenches, (b) deformed trenches due to overetch, (c) complete deterioration of the insulating material.	92
4.7	Shadowing effect of the SiO_2 cap.	93
4.8	Incomplete filling of the PI after electroplating, caused by poor seed layer step coverage.	94
4.9	Optical profiler measurement performed on a B type coil after the seed layer deposition.	94
4.10	Operating principle of CMP (from [JKKCKH ⁺ 12]).	95
4.11	Detail of a coil surface (a) before and (b) after IBE cleaning.	96
4.12	Aerial view of a finished copper coil.	96
4.13	Schematic of the Al process flow: (a) Sputtering of 8 μm Al, (b) lithography on 10 μm thick resist AZ9260, (c) deep ICP etching and resist stripping.	97
4.14	Peripheral turns after Al etching: (a) without filler and (b) with filler.	98
4.15	Aerial view of a finished aluminum coil.	99
4.16	Effect of etching anisotropy on the two process flows.	100
4.17	FIB cross sections of completed copper coils with nominal lines widths equal to 2 μm (a) and 3 μm (b).	101
4.18	Thickness measurement on a completed type B coil with nominal lines width equal to 7 μm lines: (a) 3D optical profilometry and (b) SEM measurement,	102
4.19	Detail of a completed type B coil with nominal lines width equal to 9 μm	102
4.20	Reference circuit for electrical measurements.	103
4.21	Volumic inductance density (VID) in $\text{mH}\cdot\text{mm}^{-3}$ and inductance to resistance ratio (IRR) in $\mu\text{H}\cdot\Omega^{-1}$ for the type A and type B completed coils.	107
5.1	Omnidirectional copper growth during electroplating: (a) early stages, (b) filling of smaller gaps.	112
5.2	Modification of the connection pad by introducing PI structures.	113
5.3	A completed pad (first layer) including PI pattern.	113
5.4	Stator coils layout: (a) first and (b) second layer.	114
5.5	Stators disposition on the surface of the 100 mm wafer.	115
5.6	Electric resistance (Ω) for the first layer coils (green = functional value, red = too high, yellow = too low).	116
5.7	Loss of electrical contact due to defective PI mold.	117
5.8	Examples of defects leading to short circuits: (a) mechanical deformed insulation and (b) residual copper after CMP.	118

List of Figures

5.9	Schematic of the Cu process flow: (a) Deposition and wet etching of 200 nm Ti, (b) 2 μm SiO_2 deposition and etching, (c) 4.5 μm PI + 200 nm SiO_2 deposition, (d) PI mold structuration, (e) 40 nm Ti + 250 nm Cu deposition, (f) Cu electroplating, (g) CMP + IBE cleaning.	119
5.10	Delamination and redeposition defects after Ti liftoff.	120
5.11	Ti cap over interconnection pads: (a) coil and (b) test structures.	120
5.12	FIB cross section of the 2nd layer polyimide mold.	122
5.13	2nd layer connection pad and underlying Ti VIA.	122
5.14	Shift between first and second level turns.	123
5.15	2nd layer after IBE cleaning: (a) connection pad and (b) pattern detail.	123
5.16	Cross section of a 2-layer stator after IBE.	124
5.17	Electric resistance (Ω) for the second layer coils (green = functional value, red = too high, yellow = too low).	124
5.18	Extended process flow for stators liberation: (a) Deposition and wet etching of 200 nm Ti, (b) 2 μm SiO_2 deposition and etching, (c) 1 μm SiO_2 deposition, (d) Plasma etching of 3 μm SiO_2 + 4.5 μm PI + 2 μm SiO_2 + 10 μm PI + 150 nm Al (or SiO_2), (e) DRIE of $\sim 90 \mu\text{m}$ Si, (f) Plasma etching of 1 μm SiO_2 , (g) Backside grinding.	125
5.19	Protective SiO_2 layer: (a) aerial view and (b) FIB cross section.	126
5.20	Principle of Dicing Before Grinding (source: https://www.disco.co.jp/).	128
5.21	Completed stators after Si etch: (a) borders and (b) center.	128
5.22	Completed stators with adhesion layers in SiO_2 (left) and Al (right).	129
5.23	Stator glued to flexible PCB: (a) complete view and (b) detail.	130
5.24	Rotor configuration: (left) model version and (right) prototype version.	131
5.25	Generator assembled into the watch movement: (a) complete view and (b) detail.	131
5.26	Example of induced voltage measurement.	132
5.27	Phase constant extrapolation from back EMF measurements.	133
5.28	Magnetic induction in the air gap for three different misalignment values (FEM).	134
5.29	Flux linkage as a function of the rotor angular position for a 40° misalignment between the magnets.	135
A.1	Effect of frequency on current distribution: (a) DC, (b) 10 kHz, (c) 5 MHz, (d) 1 GHz.	144
B.1	Distribution of the induction field for two axial flux generator configurations: (a) single yoke and (b) double yoke.	145
C.1	Upper view and cross section of a double yoke generator	147
C.2	Equivalent magnetic circuit.	148
C.3	Simplified magnetic circuit (I).	148
C.4	Simplified magnetic circuit (II).	149

List of Tables

2.1	Model parameters	32
2.2	Generator Parameters	41
2.3	Phase self and mutual inductances (μH)	41
2.4	Torque measurements	42
2.5	Phase constant at different speeds	48
3.1	Technical requirements	52
3.2	Entry values for preliminary simulations	58
3.3	Updated functional constraints	62
3.4	Rotor construction parameters	63
3.5	Stator construction parameter	64
3.6	Significant priority coefficients combinations	66
3.7	Evaluation domain	73
3.8	Phase constant optimization	76
3.9	Electromagnetic torque optimization	77
4.1	Significant priority coefficients combinations	81
4.2	Coils configurations features	86
4.3	Optimal number of turns	89
4.4	Fabrication results for Cu/PI coils	100
4.5	Fabrication results for Al coils	101
4.6	DC Resistance Measurements	103
4.7	Inductance Measurements	104
4.8	Inductance density	105
4.9	Inductance density comparison with previously published inductors	106
5.1	Electromagnetic torque optimization results (updated)	110
5.2	Phase constant comparison with previously published works	135

1 Introduction

The research pursued within this thesis work was largely inspired by a project situated in the domain of watchmaking industry. This chapter will clarify the context and present the operating principle of traditional escapement systems in mechanical watches. Thereafter, a novel regulation method conceived to increase the accuracy of such devices will be presented. Since the new regulation method revolves around the generation of power at small scale, the discussion will then focus on the main solutions that are currently adopted in this broad research field. In particular, the main transduction principles exploited for the conversion from mechanical to electrical energy will be revised.

1.1 Context and motivation

The market of timepieces mainly consists of two broad categories of products: mechanical and quartz watches. The first ones appeared early in history. Rudimentary examples of fully mechanical apparatuses for time measurement date back to the 13th century [Hea02], while the first modern watches became widespread in the second half of the 19th, particularly after the invention of the *swiss lever escapement* in 1860. Quartz watches, on the other hand, entered the mass market in the 70s. These were (and are) essentially electronic devices supplied by a chemical battery, providing higher accuracy with respect to their mechanical counterparts at significant lower costs and need for maintenance. Despite the economic upheavals initially caused by the introduction of quartz watches, mechanical ones didn't cease to exist and nowadays the two products have balanced market shares, with many active brands on both sides.

In this context, the project that triggered this thesis work, aimed to enhance the accuracy of a mechanical timepiece up to the level of a quartz one, while still keeping the watch without any external power source. As will be detailed in the following paragraphs, this goal will be pursued by replacing the so called escapement system, which regulates the pace of mechanical watches, with a novel semi-autonomous regulation method based on the implementation into the watch movement of a small scale electric generator coupled to an electronic command. While the design of the electronics does not appear a major issue, the demanding requirements make the conception and the design of the generator a challenging task. Such will be the focus of this dissertation.

Within the described project scenario, many lines of research can be identified, mostly related to the constraints imposed by the specification of the project itself. First of all, the system is aimed to be embedded in a watch movement. It is thus evident how miniaturization is a key point to fulfill this requirement. In fact, while the overall size of the generator falls in the millimeter range, some inner features might reach a critical dimension closer to the micron scale (devices in this size range will later on be referred to as "small scale"). A first important consequence is that not all the mathematical models that are used at macro scale are suitable when it comes to the design of a small scale device. A great attention must thus be paid to the formulation of the appropriate models and the related optimization strategies. A second important consequence that is also strongly related to miniaturization, concerns the fabrication of the device. In this sense, the adoption of the ensemble of the latest MEMS (acronym for Micro Electro Mechanical System) technologies plays a fundamental role. Process optimization in order to ensure high precision, stability and reproducibility, is another main focus of the thesis. In this sense the novelty of this research should not be sought in the principle of power generation itself, which is in general well-known, but rather on its transfer at small scale from both a functional and technological point of view.

1.1.1 Escapement systems in mechanical watches

To understand the role covered by the new regulation system, it is important to fathom the basic working principle of a mechanical watch. The main components are represented in Figure 1.1. The primary source of energy is the mainspring, which is usually shaped in a spiral form and can be charged both manually, by turning the winding pinion, or automatically by exploiting the oscillations of a seismic mass (this is the standard in modern mechanical watches). A set of rotating gears connects the main spring to the center wheel, so that a torque can be transmitted to both the display (the clock hands) and the escapement wheel. The latter is connected to an oscillating system (balance wheel and hairspring) via an anchor lever including pallets. The ensemble of these components form the escapement system. The kinematics of the escapement can be grasped in Figure 1.2, which represents a swiss lever escapement, a widely used solution in watchmaking industry. When the escape wheel receives the torque from the gearing, free rotation is prevented by one of the anchor pallets (entrance pallet) so that the mechanical action is transmitted to the oscillating system instead. Once the latter is put into motion, the peculiar design causes the blocking pallet to disengage. This enables the rotation of the escapement wheel, which stops when the exit pallet of the lever engages another teeth. The cycle then repeats itself, the final result being that the pallets curb the escape wheel, only allowing a step-like rotation. Since the oscillating system is designed to resonate at very specific frequencies (typically 3 or 4 Hz), the pace of the stepping motion is constrained, which ultimately allows the regulation of the entire movement.

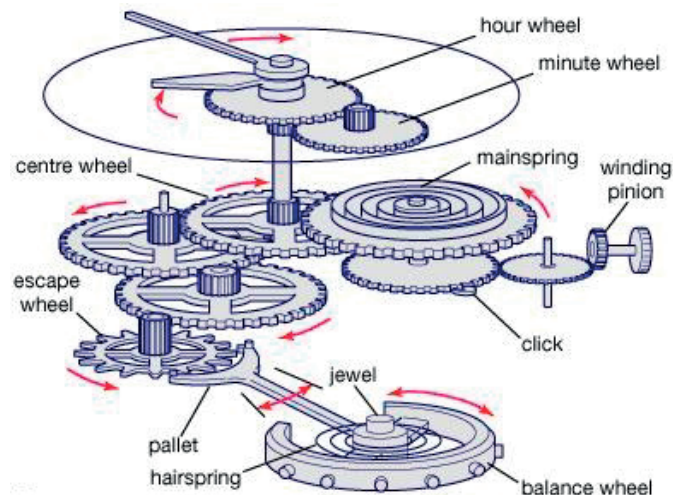


Figure 1.1 – Exploded components of a mechanical watch [enc06].

From a more general perspective, the escapement acts as a feedback regulator. It absorbs energy from the system and gives it back in a properly shaped form (Figure 1.3). This prevents the mainspring from quasi instantaneous discharging and allows

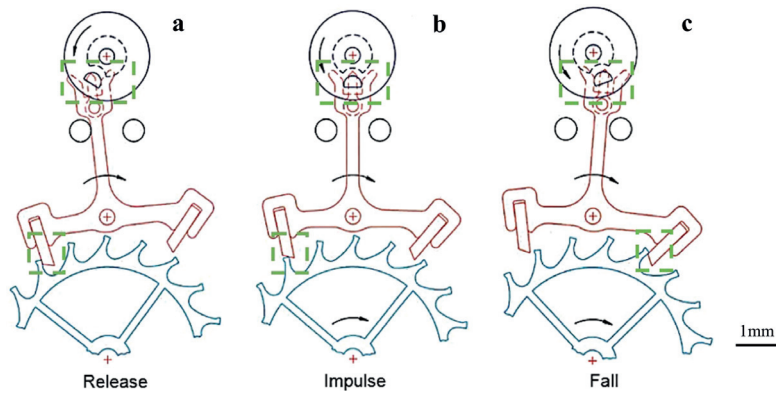


Figure 1.2 – Kinematics of a swiss lever escapement [RBSB17].

the control of the gearing speed. The reliability of the escapement system, which is the main responsible for the overall accuracy of the watch, is highly dependent on the quality of workmanship and the level of maintenance performed. Wear, lubrication and even temperature can affect performances significantly. For the same reasons, and because of the large amount of different timepieces on the market, it is challenging to quantify the average accuracy rigorously. A reasonable estimation is a divergence from the correct time measurement in the range of a few seconds per day. For comparison, a quartz watch has an accuracy in the range of a few seconds per year. As anticipated, a new hybrid system based on the introduction of a command electronics in a mechanical watch will be presented in order to fill this performances gap.

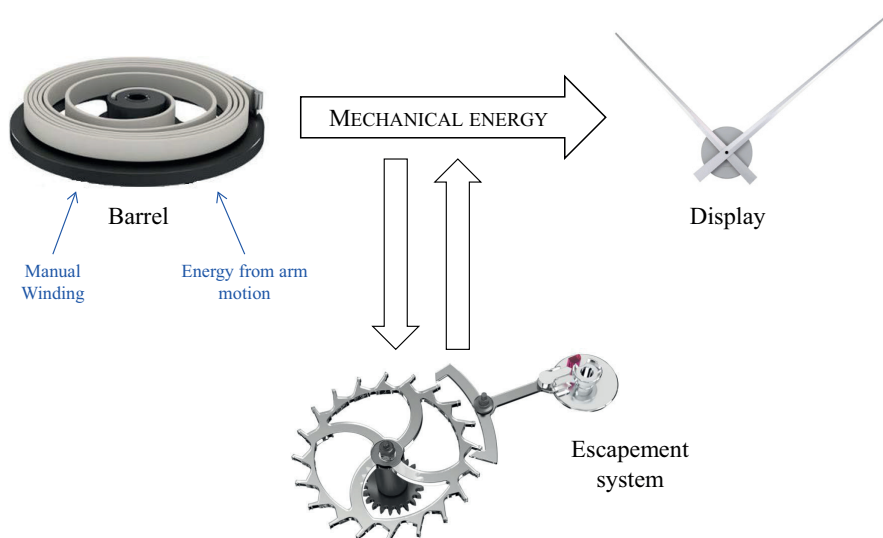


Figure 1.3 – Energy flow in a mechanical watch.

1.1.2 Novel regulation method

The concept for an electronic regulation system implemented in a mechanical watch dates back to the 70s and was originally proposed by Berney [Ber76]. In the configuration envisioned by his author the mechanical energy harvested from the user's movement is still stored in the mainspring and transmitted by the gearing as described in Figure 1.3. However, the escapement wheel and its associated oscillator are replaced with an electrical generator coupled to an electronic circuit (Figure 1.4). The operating principle is schematized in Figure 1.5. The generator converts the mechanical energy received by the gearing into electrical energy, which is subsequently used for supplying the electronic circuit. The electronics performs two basic functions:

- Sensing the rotor speed.
This is done by comparing the frequency of the input signal coming from the generator, which is directly related to the rotor speed, and a reference signal. The latter is provided by a quartz crystal which, once excited, oscillates at a given highly reliable frequency.
- Regulating the rotor speed.
In order to perform such task, the electronic command varies the electric load applied to the generator. If the rotor (and hence, the whole watch gearing) is turning too fast, the load is adjusted so that the power consumption of the system is increased. Since there is no other possibility, this additional energy ends up to be drained from the mechanical energy of the rotor, whose motion is slowed down.

The system described above allows to control the dynamics of a mechanical element (the rotor): in other words it works as an "electronic escapement", where the braking operation is no longer performed by the teeth of the escapement wheel, but by the electronic command instead. With respect to the traditional structure, the main advantage is that the global accuracy of the watch becomes theoretically comparable to the one of a quartz watch since the regulation is managed by an electronic system. This also entails increased reliability and reduced need for maintenance. All of this is accomplished without using a chemical battery, thus keeping the timepiece a mechanical one. Nevertheless, the patent was abandoned after its deposition, probably because the technology of the 70s had not reach a sufficient level of development. In recent years however, the use of MEMS devices has increased exponentially, spreading into various application fields, while at the same time manufacturing costs have kept decreasing. For these reasons, conceiving a MEMS device for this application, could in principle allow to overcome the miniaturization limits of traditional manufacturing approaches.

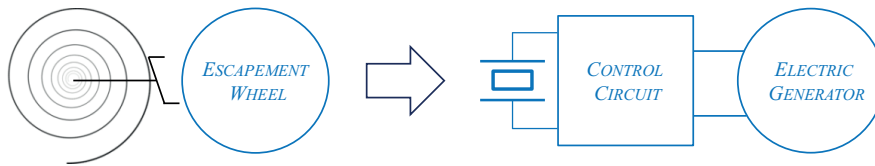


Figure 1.4 – Replacement of the traditional escapement with an electronic system.

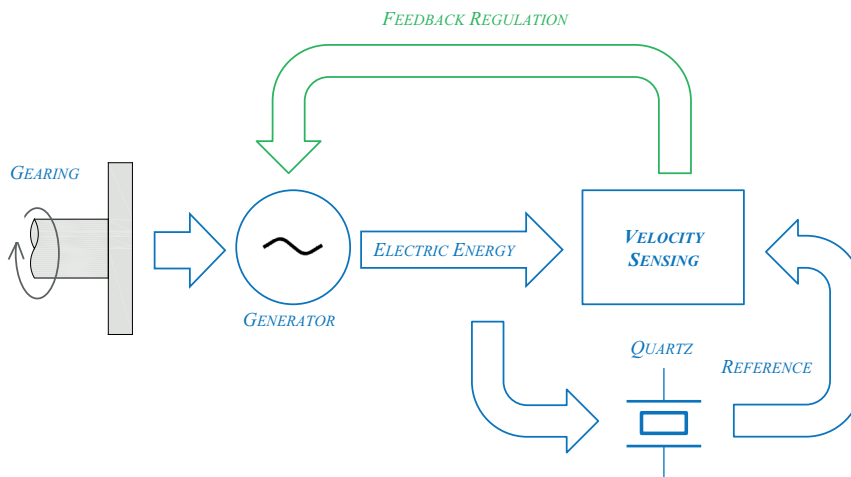


Figure 1.5 – Novel electronic escapement operating principle.

1.1.3 Industry oriented applications

At industrial level, some ideas related to the adjustment of a watch mechanism with an electronic circuit were developed. However, the focus was mainly to remove the battery from a quartz watch rather than improving the accuracy of a mechanical one. As for example, SEIKO patented quartz watches in which the battery is recharged by an electrical generator, which is in turn supplied by the mechanical energy harvested from the user's movements [HK00]. Watches implementing this system (AGS and Kinetic models) have been commercialized since the end of the 80s. Such method extends the battery's life, but it doesn't allow its elimination. Asulab patented a similar technology under the name of autoquartz [BH98]. As for the concept of controlling the movement via a braking system, analogous to the one described in the original patent by Berney, Asulab has deposited various patents which deepen the principle of braking [TT89, BF07]. Richemont filed a patent on this idea as well [MMST14], and pre-industrialized watches that, however, have never been commercialized. At the moment, the only available device on the market exploiting such operating principle is commercialized by Seiko under the name of "Springdrive" [SKN01] and is based on a relatively bulky generator.

1.2 An introduction to power generation at small scale

The device that was developed during this thesis belongs to the broad domain of power generation at small scale. The following sections will therefore provide some general context and briefly revise the main solutions adopted in this field.

1.2.1 General Applications

In recent years, a wide research has been pursued on the subject of electrical power supply for devices where wired sources are not locally available. These include gizmos from the most disparate fields [MYR⁺08], as for example smartphones, GPS instruments, sensors, biomedical components and so on. For these applications, where low power (typically from few nW to mW) is required, chemical batteries have been the primary option so far. These, however, present a number of drawbacks, including miniaturization issues, relatively high cost and need for maintenance in terms of replacement/recharging as well as disposal. This pushed the research towards small scale generators capable of delivering power wirelessly from an active source introduced for this purpose, or even extracting power from the environment (energy harvesting). The primary energy might be available in different forms, practical examples being solar, thermal, electromagnetic or mechanical. This entails that some sort of transduction is needed in order to operate the conversion to electrical energy. A key role in the choice of the most suitable transduction principle, other than the form of the primary energy source, is also played by the fabrication method. In fact, because of the reduced size of these devices, MEMS manufacturing techniques are usually required. Their implementation however, entails a series of technological constraints and might not be straightforward. Motivated readers can refer to the book by Madou [Mad02] for an exhausting compendium on the subject. In the application presented in this thesis, primary energy is available in its mechanical form. Hence, in the following the focus will be on mechanical to electrical power conversion.

1.2.2 Mechanical to electrical energy conversion

In conventional macro scale applications, the vast majority (if not the entirety) of electrical generators is based on electromagnetic transduction. At small scale however, additional techniques become attractive. For example, electrostatic transduction, which is both impractical and inefficient for large machines, becomes much more effective at small scale, where it is also well suited to MEMS implementation. In the same way, piezoelectric transduction is generally impractical for large scale rotating machinery, but it is well suited to the reciprocating nature of motion typically involved, for example, in energy scavenging from vibrations.

Electrostatic generators

A capacitor consists of two metallic surfaces which are electrically isolated from each other by an insulator (typically air or vacuum). The application of a bias voltage V creates equal but opposite charges on the plates, Q . A displacement of the surfaces results in a variation of the electrostatic energy stored in the capacitor. The fundamental definition of the capacitance is thus given by

$$C = \frac{Q}{V} \quad (1.1)$$

The term C can be expressed more explicitly if the geometry of the component is taken into account. In MEMS capacitors, the metallic surfaces are usually parallel plates, for which a very simplified expression of C is given by

$$C = \varepsilon \frac{A}{d} \quad (1.2)$$

where ε is the electrical permittivity of the insulating material between the plates, A is the area of the plates, and d is the separation between the plates. The latter is typically very small in MEMS capacitors, ranging from few nanometers to microns. The energy stored in the capacitor, can be expressed as

$$E = \frac{1}{2}QV = \frac{1}{2}CV^2 = \frac{1}{2} \frac{Q^2}{C} \quad (1.3)$$

As can be seen from equations (1.2) and (1.3), if a variation in the distance between the plates is produced, the amount of electrostatic energy stored in the capacitor is also modified. More specifically, the energy variation is given by the work spent against the electrostatic forces to make the displacement happen. A voltage or charge constrained cycle is then implemented in order to actually harvest the energy difference (see for example [SBS12]). In general, electrostatic generators have high output impedance, which leads to relatively high voltages and limited current supplying capability. The electrostatic concept is easily realizable as a MEMS and much processing know-how exists on the realization of capacitors with multiple geometries. Figure 1.6 reports three different examples of electrostatic generators where the displacement between the charged surface is achieved in different ways.

When no initial polarization source is available, an interesting solution consists in

1.2. An introduction to power generation at small scale

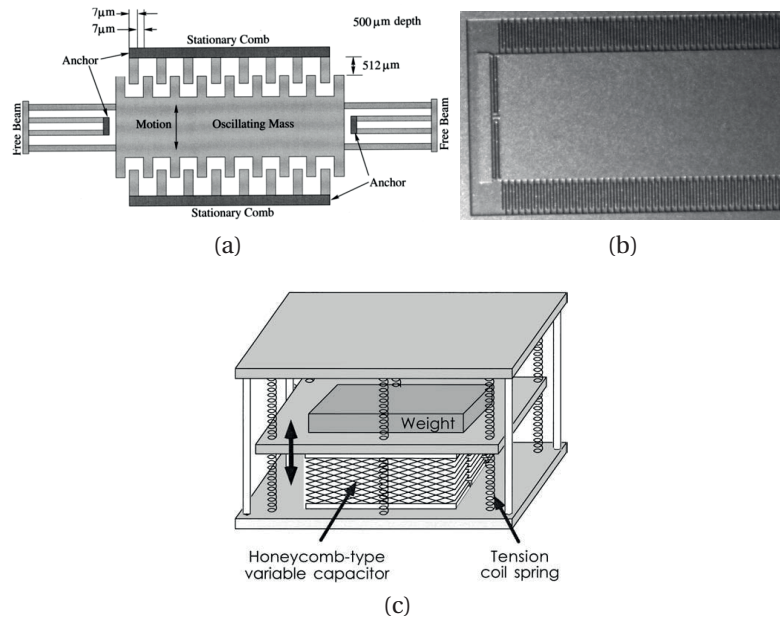


Figure 1.6 – Different geometries for electrostatic capacitors: (a) in-plane overlap [MMA⁺01], (b) in-plane gap closing [DJJ⁺05] and (c) out-of-plane gap closing [TKK⁺02].

using electrets, *i.e.* dielectric materials that, once charged, are capable of holding electric polarization [Tad86]. This concept was also demonstrated for some rotating generators. Significant examples in this sense are the devices by Jefimenko [JW78] and Boland [BCST03], reported in Figure 1.7.

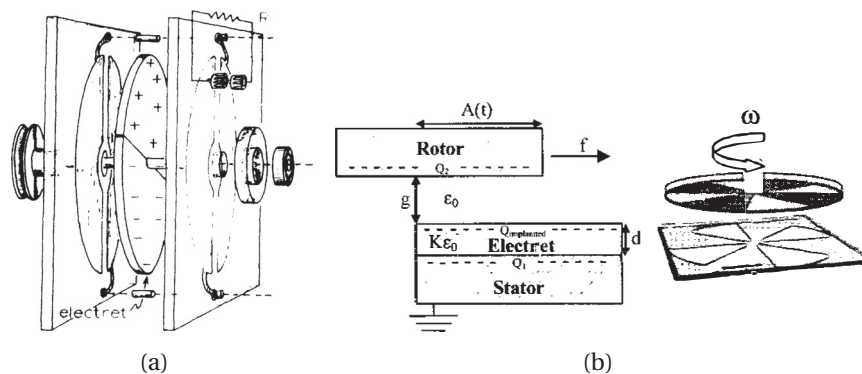


Figure 1.7 – Rotating electret generators by (a) Jefimenko [JW78] and (b) Boland [BCST03].

Piezoelectric generators

Piezoelectric ceramics have been used for many years to convert mechanical energy into electrical energy and vice versa. If certain crystals are subjected to mechanical strain, they become electrically polarized, the degree of polarization increasing with the applied strain. Conversely, it is possible to induce mechanical deformation by applying electric field. Piezoelectric materials typically exhibit anisotropic characteristics, *i.e.* the properties of the material depend upon the direction of applied forces and the orientation of the polarizing electrodes. For this reason, the describing parameters are basically tensorial quantities and they are usually expressed by mean of the notation proposed in [Nye85]. In particular, the level of piezoelectric activity of a material is defined by a series of constants used in conjunction with axes identifiers. These include the piezoelectric constant d , defined by

$$d_{ij} = \frac{\textit{strain developed}}{\textit{applied field}} \quad \textit{or} \quad d_{ij} = \frac{\textit{short circuit charge density}}{\textit{applied stress}} \quad (1.4)$$

where the coefficients i and j index the axes orientation. Another important constant affecting the generation of electrical power is the electromechanical coupling coefficient k . the latter describes the efficiency with which the energy is converted by the material between electrical and mechanical forms in a given direction:

$$k_{ij} = \sqrt{\frac{\textit{mechanical energy stored}}{\textit{electrical energy applied}}} \quad \textit{or} \quad k_{ij} = \sqrt{\frac{\textit{electrical energy stored}}{\textit{mechanical energy applied}}} \quad (1.5)$$

In recent years, a lot of effort has also been focused on the modeling of non-linear effects (see [MPG⁺14] for a review on the subject). Piezoelectricity offers a simple approach to electric generation, since structural strains are directly converted into a voltage output by plating electrodes directly on the material surface. In general, there is no need for complex geometries and the number of additional components is usually limited. Moreover, it is possible to design devices which exploit different strain constants. For example, a widely used architecture is a cantilever structure with piezoelectric material attached to the top and bottom surfaces. One side of the cantilever is clamped on the substrate while the other is left unconstrained, so that the structure operates in bending mode. An example of such a device, originally presented by Roundy [RW04], is reported in Figure 1.8. On the other hand, the devices proposed in [KKPG98] and [SP01] were designed to harvest energy from compressive loads (Figure 1.9).

1.2. An introduction to power generation at small scale

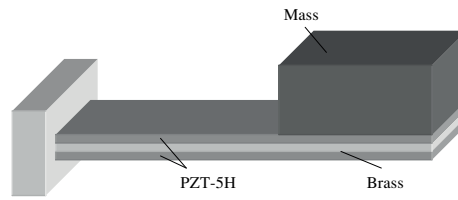


Figure 1.8 – Schematic of a cantilever piezoelectric generator [RW04].

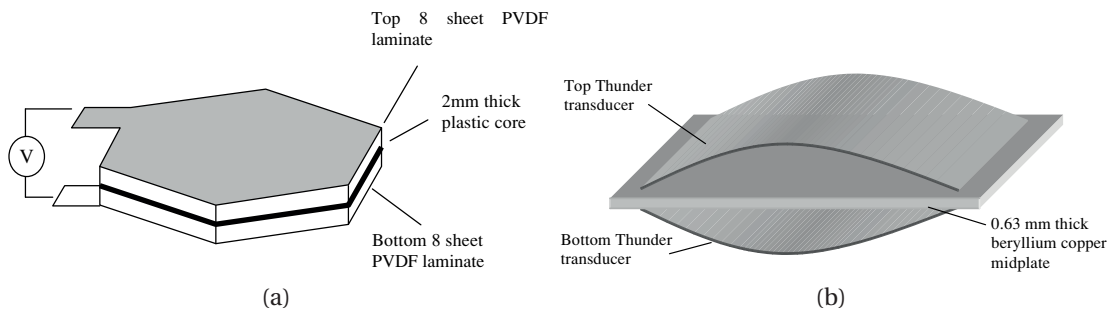


Figure 1.9 – Compressive load piezoelectric generators from (a) [KKPG98] and (b) [SP01].

Piezoelectric generators are simple to fabricate and several processes exist for depositing piezoelectric films (thin and thick). On the other hand, a major drawback is that piezoelectric materials are required to be strained directly and therefore their mechanical properties will limit overall performances as well as lifetime. Another issue is that power efficiency reaches its maximum within a very narrow frequency bandwidth (2 – 4%) around the mechanical resonant frequency of the component and drops dramatically if the excitation falls outside this range. While numerous strategies have been proposed in order to address such matter (as in [GNV09, ETWW11, LBF⁺13]), their application is still limited to the cases in which the mismatch between excitation and resonant frequencies is relatively limited. For these reasons, piezoelectric generators are difficult to adapt to rotating systems, even though some solutions in this sense are reported (see for example [PYH13, JLI⁺15]).

Electromagnetic generators

Electromagnetic induction, first discovered by Faraday in 1831, relates to the generation of a potential difference ΔV in a conductor. This voltage, also called back electromotive force (EMF), is induced whenever there is a time variation of a magnetic flux ψ (which can be generated by magnets or currents) through the surface delimited by the conductor itself. Faraday's law¹, reported below, expresses this concept. The

¹Scientific literature tends to be ambiguous on the law's designation. The author is here making reference to [MS98].

Chapter 1. Introduction

minus sign indicates that the back EMF tends to generate a magnetic field which opposes the variation of the magnetic flux.

$$\Delta V = -\frac{d\psi}{dt} \quad (1.6)$$

In engineering applications, the conductor typically takes the form of a coil. The flux variation can be obtained by a number of techniques, including relative motion between the coil and the source of the magnetic field, variation of the source magnetic field, changes in the magnetic path, etc. The most common strategy at small scale, is to produce a periodic displacement between the coil and a permanent magnet. In this case, the amount of electricity generated depends upon the strength of the magnetic field, the velocity of the relative motion and the coils characteristics. For harvesting energy from vibrations the magnet(s) usually moves together with a resonant structure, while the coil(s) is clamped to the substrate. In such way, when the resonant structure is excited, the displacement is produced and a back EMF is generated as a result. While in principle either the magnet(s) or the coil can be chosen to be the moving element, the magnet(s) is more frequently designated as the moving element. There are basically two reason for this. First, in this way the magnet can also serve as inertial mass. Second, it becomes much more practical to connect the coils to the outside circuitry. As for the resonant structure geometry, a lot of different configurations have been proposed so far. El-Hami [EhGJW⁺01] presented a device comprising a cantilever beam fixed at one end and supporting a pair of NdFeB magnets on a c-shaped core at the free end. The coil is made up of many turns of copper wire and is fixed in position between the poles of the magnets (Figure 1.10(a)). Pérez-Rodriguez [ACN⁺05] proposed an oscillating structure comprising a polyimide membrane, a NdFeB magnet and a planar coil made of a 1.5 μm thick aluminum layer. A cross section can be observed in Figure 1.10(b). Another significant example is the solution investigated by Beeby [BTK⁺04], in which the coil is the moving element. In particular, the coil is located between 4 magnets and moves laterally with respect to them (Figure 1.10(c)).

Electromagnetic transduction is particularly suitable to generate energy from rotating systems. For such applications, miniaturized synchronous generators, which are basically the small scale version of conventional electrical machines, are frequently the solution of choice. A commonly used approach is to use ring shaped magnets over variously arranged microfabricated coils. An example was proposed by Das [DAZ⁺05], who designed a three-phase permanent-magnet generator with eight magnetic poles and multiturn surface windings on a soft magnetic substrate. A conceptual drawing of the device is depicted in Figure 1.11.

In general, devices based on electromagnetic transduction offer a well-established

1.2. An introduction to power generation at small scale

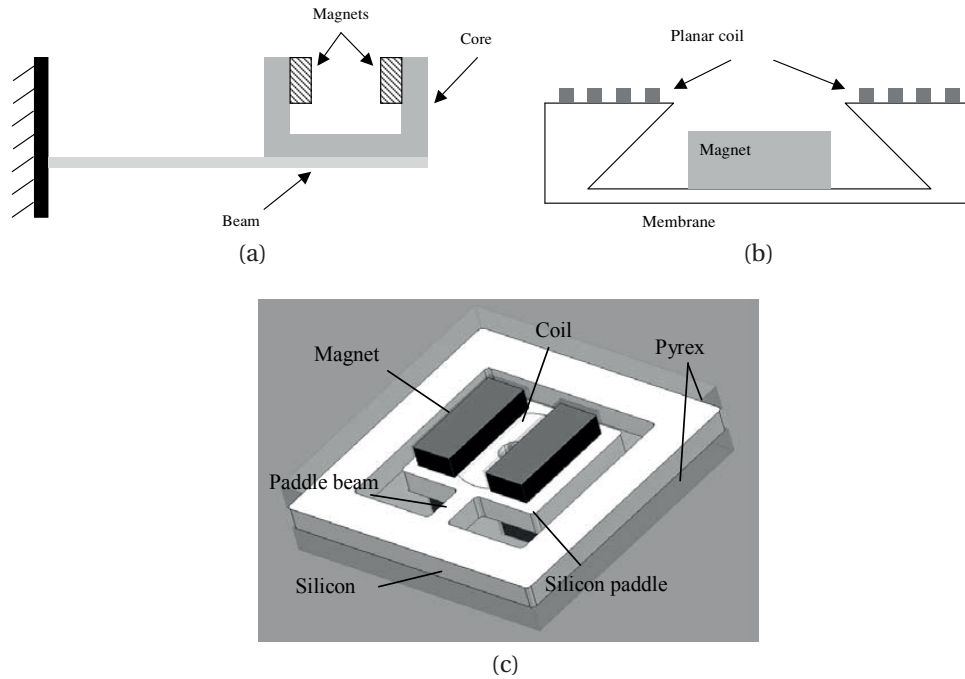


Figure 1.10 – Electromagnetic generators with different geometries: (a) bending cantilever [EhGJW⁺01], (b) vibrating membrane [ACN⁺05], (c) movable coil [BTK⁺04].

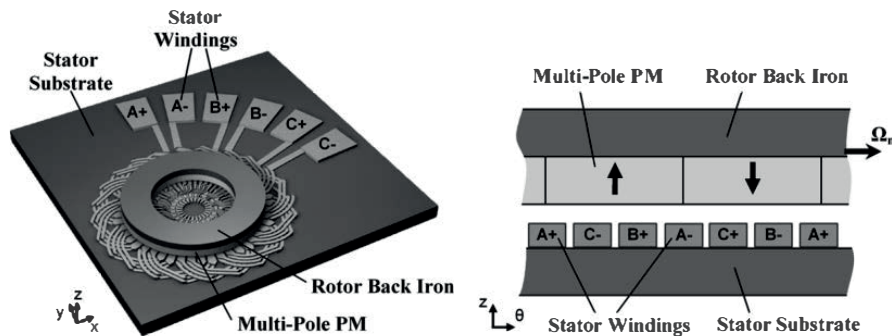


Figure 1.11 – The small scale synchronous generator by [DAZ⁺05].

technique of electrical power generation. However at wafer-scale some issues arise. In particular, obtaining a good magnetic coupling is a challenging task, mainly due to the poor properties of planar magnetic materials, the challenging implementation of ferromagnetic materials and the features of planar coils. All of these aspects will be the object of an extensive discussion in Chapter 2. Finally, it should be clarified that although the concept of the relative motion between magnets and coils is the most common, other electromagnetic conversion systems based on Faraday's law were proposed at small scale. These include reluctant [AKA93, GCS⁺93] and asynchronous [ADC⁺06] devices, which however were developed to operate as actuators rather than generators. More recently, the possibilities of magnetostrictive materials for power

generation were also explored [Zha11]. Nevertheless, the implementation of such materials at MEMS scale is quite difficult.

1.3 Choice of the solution

A feasibility study was carried out in 2013 [Pol13] with the aim to determine the most suitable solution for the conception of the electronic escapement system. In such work, several types of generators, based on different transduction principles and excitation modes, were analyzed. The main conclusions of such study will be here recalled.

- Vibration driven generators in general are impractical due to the fact that the watch gearing produces rotating elements rather than vibrating ones. As a consequence, some sort of system for obtaining the proper excitation mode has to be implemented before even considering the actual generator performances.
- Piezoelectric generators efficiency drops dramatically when they are excited far from the mechanical resonant frequency. In this sense, they are particularly affected by the mismatch between the low targeted speed, which entails low frequencies of excitation, and the reduced size of the device, which results in self resonant frequencies several orders of magnitude higher.
- Electromagnetic and electrostatic generators are more suitable for the application, as they can be arranged in rotating configurations.
- Electrostatic generators requiring an initial polarizing voltage, despite their promising characteristics in terms of output voltage and operational frequency are unsuited for the application, since no external source is available for supplying the initial bias. Using a pre-charged electret material could in principle solve this issue. However, the performances of the device will be highly dependent on the material, whose charge retaining properties are known to decay over time.

Finally, a rotational electromagnetic generator was retained as a solution. With respect to other possibilities, such option presents the advantage of having multiple design parameters that can be exploited for the optimization (*e.g.* coils geometric features). Another significant advantage is that the transduction requires no direct contact between the moving parts nor particular mechanical strain of the active part of generator, the only part subjected to significant mechanical stress being the rotor axis. Finally, keeping the operating principle of a synchronous machine allows the use of an existing electronic command developed by the industrial partner.

1.4 Content of the thesis

This work revolves around the design and the fabrication of a MEMS synchronous generator. Starting from this core, several research lines will be developed and discussed at different levels. The ambition of the thesis is not only to answer to the specific requirements of the application, but also to provide some useful tools of more general use, both in terms of models and technological solutions.

After the preliminary introduction given so far, Chapter 2 will address the derivation of an electromechanical model for the time-dependent description of synchronous machines. This will be done on the basis of very broad definitions and hypotheses. Then, the issues associated with size reduction will be discussed in detail, with a particular emphasis on how the manufacturing technique affects the overall functionality of the device. The analysis will allow to refine the general model for the description of synchronous machines at MEMS scale. In the last section, a study based on an existing MEMS device, will serve as a validation of the theoretical development and will show some possible approaches for the determination of the significant parameters.

Chapter 3 will deal specifically with the escapement application. The technical requirements will be discussed and the model derived in the previous chapter will be used extensively for determining the most suitable configuration. The influence of the different construction parameters will be discussed, and the evaluation domain will be reduced accordingly. Then an optimization routine taking into account the technological constraints will be established and use for the design of the stator coils.

Chapter 4 consists of a study on single layer planar coils, from self-inductance modeling to manufacturing. This study is related to the rest of the dissertation on two levels. First, it will help validating some of the assumptions made during the design. Secondly, it will explore the actual technological possibilities, therefore providing some crucial data for finalizing the optimization routine derived in Chapter 3 and determining the most suitable process for the generator fabrication.

Chapter 5 will deal directly with the generator prototyping, from the stator manufacturing to the implementation in the watch movement. The fabrication technique will be upgraded for the fabrication of multilayer coils and a method for the liberation of the stators from the silicon substrate will be developed as well. In this context, morphological and electrical measurements will be performed in order to ensure the success of both intermediate fabrication steps as well as the functionality of the final prototype.

Finally, Chapter 6 will revise the main conclusions and contributions of the thesis, and present some perspectives for future developments.

2 Modeling of MEMS synchronous machines

This chapter aims to address the modeling of axial flux MEMS synchronous machines from a general perspective. In order to do so, the differential non-linear equations that govern the electrical and mechanical dynamics are derived using a rigorous approach based on Hamilton's principle. The model that will be obtained provides a comprehensive description of the device behavior, and due to its time domain formulation represents a powerful tool for transient regime analysis.

While the model is in principle applicable to every synchronous machine, the dissertation will focus on how it can be adapted for the description of devices at small scale, considering how these machines differ from their macro scale counterparts. This will be pursued by presenting the scaling laws, as well as by discussing the typical construction features of MEMS devices and their influence at a functional level.

Finally, the model will be used for the analysis of an existing device. In this context, several strategies for the determination of the model defining parameters, based both on analytic formulations and Finite Element Method (FEM) will be proposed.

2.1 Conceptual modeling of electromechanical systems

At macroscale, electrical machines are ubiquitous from domestic to industrial level and by now the theory concerning the modeling of such machines is quite structured and well known [Gie08]. In common practice, the design problem is often simplified by a wide set of ready-to-use formulas which allow a fast and effective optimization of the device of interest. However, not all the models that are commonly used at large scale are necessarily suitable (or convenient) for the description of the same machines at microscale. In fact, while the basic principle of operation is the same, from a construction viewpoint small scale machines can differ drastically from their macro counterparts. As a consequence, some basic assumptions might no longer hold true, which will ultimately lead to faulty design strategies. For example, there are optimization criteria revolving around construction parameters that at microscale might have no significance (*e.g.* the poles shape). At the same time, the influence of other variables on the overall performances of the device needs to be considered with more cautiousness. For these reasons, the modeling will be addressed by adopting an approach as general as possible, following the flow reported in Figure 2.1. The starting point is Hamilton's principle. Such formulation has the highest level of abstraction, since it can virtually be written for any electromechanical system. The problem will then be defined by the introduction of a first group of hypotheses. This will allow the derivation of a set of equation of motion that will be representative of the dynamic behavior of a rotating synchronous electrical machine, but will not include any specific indication concerning the size of the device. Finally, the main parameters appearing in the equations will be discussed specifically for the case of small case devices.

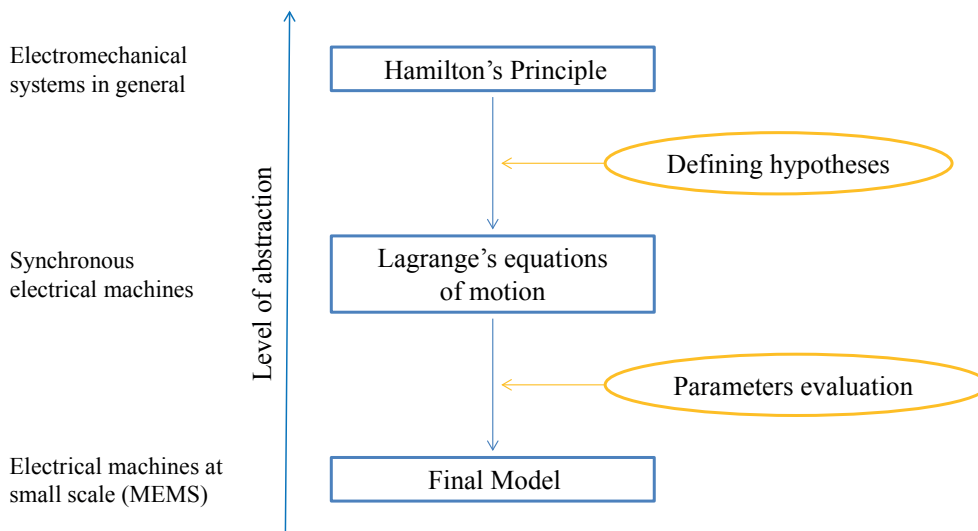


Figure 2.1 – Conceptual flow for the modeling of synchronous machines at small scale.

2.2 Evolution equations for synchronous machines

2.2.1 Hamilton's principle and Lagrange's formulation

In order to derive the equations of motions for the system of interest, the Hamilton-Lagrange formulation will be adopted. This paragraph will briefly present the basic steps that lead from Hamilton's principle to Lagrange's equations. For a rigorous treatise of the subject one can refer to [Pre06, Giu09]. The Hamilton's principle was first formulated in 1853 for classical mechanics, but it can be extended with ease to other fields of physics including electromagnetism. The principle expresses the problem of dynamic equilibrium for a generic system in a variational form, as expressed by:

$$V.I. = \int_{t_1}^{t_2} [\delta L + \delta W_{nc}] dt = 0 \quad (2.1)$$

In which the term $V.I.$ stands for variational indicator, δW_{nc} represents the virtual work of non-conservative forces and the term L is called Lagrangian of the system, given by:

$$L = \Gamma - \Pi \quad (2.2)$$

where Γ and Π represent the generalized kinetic and potential energies respectively.¹ Expression (2.1) basically states that among all the arbitrary dynamic paths between two instants t_1 and t_2 , the actual one followed by a system is the one that nullifies the variational indicator $V.I.$. As can be observed, the Hamilton's principle is based on energies and since it is not explicitly related to the system configuration, it does not provide a useful descriptive tool as it is. It is therefore convenient to rewrite the principle in the form of the Lagrange's equations. In order to do so, the first step is to define an N -size array of generalized coordinates $q_i = \{q_1(t), q_2(t), \dots, q_N(t)\}$. The choice of the coordinate set is arbitrary, nevertheless it is here supposed that the coordinates are independent or, in other words, that the size N of the array q_i equals the number of the system degrees of freedom (DOF). It should be noted that each coordinate can be either mechanical or electrical. Once the set q_i is defined, the set $\dot{q}_i = \{\dot{q}_1(t), \dot{q}_2(t), \dots, \dot{q}_N(t)\}$ of the associated time-derivative can be introduced as well. The Lagrangian in its most general form is then a function of such coordinates sets,

¹In order to keep the dissertation agile, the difference between energy and coenergy will not be discussed.

Chapter 2. Modeling of MEMS synchronous machines

and can also depend explicitly on time:

$$L = L(q_i(t), \dot{q}_i(t), t) \quad (2.3)$$

In order to obtain a more significant expression for the work of the non-conservative forces appearing in (2.1), it is convenient to separate them in two groups.

The first group is included in the array Q_i , which is defined as the set of the forces associated with the coordinates q_i . This means that such forces inject (or drain) energy to the system through the variation of the corresponding coordinates. It should be noted that the term "force" has here a generalized meaning. In fact, from a dimensional standpoint, the elements in Q_i are not necessarily forces nor are required to be homogeneous. Nevertheless, the product between an element of Q_i and its associated coordinate q_i always has the physical dimension of an energy. In the same way, we can define the array F_i^v of the "viscous" generalized forces, which act in the exact same way as the forces Q_i , but are associated with the time-derivative coordinates \dot{q}_i , instead. It is also customary in literature to define the forces of this second group as the gradient of a dissipation function D :

$$F_i^v = -\frac{\partial D}{\partial \dot{q}_i} \quad (2.4)$$

The work of the non-conservative forces can thus be expressed as

$$\delta W_{nc} = \sum Q_i \delta q_i + \sum F_i^v \delta \dot{q}_i = \sum Q_i \delta q_i - \sum \frac{\partial D}{\partial \dot{q}_i} \delta \dot{q}_i \quad (2.5)$$

By introducing expression (2.3) and (2.5) in (2.1) and integrating by parts [Pre06], it is possible to obtain the following formulation:

$$\frac{d}{dt} \left(\frac{\partial L}{\partial \dot{q}_i} \right) - \frac{\partial L}{\partial q_i} + \frac{\partial D}{\partial \dot{q}_i} = Q_i \quad (2.6)$$

Expression (2.6) represents a set of differential equations, whose number equals the system DOF and which describe the time evolution of the system in terms of the above defined generalized coordinates. As will be shown in the following paragraphs, the

2.2. Evolution equations for synchronous machines

advantage of this formulation is that if the Lagrangian and the generalized forces are conveniently expressed, the derivation of the governing equations is straightforward. Moreover, the laws of physics involved (*e.g.* Faraday's law), as well as the multiphysics interactions between the system sub-entities, are automatically taken into account. This will be the objective of the next paragraph.

2.2.2 Energy expressions for synchronous machines

Lagrange's equations (2.6) have a general validity, and very little assumptions were made in order to derive them from Hamilton's principle. The first refinement of the model (*cf.* Figure 2.1) consists in its adaptation to synchronous machines. In particular, the focus will be on rotating systems. Such devices exist for a wide variety of applications, and from a construction perspective they can differ substantially one from another depending on size and power range [Juf95]. The model was therefore derived on the basis of an extremely broad definition, according to which a synchronous machine can be regarded as a device consisting of two basic elements, a stator and a rotor, which can be put in relative rotation. One of the elements, usually the stator (*cf.* Figure 2.2), houses one or several coils (variously connected), which can be excited freely. On the other hand, the rotor comprises a number p of magnetic pole pairs. By hypothesis, the pole pairs can be obtained with either permanent magnets or windings excited with a constant current. An example of such a device is reported in Figure 2.3.

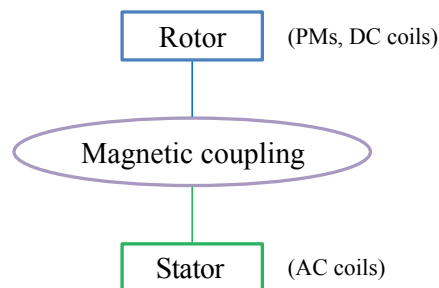


Figure 2.2 – Schematic of a single-phase synchronous machine.

Functional scheme

In order to derive the governing equations it is convenient to refer to the functional scheme in Figure 2.4, which describes a simple configuration with only one phase (potentially comprising multiple windings connected in series). The stator is represented by an electric circuit including the inner inductance L_i and resistance R_i of the phase coil. A load resistance R_l is branched at the end of the circuit, while the voltage U is an external source. The rotor is characterized by its moment of inertia J and can be put into motion under the action of a torque applied from the exterior T_{in} . The term ψ represents the flux linkage between the magnetic field generated by the rotor and

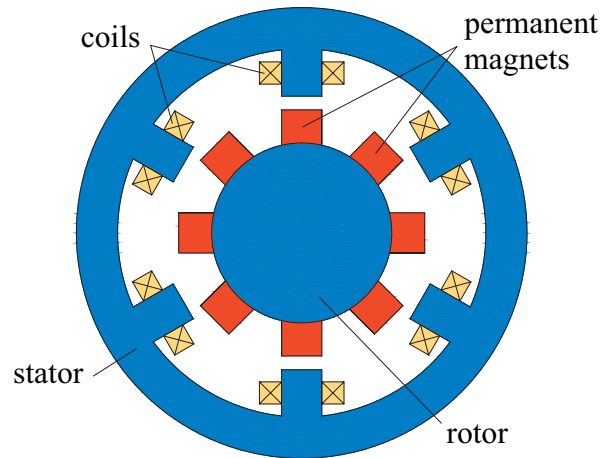


Figure 2.3 – Example of a synchronous machine.

the stator coil, while Ω and I are the angular velocity of the rotor and current circuit respectively.

The system has 2 degrees of freedom, so it can be effectively modeled by using 2 generalized coordinates q_i . As already explained, the choice is completely arbitrary, nevertheless expressing the energies involved becomes straightforward if the rotor angular position ϑ and the charge q circulating in the circuit are chosen. Moreover, with this choice the time-derivatives of the generalized coordinates \dot{q}_i become particularly meaningful, since they coincide with the rotor angular velocity Ω and the phase current I respectively. Finally, the associated non-conservative forces Q_i , in the sense specified in the previous paragraph, can be identified as the input torque T_{in} (which can be either positive or negative) and the external voltage source U (usually periodical) (2.7). For readability reasons, the time-dependency of such quantities will be omitted from now on.

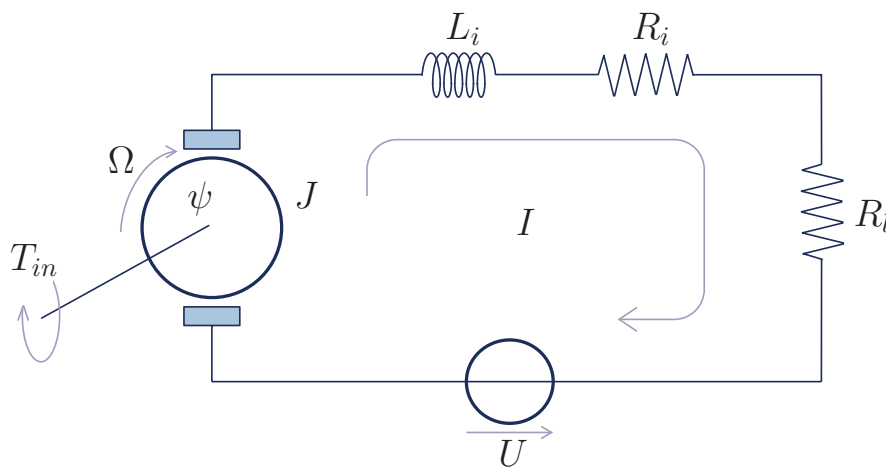


Figure 2.4 – Functional scheme of a single phase synchronous rotating machine

2.2. Evolution equations for synchronous machines

$$q_i = \begin{bmatrix} \vartheta(t) \\ q(t) \end{bmatrix} \quad \dot{q}_i = \begin{bmatrix} \Omega(t) \\ I(t) \end{bmatrix} \quad Q_i = \begin{bmatrix} T_{in}(t) \\ U(t) \end{bmatrix} \quad (2.7)$$

Since there is no potential energy in the system ($\Pi = 0$), the set of Lagrange's equations becomes:

$$\frac{d}{dt} \left(\frac{\partial \Gamma}{\partial \dot{q}_i} \right) - \frac{\partial \Gamma}{\partial q_i} + \frac{\partial D}{\partial \dot{q}_i} = Q_i \quad (2.8)$$

Kinetic energy

The generalized kinetic energy Γ , can be decomposed into the sum of 3 different terms:

$$\Gamma = \Gamma_m + \Gamma_{el} + \Gamma_{mag} \quad (2.9)$$

In (2.9) Γ_m , Γ_{el} and Γ_{mag} represent the mechanical, electrical and magnetic contributions respectively. The mechanical part corresponds to the rotational energy of the moving part as in (2.10). Such expression does not require a particular modeling effort, as the only construction parameter involved is the inertia J , which only depends on the mass and the shape of the rotor.

$$\Gamma_m = \frac{1}{2} J \Omega^2 \quad (2.10)$$

A first contribution to the electrical part is associated with the energy stored within the inductance of the stator winding(s) L_i . In general, such parameter depends on the machine configuration, due to the fact that the rotor displacement usually entails a variation of the magnetic permeance seen by the field generated by the coil itself. This effect is particularly pronounced, among the others, for salient pole machines [Cha83]. As a general rule, the inductance also depends on all the magnetic fields present in the system (generated by both the rotor and the stator) due to the saturation that might occur in the ferromagnetic medium. The term Θ_s appearing in (2.11) represents an equivalent magnetic potential as seen by the medium worth for the description of such effect. Nevertheless, it will be here assumed that the device operates in a linear regime,

Chapter 2. Modeling of MEMS synchronous machines

which is usually the case of greatest interest for low scale applications.

$$L_i = L_i(\vartheta, \Theta_s) \rightarrow L_i(\vartheta) \quad (2.11)$$

The same considerations concerning the modification of the magnetic paths, can also be done for the circuit of excitation. In order to take into account for such effect, it is convenient to express the energy associated with the rotor pole pairs in terms of the magnetic potential of excitation Θ_e and the corresponding permeance Λ_e . The potential can be supplied by either permanent magnets or DC windings and it's therefore constant over time, while the permeance Λ_e is a function of the rotor angular position similarly to L_i . The electrical kinetic energy can thus be written as (2.12).

$$\Gamma_{el} = \frac{1}{2}L_i(\vartheta)I^2 + \frac{1}{2}\Theta_e^2\Lambda_e(\vartheta) \quad (2.12)$$

As for the magnetic contribution, it can be expressed as the product of the circulating current and the magnetic flux between the rotor and the stator [Giu09]. The latter is in general a function of both space and time. However, according to the given definition of synchronous machine, the source of the rotor magnetic field are either PMs or DC coils. As a consequence, the associated magnetic flux cannot have an explicit dependency on time (2.13). The magnetic kinetic energy can thus be expressed as in (2.14).

$$\psi = \psi(\vartheta, t) \rightarrow \psi(\vartheta) \quad (2.13)$$

$$\Gamma_{mag} = \psi(\vartheta) I \quad (2.14)$$

Friction and dissipation function

The dry friction will be here represented by introducing a resisting torque T_{fr} . Such torque is constant over time, and it basically depends on the mechanical apparatus and its conditions (bearings, lubrication, *etc.*). It can be directly included in the set Q_i of the generalized forces, as can be seen in (2.15), where the minus sign indicates that it opposes the direction of motion.

$$Q_i = \begin{bmatrix} T_{in}(t) - T_{fr} \operatorname{sgn}(\Omega) \\ U(t) \end{bmatrix} \quad (2.15)$$

The dissipation function D can be considered as the sum of two contributions from the mechanical and the electrical subsystems (2.16).

$$D = D_m + D_{el} \quad (2.16)$$

The mechanical dissipation function D_m is associated with the viscous effects, which are in general a function of the rotor velocity. A simple way to express it is to assume that D_m is quadratic with respect to the rotor velocity as in (2.17)), where the coefficient β is called the viscous friction coefficient and is measured in $[N.m.s]$.

$$D_m = D_m(\Omega) = \frac{1}{2}\beta\Omega^2 \quad (2.17)$$

The electrical dissipation is associated with the resistors appearing in the equivalent circuit of Figure 2.4. For such elements it is customary to define the function D_{el} as in (2.18). Theoretically, the electrical dissipation of the excitation circuit should also be included. Nevertheless, such term is absent if PMs are employed and usually negligible if DC coils are used instead.

$$D_{el} = \frac{1}{2}(R_i + R_l)I^2 \quad (2.18)$$

2.2.3 Derivation of the equations

The energy expressions just obtained, allow to develop (2.8). The total generalized kinetic energy is given by:

$$\Gamma = \frac{1}{2}J\Omega^2 + \frac{1}{2}L_i(\vartheta)I^2 + \frac{1}{2}\Lambda_e(\vartheta)\Theta_e^2 + \psi(\vartheta)I; \quad (2.19)$$

Chapter 2. Modeling of MEMS synchronous machines

The term $\frac{\partial \Gamma}{\partial q_i}$ becomes:

$$\frac{\partial \Gamma}{\partial \vartheta} = I^2 \frac{1}{2} \frac{dL_i(\vartheta)}{d\vartheta} + I \frac{d\psi(\vartheta)}{d\vartheta} + \Theta_e^2 \frac{1}{2} \frac{d\Lambda_e(\vartheta)}{d\vartheta}; \quad \frac{\partial \Gamma}{\partial q} = 0 \quad (2.20)$$

The term $\frac{d}{dt} \left(\frac{\partial \Gamma}{\partial \dot{q}_i} \right)$ gives:

$$\frac{\partial \Gamma}{\partial \Omega} = J\Omega; \quad \frac{d}{dt} \left(\frac{\partial \Gamma}{\partial \Omega} \right) = J\dot{\Omega} \quad (2.21)$$

$$\frac{\partial \Gamma}{\partial I} = L_i I + \psi(\vartheta); \quad \frac{d}{dt} \left(\frac{\partial \Gamma}{\partial I} \right) = L_i \frac{dI}{dt} + I \frac{dL_i}{d\vartheta} \Omega + \frac{d\psi(\vartheta)}{d\vartheta} \Omega \quad (2.22)$$

The total dissipation function is given by:

$$D = \frac{1}{2} \beta \Omega^2 + \frac{1}{2} (R_i + R_l) I^2 \quad (2.23)$$

Hence, the term $\frac{\partial D}{\partial \dot{q}_i}$ can be developed into:

$$\frac{\partial D}{\partial \Omega} = \beta \Omega; \quad \frac{\partial D}{\partial I} = (R_i + R_l) I; \quad (2.24)$$

By putting the corresponding terms together the governing equations (2.25) can finally be obtained.

$$\begin{cases} J\dot{\Omega} - I^2 \frac{1}{2} \frac{dL_i(\vartheta)}{d\vartheta} - \Theta_e^2 \frac{1}{2} \frac{d\Lambda_e(\vartheta)}{d\vartheta} - I \frac{d\psi(\vartheta)}{d\vartheta} + \beta \Omega = T_{in} - T_{fr} \operatorname{sgn}(\Omega) \\ L_i(\vartheta) \frac{dI}{dt} + I \frac{dL_i(\vartheta)}{d\vartheta} \Omega + \frac{d\psi(\vartheta)}{d\vartheta} \Omega + (R_i + R_l) I = U \end{cases} \quad (2.25)$$

The system in (2.25) consists of non-linear differential equations. In particular, the first one describes the rotor dynamics in terms of the angular position and its first and

2.2. Evolution equations for synchronous machines

second order time-derivatives, while the second one governs the electrical circuit in terms of the quantity of charge circulating in the stator circuit. As can be observed, the equations are interdependent. In fact, the terms I and I^2 are involved in the mechanical equation, while the term Ω intervenes in the electrical one. The term $\frac{d\psi}{d\vartheta}$ is also common and is inherently associated with the magnetic coupling between the rotor and the stator.

Some considerations can also be drawn if the device symmetry is taken into account. This can be better understood by looking at Figure 2.5, which represents a linear development of a single-phase device including 4 magnetic poles ($p = 2$) and an equal number of coils.

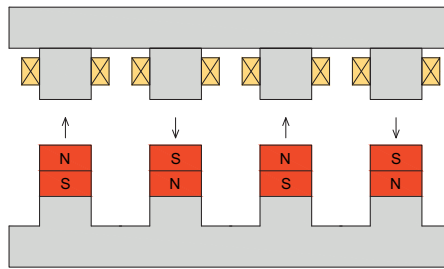


Figure 2.5 – Linear development of a single-phase synchronous machine.

The magnetic field B generated by the permanent magnets is periodical with respect to the rotation angle ϑ (with null average component). As a consequence, the total flux linkage with the stator coils will be periodical in nature as well. Hence, assuming that the flux is maximum when the magnetic poles and the coils are aligned ($\vartheta = 0$), the flux can be expressed as the sum of harmonics. Also, given that the $2p$ magnetic pairs are arranged with alternating polarity (a condition which is usually verified), one can safely assume the pulsation of the fundamental harmonic to be equal to p :

$$\psi(\vartheta) = \sum_{k=1}^{\infty} \psi_k \cos(kp\vartheta) \quad (2.26)$$

The derivative with respect to ϑ can thus be written as:

$$\frac{d\psi(\vartheta)}{d\vartheta} = - \sum_{k=1}^{\infty} kp\psi_k \sin(kp\vartheta) \quad (2.27)$$

In practice, given a certain distribution of the field B , the number of the harmonics that are necessary for an effective reconstruction of the magnetic flux depends on the

coils shape and arrangement. Usually, a form as sinusoidal as possible is considered as optimal. The same approach can be used for the terms $\frac{dL_i(\vartheta)}{d\vartheta}$ and $\frac{d\Lambda_e(\vartheta)}{d\vartheta}$. In such cases, the frequency of the fundamental harmonic is in general a multiple with respect to the frequency of flux, and depends on the number of poles, the number of coils (or rather their supporting mechanical structures) and the number of phases.

2.2.4 Physical interpretation

The terms appearing in (2.25) have a very specific physical interpretation. From a canonical perspective, the first equation can be read as the well known Newton's law of dynamics for a rotational system. The sum of the terms that are not purely mechanical represent the characteristic couple of the device T_m :

$$T_m = \underbrace{I^2 \frac{1}{2} \frac{dL_i(\vartheta)}{d\vartheta}}_{\text{reluctant}} + \underbrace{\Theta_e^2 \frac{1}{2} \frac{d\Lambda_e(\vartheta)}{d\vartheta}}_{\text{em}} + I \frac{d\psi(\vartheta)}{d\vartheta} \quad (2.28)$$

The first two terms appearing in (2.28) are reluctant in nature, since they are associated with any modification that may occur in the magnetic paths due to the rotor angular displacement. The first contribution depends quadratically on the current, and is therefore zero in open circuit conditions. On the other hand, the second contribution does not depend on the excitation conditions of the device, and it's solely due to the interactions of the PMs (or the DC electromagnets) with the surrounding material. Finally, the third contribution in (2.28) is the electromagnetic couple generated by the interaction between the rotor and stator magnetic fields. As for the second equation in (2.25), it can be read as the usual Kirchhoff's law for an R-L circuit, where the total induced voltage (back EMF) U_i is given by (2.29). In compliance with Faraday's law, the back EMF is generated in the stator coils by any flux variation over time. In this sense, the first contribution of U_i is given by the relative motion between the magnet and the coil, whereas the second contribution is associated with variations of the flux generated by the current circulating in the coil itself due to modifications of the coil inductance.

$$U_i = \underbrace{\frac{d\psi(\vartheta)}{d\vartheta}}_{\text{magnet}} \Omega + \underbrace{I \frac{dL_i}{d\vartheta}}_{\text{inductance}} \Omega \quad (2.29)$$

2.2.5 Extension to multi-phase machines

The equations (2.25) were derived by writing Hamilton's principle for a single-phase system. The same methodology can be extended with relative ease for multiple phase devices. In this sense, a case of great interest is represented by the three-phase machine, since this configuration is commonly preferred when the machine is designed to operate as a motor. The functional scheme of reference is reported in Figure 2.6, where r , s and t designate the phases. Each phase is represented by its own electric circuit, comprising the inner resistance R_x , impedance L_x , load resistance R_{lx} as well as potential source U_x . The magnetic coupling between stator and rotor is described by the flux ψ_x . In turn, the rotor is described by the same parameters as the previously analyzed case. It should be noted that in such scheme each phase is considered electrically disconnected from the others.

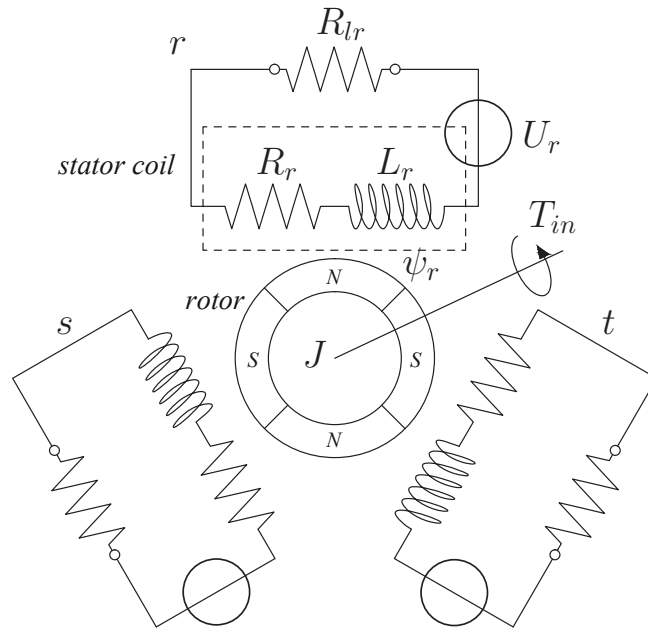


Figure 2.6 – Functional scheme of three phase synchronous rotating machine.

Each phase adds another degree of freedom to the system, so that the whole system can be described by 4 generalized coordinates. By choosing the rotor angular position and the charge circulating in the circuit, the following sets of coordinates and generalized forces are obtained:

$$q_i = \begin{bmatrix} \vartheta(t) \\ q_r(t) \\ q_s(t) \\ q_t(t) \end{bmatrix} \quad \dot{q}_i = \begin{bmatrix} \Omega(t) \\ I_r(t) \\ I_s(t) \\ I_t(t) \end{bmatrix} \quad Q_i = \begin{bmatrix} T_{in}(t) - T_{fr} \operatorname{sgn}(\Omega) \\ U_r(t) \\ U_s(t) \\ U_t(t) \end{bmatrix} \quad (2.30)$$

Chapter 2. Modeling of MEMS synchronous machines

The main difference is that the mutual inductances $M_{xy}(\vartheta)$ between coils of different phases must be considered. This results in a contribution to the generalized kinetic energy in the form of $\frac{1}{2}M_{xy}I_xI_y$. Since $M_{xy} = M_{yx}$, and each contribution has to be taken into account twice, the final expression of Γ becomes:

$$\begin{aligned} \Gamma = & \frac{1}{2}J\Omega^2 + \frac{1}{2}\Lambda_e(\vartheta)\Theta_e^2 + \frac{1}{2}L_r(\vartheta)I_r^2 + \frac{1}{2}L_s(\vartheta)I_s^2 + \frac{1}{2}L_t(\vartheta)I_t^2 + \\ & + M_{rs}(\vartheta)I_rI_s + M_{st}(\vartheta)I_sI_t + M_{rt}(\vartheta)I_rI_t + \psi_r(\vartheta)I_r + \psi_s(\vartheta)I_s + \psi_t(\vartheta)I_t \end{aligned} \quad (2.31)$$

The dissipation function D must also be modified in order to take into account for the resistors in each phase, and it can thus be written as:

$$D = \frac{1}{2}\beta\Omega^2 + \frac{1}{2}(R_r + R_{lr})I_r^2 + \frac{1}{2}(R_s + R_{ls})I_s^2 + \frac{1}{2}(R_t + R_{lt})I_t^2 \quad (2.32)$$

Following the same steps as in paragraph 2.2.3, one can obtain the system of equations reported below.

$$\left\{ \begin{array}{l} J\dot{\Omega} - \Theta_e^2 \frac{1}{2} \frac{d\Lambda_e}{d\vartheta} - I_r^2 \frac{1}{2} \frac{dL_r}{d\vartheta} - I_s^2 \frac{1}{2} \frac{dL_s}{d\vartheta} - I_t^2 \frac{1}{2} \frac{dL_t}{d\vartheta} - I_r I_s \frac{dM_{rs}}{d\vartheta} - I_s I_t \frac{dM_{st}}{d\vartheta} - I_r I_t \frac{dM_{rt}}{d\vartheta} + \\ \quad - I_r \frac{d\psi_r}{d\vartheta} - I_s \frac{d\psi_s}{d\vartheta} - I_t \frac{d\psi_t}{d\vartheta} + \beta\Omega = T_{in} - T_{fr} \operatorname{sgn}(\Omega) \\ L_r \frac{dI_r}{dt} + I_r \frac{dL_r}{d\vartheta} \Omega + M_{rs} \frac{dI_s}{dt} + I_s \frac{dM_{rs}}{d\vartheta} \Omega + M_{rt} \frac{dI_t}{dt} + I_t \frac{dM_{rt}}{d\vartheta} \Omega + \frac{d\psi_r}{d\vartheta} \Omega + I_r (R_r + R_{lr}) = U_r \\ L_s \frac{dI_s}{dt} + I_s \frac{dL_s}{d\vartheta} \Omega + M_{st} \frac{dI_t}{dt} + I_t \frac{dM_{st}}{d\vartheta} \Omega + M_{rs} \frac{dI_r}{dt} + I_r \frac{dM_{rs}}{d\vartheta} \Omega + \frac{d\psi_s}{d\vartheta} \Omega + I_s (R_s + R_{ls}) = U_s \\ L_t \frac{dI_t}{dt} + I_t \frac{dL_t}{d\vartheta} \Omega + M_{rt} \frac{dI_r}{dt} + I_r \frac{dM_{rt}}{d\vartheta} \Omega + M_{st} \frac{dI_s}{dt} + I_s \frac{dM_{st}}{d\vartheta} \Omega + \frac{d\psi_t}{d\vartheta} \Omega + I_t (R_t + R_{lt}) = U_t \end{array} \right. \quad (2.33)$$

2.2.6 Advantages and drawbacks

The governing equations (2.25) and (2.33), are formulated in the time domain. Due to the non-linearity and interdependency an analytic solution cannot be found and a numerical approach should be adopted instead. In turn, one of the main advantages is that, once the proper numerical method is assessed, the model allows to simulate a great variety of situations, with virtually any boundary conditions. For example, the

generator and the motor mode are easily obtained by choosing the appropriate input vector of generalized forces Q_i as in (2.34).

$$Q_i^{gen} = \begin{bmatrix} T_{in}(t) \\ 0 \\ 0 \\ 0 \end{bmatrix} \quad Q_i^{mot} = \begin{bmatrix} -T_{in}(t) \\ U_r(t) \\ U_s(t) \\ U_t(t) \end{bmatrix} \quad (2.34)$$

Furthermore, any dynamic change of the system configuration, as for example a varying load or a commutation, can be managed with relative ease, thus simplifying the analysis of the transition between one state and another. It should be put into evidence however, that model was derived by expressing all of the energy contributions in terms of arbitrary generalized coordinates. As a consequence, a limit of the model is that it is substantially blind to any evolution pattern occurring along other coordinates. A pertinent example is the static contribution to the reluctant couple $\Theta_e^2 \frac{1}{2} \frac{d\Lambda_e(\vartheta)}{d\vartheta}$, which is generated by the interaction of the PMs with the surrounding ferromagnetic material. Such term was supposed to depend only on the angular position of the rotor. While such hypothesis holds for a wide range of machines, due to their construction symmetries, it's not uncommon, especially at small scale, to find systems in which strong positioning torques or forces originate from stray magnetic streamlines interacting with "randomly" placed ferromagnetic materials.

2.3 Scaling laws and MEMS devices

2.3.1 Design problem

The systems of equations (2.25) and (2.33) describe the evolution of synchronous machines in a general way but, except for some basic assumptions on the device symmetry, they do not specify the actual form of the parameters appearing in them. In this sense, the design problem consists of:

- Identifying the functions that represent the construction parameters of interest;
- combining them in order to obtain one or multiple objective functions.

The model parameters are resumed in Table 2.2. In the following paragraphs, the discussion will focus on the relevance and the evaluation methods for each parameter as the size is reduced up to MEMS level.

Table 2.1 – Model parameters

	units	type	description
J	kg.m ²	mechanical	rotor moment of inertia
β	N.m.s	mechanical	viscous friction coefficient
T_{fr}	N.m	mechanical	dry friction torque
$R_i(\vartheta)$	Ω	electrical	phase resistance
$L_i(\vartheta)$	H	electrical	phase self inductance
$M(\vartheta)$	H	electrical	mutual inductance between 2 phases
$\Lambda_e(\vartheta)$	H	magnetic	equivalent permeance seen by PMs
$\psi(\vartheta)$	V.s	magnetic	flux between PMs and phase coils

2.3.2 Mechanical parameters

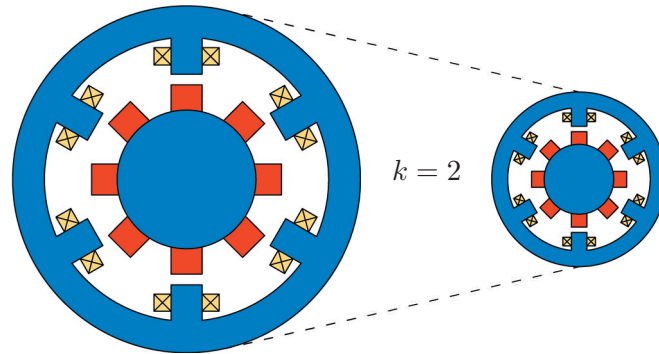
The design of the rotor makes the object of a whole branch of applied mechanics, called rotor dynamics, which focuses on how to take into account the influence of vibrations, bearings, interactions with fluids and so on [Gen05]. At the same time, including this theory in a comprehensive optimization strategy is quite difficult, and although some authors have made remarkable efforts in this sense (see for example [KALS11, UKN⁺16]), this task is often performed separately. It should be also noted that a detailed study of the rotor mechanical performances becomes usually necessary at high operational speeds. In general, this is not the case at small scale, as size reduction entails an enhancement of the safe speed range [BPF10]. For this reason, the viscous torque $\beta\Omega$ and the friction T_{fr} are often measured directly on the prototype, and considered as design parameters only in very specific cases.

2.3.3 Electrical and magnetic parameters

The issue of size reduction will be addressed at two levels. The first one considers a homotetic size reduction as in Figure 2.7. At this level, it is only assumed that each geometric trait of the machine is scaled of a factor k . Then, some considerations concerning the actual construction differences between a large and a MEMS scale device, will be added.

Resistance

The overall resistance the phase coils R_i is the sum of the DC resistance and two terms, Y_s and Y_p , representing an increasing due to skin and proximity effects. While the DC contribution only depends on the conductor resistivity ρ , length l and section S , the


 Figure 2.7 – Homotetic size reduction for a factor $k = 2$.

other two terms depend on the frequency of operation f :

$$R_i = \rho \frac{l}{S} + Y_s(f) + Y_p(f) \quad (2.35)$$

Skin effect is the tendency of an AC current to not distribute uniformly on the section of the conductor in which it's circulating. Instead, the current density is the highest near the conductor surface and decreases exponentially towards the center, thus reducing the actual section that is used for conduction. Proximity effect is also a deformation of the current density within a conductor, but it's caused by the interaction with magnetic fields generated by nearby current carrying conductors. Both phenomena are absent at DC, and become more pronounced as the frequency increases. In general, such additional losses cannot be neglected and several studies have been carried out for their determination in PM electrical machines [IDL⁺09, TZJ09, PD13, LFLT16]. These are however focused on large scale machines, with conductor diameters in the mm range and designed to operate at high speed. At small scale, several simplifications can be made. The impact of skin effect can be evaluated by calculating the skin depth [PP99], which is defined as the the distance from the conductor surface in which the current density is reduced to about 37%:

$$\delta = \sqrt{\frac{\rho}{\pi \mu f}} \quad (2.36)$$

The electrical frequency of operation in this domain ranges from a few Hz to several kHz (machines with rotational speed $\sim 1 \cdot 10^5 rpm$). This entails skin depth in the mm range, far above the height and width of MEMS conductors, which are usually of the order of tens of μm . As a consequence, it can be safely assumed that the current density

Chapter 2. Modeling of MEMS synchronous machines

non uniformity due to skin effect is completely negligible. Evaluating proximity effect is in turn more complex, due to the variety of configurations and conductor sections. The majority of studies in this field revolves around the model derived by Dowell [Dow66] in 1966 and its more recent refinements by Ferreira [Fer90, Fer94, Fer92]. Among the others, Stefanini [Ste06] discussed the influence of inter conductor spacing as well as conductor section. While these models are not specifically derived referencing MEMS conductors, they are unanimous in predicting no significant proximity effect for conductors and frequencies in the aforementioned range. This can be empirically verified using FEM as well (see Appendix A). As a result, the phase resistance can be assumed to be coincident with its DC value:

$$R_i \approx R_i^{DC} \quad (2.37)$$

Shrinking the geometry of a factor k will not influence the resistivity of the material, in turn the new length of the conductor becomes $l^* = l.k^{-1}$, while the new section is equal to $A^* = S.k^{-2}$. The scaled resistance R_i^* is thus given by

$$R_i^* = \rho \frac{l}{S} \frac{k^2}{k} \rightarrow \frac{R_i^*}{R_i} = k \quad (2.38)$$

In other words, the resistance results increased of a factor k .

Fluxes and magnetic paths

The terms Λ_e , ψ , L_i and M share the same physics nature, and their scaling can therefore be addressed simultaneously. In order to do that, it's here recalled that Hopkinson's law (2.39) states that a generic magnetic flux Φ circulating in a loop path can be obtained as the product of the magnetic potential Θ (or magnetomotive force, supplied by coils or permanent magnets) and the permeance Λ associated to the path.

$$\Phi = \Theta \Lambda \quad (2.39)$$

All of the aforementioned parameters refer to this law, in particular:

- Λ_e is a permeance.

- ψ is the flux of the magnetic field generated by the PMs to through the phase coil(s).
- L_i is defined as the ratio of the flux of magnetic field generated by the phase coil(s) through the coil(s) itself to the current circulating in the coil(s).
- M is defined as the ratio of the flux of magnetic field generated by one phase coil(s) through the coil(s) of another phase to the current circulating in the coil(s) of the first phase.

As a general rule, as long as a magnetic field (or most of it) is guided by the presence of a ferromagnetic path, a number of simplifying hypotheses can be adopted, thus making the application of Hopkinson's law is straightforward. In turn, as air gaps and stray field lines appear, the simplifying hypotheses tend to fall apart, which makes the calculation more problematic. The concept is clarified by Figure 2.8, which represents the magnetic field distribution (obtained by FEM) for the same three turns coil with different magnetic paths.

The situation depicted in Figure 2.8(a) is considered as ideal from the point of view of the mere application of Hopkinson's law: the ferromagnetic loop is closed and there are no air gaps (or, more generally, segments with high magnetic reluctance). As a consequence, the magnetic field is completely confined in the loop. This allows to formulate the following hypotheses:

- (i) The total flux is the same for each coil turn.
- (ii) The magnetic field can be assumed to be uniform on the path section.

The permeance can thus be calculated with relative ease using (2.40), in which γ is the length of the path and μ is the permeability of the material. At this point, since the magnetic potential Θ is usually easy to express, (2.39) allows an immediate calculation of the magnetic flux through the coil.

$$\Lambda^{-1} = \int_{\gamma} \frac{dl}{\mu A} \quad (2.40)$$

In Figure 2.8(b), which represents a situation which is common for electrical machines at standard scale, an air gap is introduced. In principle, if its size is small with respect to the rest of the ferromagnetic path, (i) can still be considered valid. Nevertheless, as the air gap size increases, the flux leakages become more important, and such effect has to be taken into account for proper modeling of electromagnetic actuators in general.

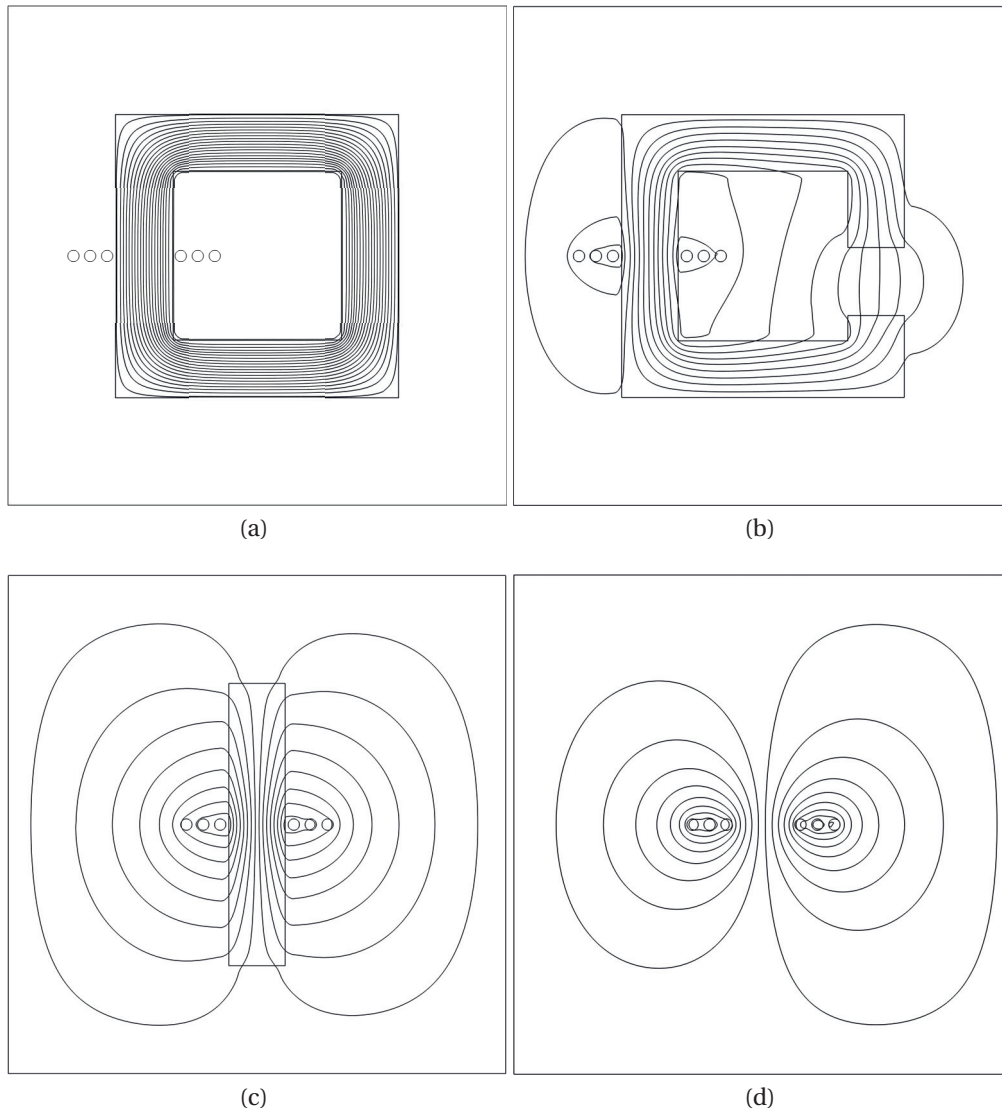


Figure 2.8 – Cross section of a three turns coil with different magnetic paths: (a) full circuit , (b) circuit with air gap, (c) ferromagnetic core, (d) air.

This is usually done by introducing additional permeances in the equivalent magnetic circuit. The first analytic model was proposed by Roters back in 1941 [Rot41]. His formula was derived by approximating the fringe field lines with simple geometrical entities, such as circles and straight lines, and the same approach was later adopted by other authors (see for example [CST06, BL09, Gri17]).

In Figure 2.8(c) the ferromagnetic material is reduced to a core, and it cannot be considered a closed loop anymore. For a system as such, not only the modeling of stray fluxes becomes more difficult, but even (i) might be jeopardized. Finally, Figure 2.8(d) represents the coil without any magnetic guidance. In this case Hopkinson's law

is basically not applicable, since not only the concept of permeance loses practical significance, but each coil turn sees a different flux and must therefore be considered individually. As already mentioned, electrical machines at standard scale usually present ferromagnetic loops with relatively small air gaps (Figure 2.8(b)). In such case, a first estimation of the impact of a homothetic size reduction of factor k can be pursued using (2.40), in the same way as for the resistance:

$$L_i^* = \mu \frac{Ak}{\gamma k^2} \rightarrow \frac{L_i^*}{L_i} = \frac{1}{k} \quad (2.41)$$

For the same magnetic potential (*cf.* (2.39)), this entails that each parameter is reduced of a factor k . This approach however is unsuitable for describing the transition to a MEMS synchronous machine. In fact, the use of ferromagnetic materials in such devices is in general limited, so that magnetic fields are very little guided or completely unconstrained, as exemplified in Figure 2.8(c) or (d). For this reason, the factor k is likely to underestimate dramatically the effect of size reduction.

2.3.4 Functional implications

On the basis of the discussion above, several key aspect concerning the electromechanical behavior of MEMS synchronous machines can be drawn.

Because of the reduced section of the conductor and the relatively low frequencies of operation, the phase resistance is not influenced by skin and proximity effects. However, it also tends to increase due to the reduction of the conductor section. Such effect is usually predominant, so that high ohmic losses should be expected. At the same time, since phase inductance tends to decrease for both scaling and technological reasons, the phase coils are likely to drift from inductive to resistive behavior.

As discussed in the previous paragraph, the lack of ferromagnetic loops, typical of synchronous MEMS machines, causes a significant drop of the parameters which are directly related to magnetic fluxes. From a functional point of view, this affects the device performances in terms of torque and induced voltage (*cf.* equations (2.28) and (2.29)), which are generally low and challenging to enhance.

2.4 Practical application

In this section, the model will be used for the study of a MEMS synchronous device which was originally developed by Merzaghi *et al.* in 2009 [MKP09, KMP10, MKP11]. The motivations for this are as follows:

Chapter 2. Modeling of MEMS synchronous machines

- Show and discuss the model possibilities for the system simulation
- Validate the dissertation on the scaling laws
- Demonstrate the use of FEM for the estimation of the model parameters

The discussion will be based only on the application of the model, and will purposely not focus on the manufacturing technology involved. In turn, such matter will be addressed extensively, with a particular attention to the fabrication of planar coils, in Chapter 5. Finally, in order to simplify the measurements, the device by Merzaghi will be characterized in its generator operating mode.

2.4.1 Description of the device

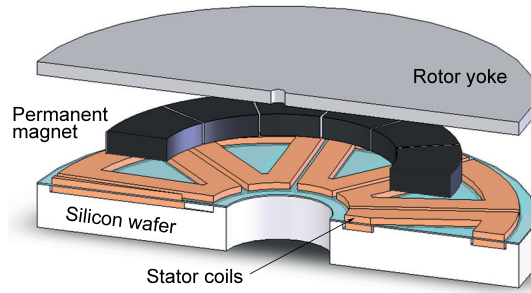
An exploded view of the device can be observed in Figure 2.9(a). The rotor is composed of one ferromagnetic yoke and a ring shaped magnet. The latter is realized with traditional sintering techniques, and is axially magnetized in order to form 12 magnetic poles. The diameter of the rotor is equal to 4 mm, while the thickness of the rotor yoke and the magnet are equal to 150 μm and 250 μm respectively. The stator (Figure 2.9(b)) is manufactured on a silicon wafer, and includes 9 planar coils connected in series three by three in order to form three phases. The coils are obtained by superposing two layers of 12 turns each with an insulating layer in between (Figure 2.9(c)). The conductor nominal width and thickness are equal to 20 and 25 μm , while the spacing between the windings is equal to 10 μm .

2.4.2 Evolution equations

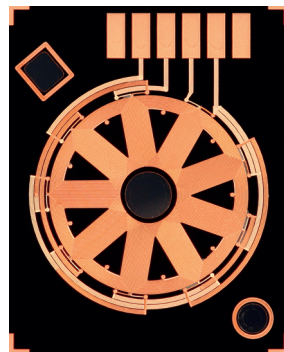
Since the device has 9 coils and 3 phases, the functional scheme of Figure 2.6 can be used by simply considering the series of three coils for each phase. The system of equations (2.33) can thus be used. Since each phase is composed by identical coils with the same spatial distribution, it can be assumed that the inner impedance is the same for each phase. Also, considering the symmetry in the windings relative positioning, the mutual inductance between 2 phases can be assumed to be the same as well:

$$\begin{aligned} R_r &= R_s = R_t = R_i \\ L_r &= L_s = L_t = L_i \\ M_{rs} &= M_{st} = M_{rt} = M \end{aligned} \tag{2.42}$$

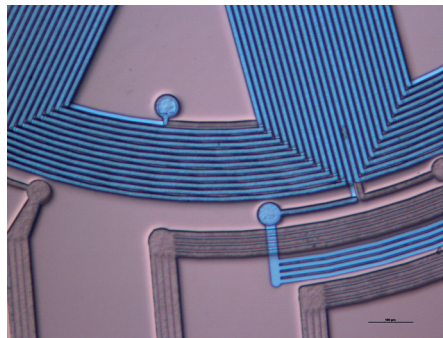
By looking at the geometry, it appears evident that no permeance variation is associated with the rotor angular position. As a consequence, the terms (2.43) are null, and so are



(a) Exploded view.



(b) Stator.



(c) Planar coil detail.

Figure 2.9 – The PM synchronous generator by Merzaghi *et al.* [MKP09, KMP10, MKP11]: schematic outlook (a), full microfabricated stator (b), detail of one copper coil (c).

the reluctant contributions associated to them.

$$\frac{d\Lambda_e}{d\vartheta} = 0 \quad \frac{dL_i}{d\vartheta} = 0 \quad \frac{dM}{d\vartheta} = 0 \quad (2.43)$$

The device is designed so that the symmetry and ratio between the number of coils and the number of magnetic poles are such that the flux linkage between the magnetic poles and each phase is the same with a 120 degrees shift between one phase and another. As a matter of fact, this condition is common for three-phase systems. Taking

the flux linkage of the phase r as a reference, one can write:

$$\begin{aligned}
 \psi_r &= \psi(\vartheta) \\
 \psi_s &= \psi\left(\vartheta + \frac{2}{3}\pi\right) \\
 \psi_t &= \psi\left(\vartheta - \frac{2}{3}\pi\right)
 \end{aligned} \tag{2.44}$$

Assuming the same load resistance R_l for each phase, and an input vector corresponding to the generator operating mode (*cf.* (2.34)) the system governing equations become:

$$\left\{ \begin{aligned}
 J\dot{\Omega} - I_r \frac{d\psi(\vartheta)}{d\vartheta} - I_s \frac{\psi\left(\vartheta + \frac{2}{3}\pi\right)}{d\vartheta} - I_t \frac{\psi\left(\vartheta - \frac{2}{3}\pi\right)}{d\vartheta} + \beta\Omega &= T_{in} - T_{fr} \operatorname{sgn}(\Omega) \\
 L_i \frac{dI_r}{dt} + M \frac{d}{dt}(I_s + I_t) + \frac{d\psi(\vartheta)}{d\vartheta} \Omega + I_r(R_i + R_l) &= 0 \\
 L_i \frac{dI_s}{dt} + M \frac{d}{dt}(I_r + I_t) + \frac{\psi\left(\vartheta + \frac{2}{3}\pi\right)}{d\vartheta} \Omega + I_s(R_i + R_l) &= 0 \\
 L_i \frac{dI_t}{dt} + M \frac{d}{dt}(I_r + I_s) + \frac{\psi\left(\vartheta - \frac{2}{3}\pi\right)}{d\vartheta} \Omega + I_t(R_i + R_l) &= 0
 \end{aligned} \right. \tag{2.45}$$

2.4.3 Parameters evaluation

In order to proceed to the simulation of the system, the parameters in Table 2.2 have to be determined. In general, there are different strategies that can be adopted in order to do so.

The determination of the phase resistance is straightforward since, as already discussed, it coincides with its DC value. The measured value of R_i is 14.3Ω , which is substantially the same as the value calculated by mean of the Ohm's law.

The calculation of the phase self inductance can be addressed in several ways. As can be observed, the coils configuration is unfavorable, since they are coreless and without any associated ferromagnetic loop (*cf.* Figure 2.8(d)). Recently, many authors proposed methods for the analytical calculation of planar coils self inductance with different shapes and layers [MdMHL99, PM08]. However, an analytic expression is not likely to be found with ease, especially as the coil shape becomes more complex.

Table 2.2 – Generator Parameters

Parameter	Symbol	Unit
Phase resistance	R_i	Ω
Phase inductance	L_i	H
Mutual inductance	M	H
Rotor moment of inertia	J	kg.m ²
Dry friction torque	T_{fr}	N.m
Viscous friction coefficient	β	N.m.s
Flux linkage	ψ	V.s

In such cases, numerical integration and/or analysis by mean of finite elements is an effective option [ER06, EPCLALLC05]. As a general rule, the computational cost becomes higher as the number of turns per layer increases and the spacing between them decreases. This topic will be addressed extensively in Chapter 5, while for this application the phase inductance was obtained via FEM and then measured using a precision impedance meter. The mutual inductance was also obtained using FEM, nevertheless an actual measurement was not possible because of the extremely low value. The results are reported in Table 2.3. As can be observed, the values are in the μH range. As a consequence, working frequencies up to hundreds of kHz would be necessary in order to obtain reactances comparable to the phase resistance. Such condition is unlikely to occur in MEMS electrical machines.

Table 2.3 – Phase self and mutual inductances (μH)

	FEM	Measurement
L_i	3.2	3.8
M	0.16	–

The rotor moment of inertia can be obtained with a simple calculation once the geometry and the material of the rotor yoke in the first hand and the magnet in the second hand are known.

$$J = 1.66 \cdot 10^{-10} \text{ kg.m}^2 \tag{2.46}$$

The calculation of the dry friction torque T_{fr} as well as the viscous coefficient β is a challenging task, since it is the result of the characteristics of the mechanical apparatus (bearings, crankshafts, lubrication, materials, fluid dynamics...) that is used for interacting with the rotor. As anticipated, despite significant research focused on the topic, it is almost impossible to rigorously evaluate such effects *a priori*. An experimental

Chapter 2. Modeling of MEMS synchronous machines

approach was therefore preferred. The rotor speed was set at a constant value, while the three phases were left open circuit. Under these conditions, the first equation in (2.45) can be rewritten as:

$$T_{in} = T_{fr} + \beta \dot{\vartheta} \quad (2.47)$$

The torque T_{in} was then measured for different velocities by mean of a dedicated sensor. As can be observed from Table 2.4, the measured value resulted constant at different speeds. One can thus conclude that in the considered range of velocities the contribution of the viscous term $\beta \dot{\vartheta}$ is negligible and that the measured torque basically coincides to the dry friction torque T_{fr} .

Table 2.4 – Torque measurements

Speed (rad.s ⁻¹)	Torque (μ N.m)
1.7	0.09
3.5	0.09
5	0.09

The final parameter to consider is the flux linkage between the phase coils and the permanent magnets. This usually requires two steps:

1. Determining the spatial distribution of magnetic induction field B
2. Calculating the flux of B through the coils in order to find ψ

For certain geometries of the magnet, an analytic expression for B can be found (see for example [KP13, CSJL13]). Nevertheless, due to absence of a ferromagnetic core, the integration on the coils surface is usually pursued numerically. The main alternative approach, that will be used in the following, is to use FEM to obtain the flux linkage starting only from the geometry and the material properties. This approach is usually computationally expensive, but it's also less prone to modeling errors and approximations. The flux linkage between the magnet and the coils of one phase for a rotation of 60 degrees (electrical period), is reported in Figure 2.10. For simulation purposes it is convenient to reconstruct the signal by mean of its harmonic components. For this application, 2 even harmonics are enough for the generation of a signal which is basically coincident with the original one (*cf.* Figure 2.10). One can write for the flux:

$$\psi(\vartheta) = \psi_1 \cos(p\vartheta) + \psi_3 \cos(3p\vartheta) \quad (2.48)$$

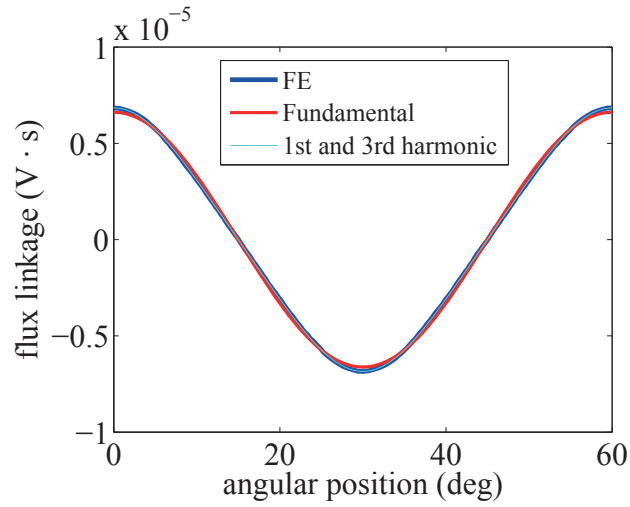


Figure 2.10 – Flux linkage between the magnet and the coils (one phase)

And for its derivative

$$\frac{d\psi(\vartheta)}{d\vartheta} = -p\psi_1 \sin(p\vartheta) - p\psi_3 \cos(3p\vartheta) \quad (2.49)$$

where

- $p = 6$ is the number magnetic poles pairs
- $\psi_1 = 0.662 \cdot 10^{-5} \text{ V}\cdot\text{s}$ and $\psi_3 = 0.022 \cdot 10^{-5} \text{ V}\cdot\text{s}$ are the magnitudes of the first and third order harmonic respectively ($\psi_2 \approx 0$).

Since the system is now completely defined, it is possible to proceed to the numerical simulations.

2.4.4 System simulations

The numerical simulation of interdependent equations like (2.45) might be a difficult task. First of all, as the scale of the device becomes smaller, the measurement units require more and more decimal digits, thus affecting the computational efficiency and eventually leading to numerical instability. An effective way to overcome this issue, is to define new arbitrary measurement units and rewrite the equations in a non dimensional form. The choice of the solver also plays an important role. Since the equations exhibit a certain degree of stiffness [Sha03], in the author experience

Chapter 2. Modeling of MEMS synchronous machines

the ode15s algorithm in the MATLAB library has to be preferred in order to gain computational efficiency.

Two different load conditions were simulated, open and short circuit, in order to simulate the device behavior as a generator. In both cases the input torque T_{in} was set equal to $0.18 \mu\text{N}\cdot\text{m}$.

Open circuit

First, the system was simulated in open circuit condition ($R_l = \infty$). In this case, no current is circulating ($I_r = I_s = I_t = 0$) and the electromagnetic torque is null as a result (*cf.* first equation in (2.45)). Hence, the external applied torque T_{in} and the dry friction torque T_{fr} are the only mechanical actions affecting the rotor dynamics. Since $T_{in} > T_{fr}$, the resulting torque is positive and constant over time, making the rotor speed increase linearly (Figure 2.11).

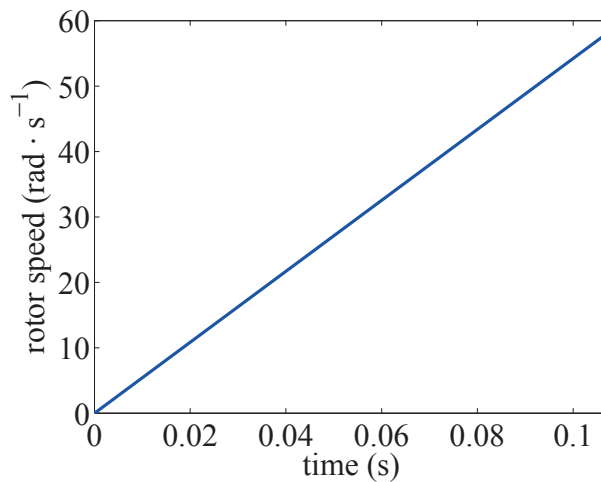


Figure 2.11 – Rotor speed (open circuit)

As the rotor speed increases, the induced voltage (the terms $\frac{d\psi}{d\vartheta} \dot{\vartheta}$) in each phase increases in magnitude and frequency as expected (Figure 2.12). This behavior goes on until the input torque is eventually balanced by the viscous friction that becomes more and more relevant at higher rotor velocities.

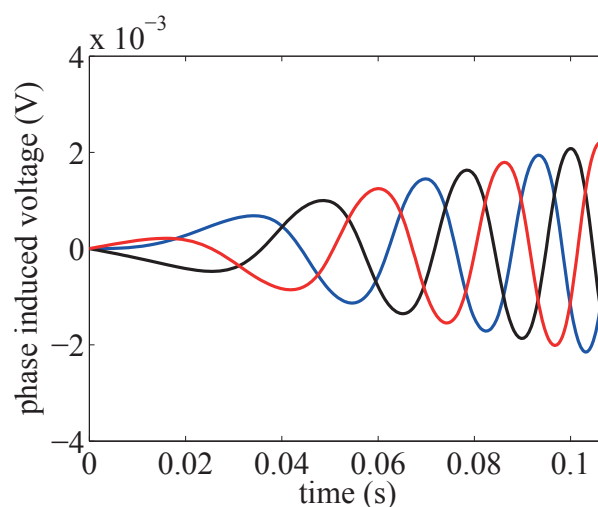


Figure 2.12 – Induced voltages for the three phases (open circuit)

Short circuit

Further simulations were performed putting the system in short circuit condition. In this case each phase has the lowest possible resistance, coincident with the inner resistance of the coils ($R_l = 0$). As the external torque is applied and the rotor is put into motion, an induced voltage is generated in each phase circuit. Due to the low resistance in the electric path, even small voltages lead to significant increase in the magnitude of the circulating current. As a result, in relatively small time span (less than 0.1 ms) the electromagnetic torque reaches the value needed to balance the input torque (Figure 2.13). Consequently, the rotor speed (Figure . 2.14) increases while the electromagnetic torque is smaller than the external torque, and then it stabilizes at a constant value, the latter depending on the input torque and on the constructive parameters of the generator. For the same induced voltage, coils with lower internal resistance develop higher electromagnetic torque at lower speed. As the speed becomes constant, the phase induced voltages also become constant in magnitude and frequency (Figure 2.15).

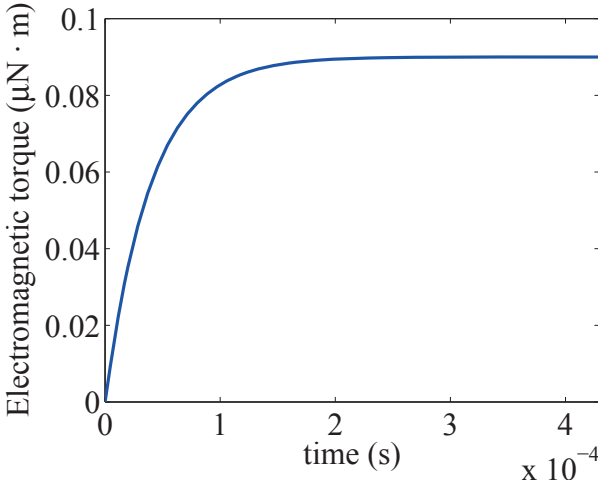


Figure 2.13 – Electromagnetic couple (short circuit)

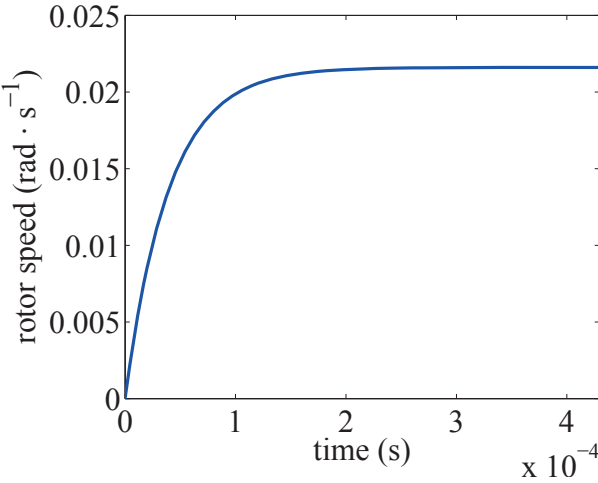


Figure 2.14 – Rotor speed (short circuit)

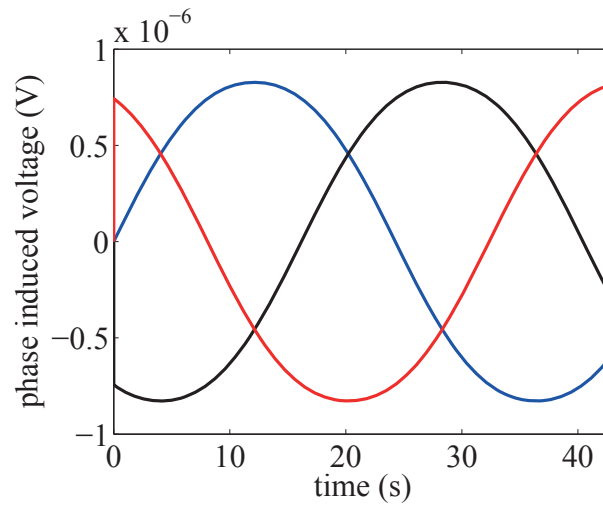


Figure 2.15 – Induced voltages for the three phases (short circuit)

2.4.5 Measurements and comparison

Some measurements were performed in order to validate the model. In particular, the induced voltage in one phase was measured in open circuit conditions, while the rotor speed was kept constant at different values. As can be observed in Figure 2.16 the induced voltage increases in amplitude and frequency as the the speed is increased, as expected.

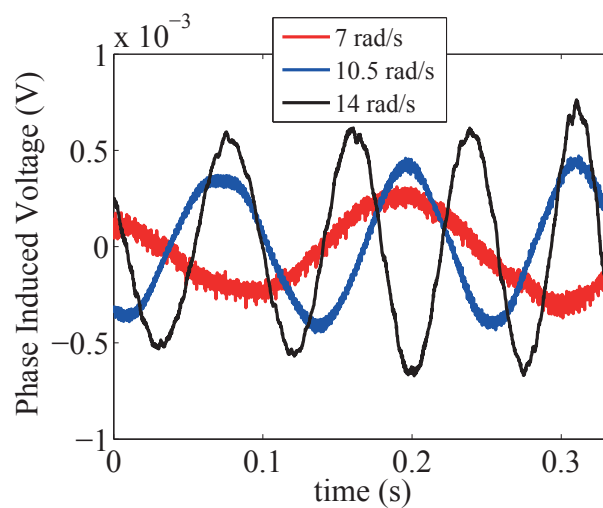


Figure 2.16 – Induced voltages at different velocities for one phase (timescale for reference only)

A significant parameter to be determined, is the phase constant of the generator k_{ph} ,

which links the rotor speed with the peak value of the induced voltage:

$$\hat{U}_i = k_{ph}\Omega \quad (2.50)$$

The theoretical value for k_{ph} , found throughout the model, is equal to $3.83 \cdot 10^{-5} \text{ V.s.rad}^{-1}$, while Table 2.5 summarizes the values measured at different velocities. As can be observed, the measured k_{ph} ranges from 3.60 to $4.05 \cdot 10^{-5} \text{ V.s.rad}^{-1}$, showing a maximum discrepancy with the theoretical value below 6%. This result validates the development so far. Moreover, the phase constant is particularly low, which further proves the dramatic impact of size reduction on magnetic related parameters. To give some reference, speeds in the order of 10^3 rad.s^{-1} would be necessary, for example, for the development of a sensorless electronic control based on induced voltage detection.

Table 2.5 – Phase constant at different speeds

Speed (rad.s^{-1})	k_{ph} (V.s)
7	$3.77 \cdot 10^{-5}$
10.5	$3.60 \cdot 10^{-5}$
14	$4.05 \cdot 10^{-5}$

2.5 Summary and conclusion

In this chapter the modeling of MEMS synchronous machines was addressed extensively. A comprehensive electromechanical model was derived starting from Hamilton's principle. Among the advantages of such approach, is the fact that the time-domain formulation makes the model suitable for the analysis of a wide variety of operating conditions, including generator and motor modes. In turn, the model is not suitable for the analysis of some parasitic effects, such as positioning torques and forces, which require the introduction of additional DOF in order to be taken into account.

On the basis of the scaling laws and the constructive features of MEMS machines, several conclusions concerning the characteristics of such devices were drawn. As the size decreases, the ratio between the phase reactance and resistance is dramatically worsened. In other words, the stator coils tend to behave as resistors rather than inductors. The practical consequence is that the design of the coils has to be addressed with particular care, since the impact on the device performances can be significant. Another key point is the substantial drop of the parameters associated with some sort of magnetic coupling due to the absence of ferromagnetic paths. This has strong consequences in terms of torque and induced voltage, in particular for their reluctant

contributions.

The device developed by Merzaghi *et al.* was then taken as a case study for model validation. Different strategies, based on analytical calculations as well as FEM, were adopted in order to determine the parameters of interest, which were later introduced into the model. Then, the governing equations were solved numerically in order to simulate the system under different operating conditions. Measurements of the phase constant at different speeds were performed, and the results were compared to the theoretical prediction showing good agreement.

Publications related to this chapter:

- J. Poliakine, Y. Civet and Y. Perriard, "Modeling and characterization of a MEMS synchronous generator," 2014 17th International Conference on Electrical Machines and Systems (ICEMS), Hangzhou, 2014, pp. 3492-3497.

3 MEMS Generator for the regulation of a mechanical movement

This chapter addresses the design of a small scale generator for the regulation of a mechanical movement. It gives insights on the preliminary choices that were made in terms of global configuration and shows how the electromechanical model derived in Chapter 2 can be used as an effective tool for the assessment of the generator functional constraints.

The dissertation will then focus on the definition of the objective function. In this context, the construction parameters and their influence on the device performances will be discussed extensively. On the basis of such analysis, a design algorithm is conceived and used for the optimization of the planar coils housed in the stator. In particular, the algorithm takes into account the technological risk associated to the fabrication process.

3.1 Technical requirements

The specifications for the future device were given by the industrial partner and are reported in Table 3.1. They are designed so that the microgenerator will be compatible with an existing control circuit provided by the industrial partner, and will have at the same time a size small enough to allow the implementation into a standard watch mechanism.

Table 3.1 – Technical requirements

	units	value
Rotor speed (controlled)	rad.s ⁻¹	33.5
Time for circuit start up	s	3
Max. total height	mm	2.21
Max. rotor diameter	mm	4.60
Max. stator diameter	mm	7.20
Output voltage at controlled speed	V	0.35
Input torque	μN.m	0.02 – 0.04

The desired rotor speed at steady state is equal to 33.5 rad.s⁻¹. Values of such relatively small entity are commonly used for watchmaking applications in order to limit friction and wear issues that may arise at higher velocities. To the author knowledge, such limit has never been demonstrated on the basis of a rigorous mathematical model. Nevertheless, its existence has a solid empirical validation consolidated by several decades of watchmaking practice. In terms of design, the main implication is that, regardless of the type of generator and its transduction principle, the device will operate at very low frequencies. Assuming the electrical frequency to be a multiple of the mechanical one, operational frequencies in the range of tens of Hz should reasonably be expected. This heavily affects the generator choice, since not all the transduction principles perform equally in the same frequency range. The time for the circuit to start up, can be interpreted as constraint on the maximum length allowed for the system to reach its controlled state. In practice, this affects the mechanical dynamics of the system, which has to be designed for a quick response. By observing the size constraints, it appears evident that the technology involved for the fabrication of the device has an important role, and has to be taken into account from the beginning of the design. In fact, the outer dimensions of the generator are in the mm range, which entails inner features in the μm range. Another particular binding constraint is related to the output voltage of the generator. As it emerges from Table 3.1, the electrical power output has to be produced ensuring a voltage of at least 0.35 V at the controlled speed of 33.5 rad.s⁻¹. This is motivated by the specifications of the command circuit. In fact, the latter needs to be supplied in direct current, while the generator produces an alternate current. For this reason the electronic command provides a voltage multiplier/rectifier to shape the signal properly which is essentially composed by

transistors whose threshold tension coincides with the given value. Because of the reduced size of the generator, together with the low operational frequencies, the voltage constraint appears to be quite challenging, and therefore it will be a driving parameters for the development of the solution. Finally, it should be noted that the input torque to be balanced is not constant. This is due to the fact that it depends on the energy stored in the barrel, which is far from being constant. The design routine will consider this fact as well.

3.2 Preliminary design choices

3.2.1 Generator features

A scheme of the generator of topology is represented in Figure 3.1. As can be observed, an axial flux topology was preferred over a radial one. This choice complies much better with the technical requirements, which constrain heavily the height of the device (*cf.* Table 3.1). In this sense, an axial flux topology entails a basically horizontal layout, thus allowing a better exploitation of the space available in the watch movement. Moreover, this eases the fabrication using MEMS technologies, which are particularly suited for 2D-like structures. The absence of salient poles, simplifies *a priori* the fabrication as well and it also allows the suppression of the reluctant contributions to the overall torque (*cf.* equation (2.28)), which are definitely unwanted for the given application. This is particularly true for parasitic positioning torque and forces appearing in absence of current in the stator windings.

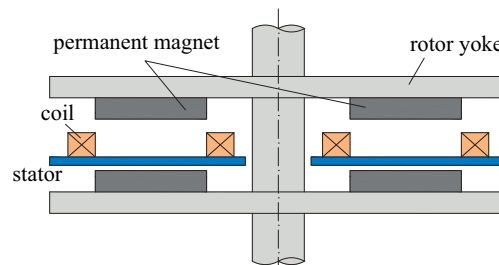


Figure 3.1 – Retained solution: rotational electromagnetic generator with PMs as the primary excitation source.

The rotor yoke is ferromagnetic and it implements a multi-pole ring shaped magnet including a number p of magnetic pole pairs with alternating polarization (Figure 3.2). The determination of the number of yokes as well as the number of magnetic pole pairs will be discussed in detail in the context of the rotor optimization. From a technological viewpoint, the rotor will not be fabricated using MEMS technologies. In particular, the magnet will be fabricated using traditional sintering techniques, following a pick and place approach. While this choice does not serve well the purpose of process integration, it is motivated by the fact that the properties of microfabricated

Chapter 3. MEMS Generator for the regulation of a mechanical movement

magnets keep being relatively poor, although a great effort is currently being dedicated to their enhancement (see for example [per03, Ueh04, JPB⁺16]).

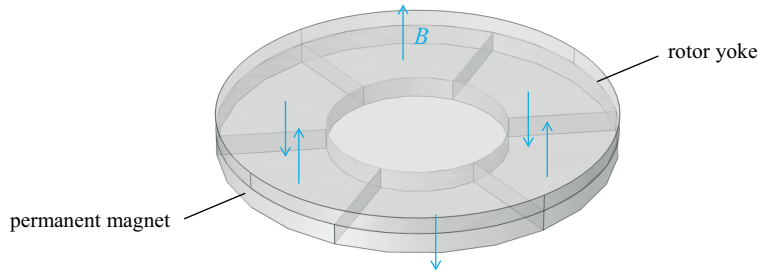


Figure 3.2 – Rotor yoke and its ring shaped permanent magnet with alternating axial magnetization.

Another main choice that was done at the early stages of the project, concerned the number of rotor yokes. A single yoke configuration (Figure 3.3(a)), similar to the one adopted by Merzaghi (*cf.* section 2.4), presents the advantage of a simpler assembly. Furthermore, with respect to a double yoke configuration (Figure 3.3(b)), the absence of the rotor axis facilitates the design of the coils shape. In turn, the magnetic coupling (and hence the device performances) is expected to decrease because the permeance associated to the magnetic field is increased. In order to quantify such effect, a finite element simulation, carried out considering a magnet with 3 magnetic pole pairs and an air gap of 300 μm , was launched in order to calculate the induction in the air gap in the two cases. The results are reported in Figure 3.4, which depicts the induction along a straight line starting from the center of one magnet sector.

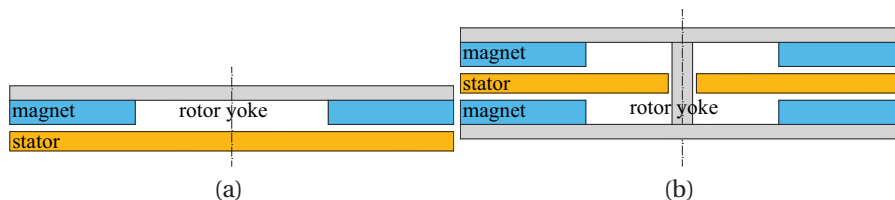


Figure 3.3 – Possible rotor configuration: (a) single yoke and (b) double yoke.

As can be observed, the double yoke performs far better in terms of induction magnitude. Assuming that the stator is placed in the middle of the air gap, at a distance of 150 μm from the magnet(s) surface, using a single yoke makes the induction magnitude drop of about 60%. In addition to that, the induction magnitude decreases as the distance from the magnet increases, thus complicating the design as well as the positioning of the stator during the assembly. Finally, in the double yoke configuration the magnetic field is more confined (see Appendix B), which reduces the risk of parasitic mechanical interactions with surrounding high permeance materials.

As for the coils, two different approaches for the fabrication were considered. The

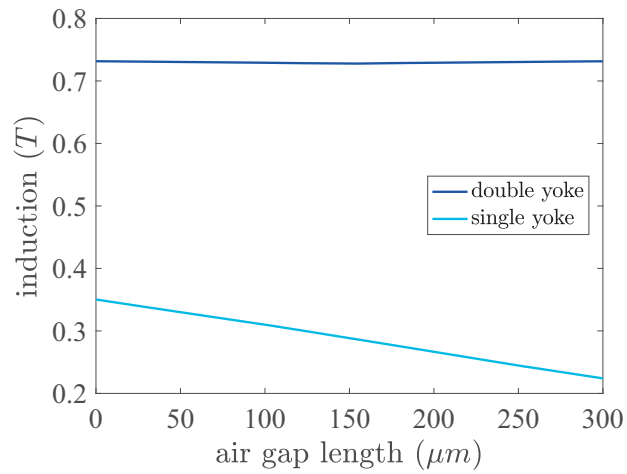


Figure 3.4 – Magnetic induction in the air gap (300 μm) for single and double yoke systems ($p = 3, B_0 = 1.2$ T).

first method was proposed by [BKB⁺09] in 2009. His group developed a technique for the manufacturing of 3D coils in which polymeric posts are first fabricated on a substrate using UV or X-ray lithography and a wire bonder is subsequently used for winding an isolated conductor around them (Figure 3.5).

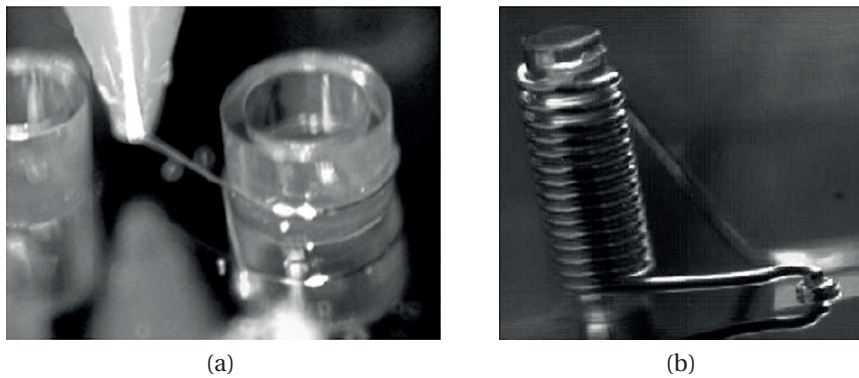


Figure 3.5 – Wire bonder manufacturing technique [BKB⁺09]: (a) copper conductor wiring and (b) a completed coil.

Despite its attractiveness, such technique was considered as problematic for a number of reasons. First of all, the circular shape of the coils is not suited for maximizing the magnetic coupling with a ring shaped multi-pole magnet, for which purpose trapezoidal or triangular shape should be adopted. Also, multiple layers of wire turns (and a significant number of them) proved to be necessary in order to obtain a sufficient magnetic coupling. Although in principle the wire bonding technique enables such possibilities, these were never actually tested and the technique was abandoned. Instead, it was chosen to use a more standard clean room process in order to fabricate

Chapter 3. MEMS Generator for the regulation of a mechanical movement

planar coils by superposing several layers of patterned conductor (Figure 3.6) on a silicon substrate. Such approach has been successfully adopted for a wide variety of applications, including MEMS machines (see for example [DAZ⁺05, HJA08, MKP11]). One of the main advantages of this strategy is that the coils can be shaped in virtually any form without significant modifications to the process flow. Moreover, it offers more freedom in terms of conductor size (the wire used in the wire bonding process has a diameter of 25 μm). Finally, a 2D-like structure for the windings is also more suitable for the purpose of reducing the device height. In principle, this kind of coils could also be manufactured using printing technologies [KLD15], with significant benefits in terms of costs and prototyping throughput. A preliminary analysis unveiled however that, despite the intense ongoing development, these techniques are still immature for the application. In particular, the relatively poor resolution (in the range of tens of microns) limits the achievable turns density while the conductor thickness, usually limited to hundreds of nm, would translate into small sections and excessive ohmic losses as a consequence.

In this chapter, the focus will be on the optimization in the context of the MEMS generator rather than the fabrication, which in turn will be addressed extensively in Chapter 4 and 5.

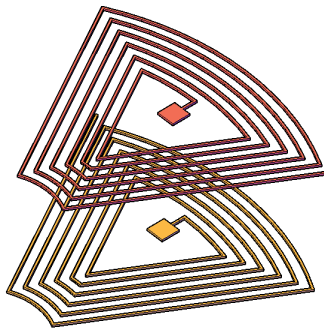


Figure 3.6 – Schematic of a multilayer coil.

3.2.2 Single-phase vs three-phase

In order to put the design routine on track, a particularly important choice is the number of phases of the device. In this sense, the most interesting cases to consider are a single-phase and a three phase generator. In fact, single-phase is the most basic configuration while three-phase systems are commonly used in all of sort of applications as they present significant advantages in terms mechanical stability, as will be demonstrated in the following. A first comparison can be made on the basis of the model obtained in Chapter 2, using the systems of equations (2.25) and (2.33). For a device of the type presented in Figure 3.1, the following observations can be done.

3.2. Preliminary design choices

- No modification of magnetic paths is associated with the rotor angular position. This entails that all the terms of the type $\frac{dL_i(\vartheta)}{d\vartheta}$, $\frac{dM(\vartheta)}{d\vartheta}$, $\frac{d\Lambda_e(\vartheta)}{d\vartheta}$ are equal to zero.
- Being a small scale device in which magnetic fluxes are very little guided (cf. paragraph 2.3), reactances are several orders of magnitude lower than the corresponding resistances.
- For the same reason, mutual inductances between coils of different phases are even smaller and therefore negligible.
- Due to the low operating speed, viscous friction effects are negligible as well ($\beta = 0$). Dry friction will not be considered either since it does not depend on the number of phases, which is the object of the present analysis.

It will also be assumed that the terms $\frac{d\psi}{d\vartheta}$ are purely sinusoidal and proportional to the phase constants k_{ph} . For the three-phase device it will be assumed to be symmetric, so that each phase has the same impedance ($R_r = R_s = R_t = R_i$; $L_r = L_s = L_t = L_i$) and the induced voltages have an electric phase shift of $\frac{2}{3}\pi$. Finally, the generators will be assumed to be in short circuit (load resistance R_l equal to zero). The evolution equations for the two generators can thus be rewritten as in (3.1) (single-phase) and (3.2) (three-phase).

$$\begin{cases} J\dot{\Omega} + k_{ph} \sin(p\vartheta)I = T_{in} \\ L_i \frac{dI}{dt} - k_{ph} \sin(p\vartheta)\Omega + R_i I = 0 \end{cases} \quad (3.1)$$

$$\begin{cases} J\dot{\Omega} + I_r k_{ph} \sin(p\vartheta) + I_s k_{ph} \sin\left(p\vartheta + \frac{2}{3}\pi\right) + I_t k_{ph} \sin\left(p\vartheta - \frac{2}{3}\pi\right) = T_{in} \\ L_i \frac{dI_r}{dt} + k_{ph} \sin(p\vartheta)\Omega + I_r R_i = 0 \\ L_i \frac{dI_s}{dt} + k_{ph} \sin\left(p\vartheta + \frac{2}{3}\pi\right)\Omega + I_s R_i = 0 \\ L_i \frac{dI_t}{dt} + k_{ph} \sin\left(p\vartheta - \frac{2}{3}\pi\right)\Omega + I_t R_i = 0 \end{cases} \quad (3.2)$$

In order to obtain an exhaustive analysis, each configuration should be completely optimized before the simulation. At this stage however, the aim is rather to evaluate the

Chapter 3. MEMS Generator for the regulation of a mechanical movement

performances qualitatively and verify if one configuration is *a priori* more suitable for the fulfillment of the technical requirements. In order to do so, some entry values for the model parameters will be chosen for the single-phase generator and subsequently adapted for coherently describing the three-phase device. The number of magnetic pole pairs p was arbitrary set equal to 3 for both generators. Although such parameter is highly significant for the generator performances, it has no particular relevance in the context of the preliminary analysis that is here being conducted. For two devices of the same size, housing the same overall length of conductor with the same section and material, the resistance of one phase R_i in the three-phase setup can be assumed to be one third than the single-phase one, since the same ohmic losses are split between the three phases. If the coils number is also the same, the same consideration can roughly be applied to the phase inductance L_i . Finally, the phase constant k_{ph} is proportional to flux linkage between the magnet and the coils, which in turn is proportional to the active surface available. Since the surface is split between three phases, other conditions being the same, the phase constant in the three-phase can be assumed to be one third than the single-phase one as well. The input torque was set equal to $0.04 \mu\text{N.m}$. The numerical values used for the simulation are reported in Table 3.2.

Table 3.2 – Entry values for preliminary simulations

	units	single-phase	three-phase
p	–	3	3
R_i	$\text{k}\Omega$	30	10
L_i	mH	15	5
k_{ph}	V.s	0.0104	0.0035
T_{in}	$\mu\text{N.m}$	0.04	0.04

The results from the dynamic simulation are reported in Figure 3.7, 3.8 and 3.9, which report the rotor speed, induced voltage and electromagnetic torque for the two configurations. As can be observed, the basic evolution path is the same. In a first phase the rotor speed increases under the action of the input torque. This causes the output voltage to increase accordingly in magnitude and frequency. As a result, a current starts circulating in the coils, thus generating an electromagnetic torque. Eventually, the system reaches its steady state. In this condition, the electromagnetic torque balances the input torque and as a consequence the rotor speed becomes constant (so does the back EMF).

Although the general dynamics is quite similar, several major differences exist between the two configurations. A first aspect to be considered is that the output voltage (Figure 3.8) is significantly higher in the single-phase configuration. This is a direct consequence on the assumptions made for the estimation of the phase constant. This as to be regarded as a meaningful advantage, since as discussed in paragraph 3.1, obtaining a relatively high output voltage is among the main requirements of the

3.2. Preliminary design choices

application. As can be observed from Figure 3.9, at steady state the overall torque matches the input torque value of $0.04 \mu\text{N.m}$. However, while in the three-phase generator, the phase shift between the induced voltages results in a smooth couple characteristic, in the single-phase configuration the shape is rather periodical with a non-null component equal to the input torque. The effects can also be appreciated in terms of rotor speed (Figure 3.7(a)), which even at steady state presents some ripples. This behavior is undesired in the context of the present application, since it complicates the conception of the control system. Nevertheless, the advantage of a single-phase generator in terms of output voltage magnitude was considered as determinant, and a single-phase configuration was retained.

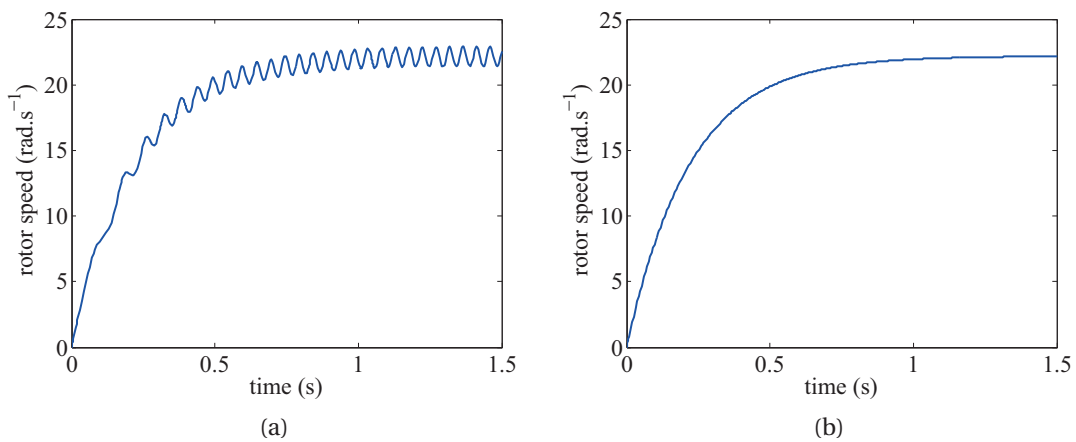


Figure 3.7 – Simulated rotor speed for the two configurations: (a) single-phase and (b) three-phase.

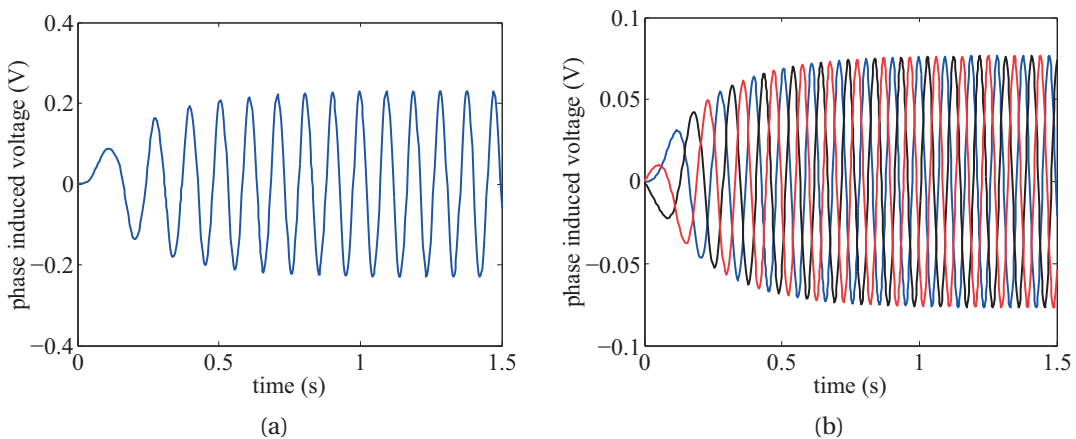


Figure 3.8 – Simulated back EMF for the two configurations: (a) single-phase and (b) three-phase.

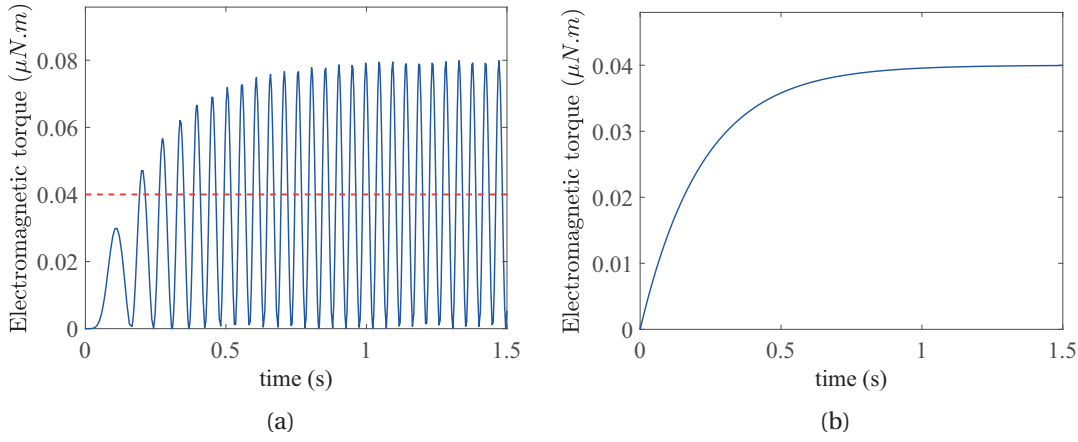


Figure 3.9 – Simulated electromagnetic torque for the two configurations: (a) single-phase and (b) three-phase.

3.2.3 Controlled state simulation

Once the single-phase configuration was selected, other simulations were run with the aim of testing the braking principle and potentially obtaining additional requirements in order to ensure the overall functionality of the device. In order to do so, a fictitious control system was numerically implemented in the model. This was done as follows.

In the first stage of the simulation the generator was left open circuit ($R_l \gg R_i$) for three seconds. According to the technical requirements (*cf.* Table 3.1), in such interval the circuit is supposed to start up. From a functional point of view, this means that the rotor must have surpassed the targeted speed of 33.4 rad.s^{-1} . This translates into an additional constraint on the rotor moment of inertia J . In fact, since no current is circulating, the electromagnetic (*i.e.* braking) torque is zero and the rotor mechanical equation can be rewritten as

$$J\dot{\Omega} = T_{in} \quad (3.3)$$

which upon integration, and introducing the start up time t_{start} and the targeted speed Ω_{target} leads to the following condition:

$$J \leq \frac{T_{in} t_{start}}{\Omega_{target}} \quad (3.4)$$

3.2. Preliminary design choices

Considering the lowest value for the input torque, which is equal to $0.02 \mu\text{N}\cdot\text{m}$, (3.4) gives an upper limit for the rotor moment of inertia of $1.8 \cdot 10^{-9} \text{kg}\cdot\text{m}^2$. A quick analysis based on the device size and the materials involved allows to estimate actual values of the order of $10^{-10} \text{kg}\cdot\text{m}^2$. For the simulation purposes J was set equal to $4 \cdot 10^{-10} \text{kg}\cdot\text{m}^2$.

In the second stage, the system was suddenly short circuited ($R_l = 0$). Even if the electronic command is not described, this operating condition mimics a controlled mode, in the sense that the circulating current reaches its maximum value, and so does the electromagnetic torque. In order to take into account the most critical conditions, the input torque was set equal to its highest value of $0.04 \mu\text{N}\cdot\text{m}$. As for the remaining parameters (*cf.* equations (3.1)), the phase constant was supposed to match its required value ($0.0104 \text{V}\cdot\text{s}$). As for the viscous friction, the coefficient β was arbitrarily put equal to $3.34 \cdot 10^{-11} \text{N}\cdot\text{m}\cdot\text{s}$. Finally, in order to take into account for the inner resistance, the simulation was repeated varying its value between 20 and 500 k Ω . The rotor speed is reported in Figure 3.10.

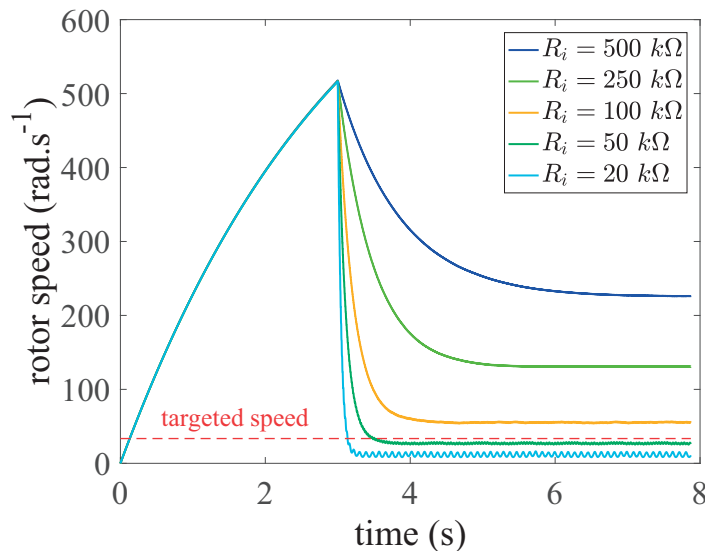


Figure 3.10 – Controlled behavior and targeted speed.

As can be observed, in open circuit the rotor speed increases linearly under the action of the input torque. The trend changes slightly due to the influence of viscous friction, which becomes more significant as the speed increases. When the generator is suddenly short circuited ($t = 3 \text{s}$), the electromagnetic torque that is generated is higher than the input torque and as a result the speed (as well as back EMF and current) starts decreasing until a dynamic equilibrium is reached and the speed becomes constant. The system is inherently stable, nevertheless the speed at which the steady state is attained depends on the coil resistance. The physical explanation is straightforward. Since the electromagnetic torque is linked to the current, if the phase constant is the same and the resistance is higher, higher induced voltages (*i.e.* higher velocities) are

needed in order to generate the same torque. For the application of interest, the aim is to control the speed at 33.5 rad.s^{-1} . As a consequence, in order to brake effectively, the electromagnetic torque must overcome the input torque at velocities below this limit. As depicted in Figure 3.10, this requirement is fulfilled for resistances around $50 \text{ k}\Omega$. In general, lower resistances lead to more efficient control of the device. For this reason, the actual targeted value was set equal to $30 \text{ k}\Omega$. It is also worth noticing that the speed ripples put into evidence in the previous paragraph are more prominent at low speed, while at the targeted value they become less than an issue. Table 3.3 reports the updated functional constraints.

Table 3.3 – Updated functional constraints

	units	value
phase constant	V.s	≥ 0.0104
total height	mm	≤ 2.21
rotor diameter	mm	≤ 4.60
stator diameter	mm	≤ 7.20
inner resistance	$\text{k}\Omega$	$\leq 50 (\leq 30)$
rotor moment of inertia	kg.m^2	$\leq 1.8 \cdot 10^{-9}$

3.3 Optimization

3.3.1 Construction parameters

Rotor

The rotor construction parameters are reported in Table 3.4, while Figure 3.11 represents visually the same parameters on an axisymmetric cross section of the rotor. The materials employed influence the performances as well, but they do not necessarily have to be included in the optimization routine. For what concerns the magnet, the magnetization curves are often not available for commercial products of the type used in this study. Considering that in MEMS application the operational currents (and hence the associated magnetic fields) are usually low, high remanence must be preferred over high coercivity. As for the rotor yoke, the higher the material permeability is, the better the performances are.

In practice, all the parameters listed in Table 3.4, influence intensity and distribution of magnetic induction in the air gap, except for the shaft radius, which only affects the shape of the coils (see Appendix B).

Table 3.4 – Rotor construction parameters

	units	symbol
Air gap	mm	h_t
Yoke outer radius	mm	r_y
Yoke thickness	mm	h_y
Shaft radius	mm	r_{sh}
Magnetic pole pairs	–	p
Magnet outer radius	mm	r_{em}
Magnet inner radius	mm	r_{im}
Magnet thickness	mm	h_m

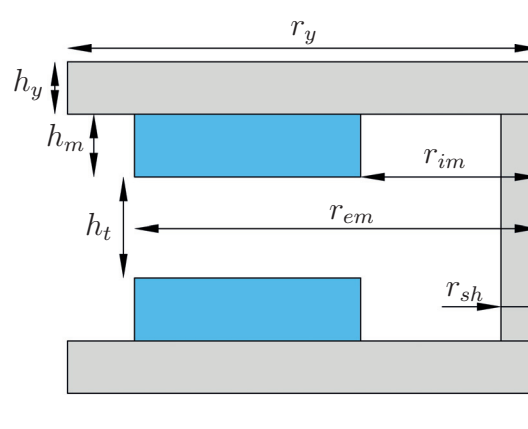


Figure 3.11 – Cross section of the rotor and main construction parameters.

Stator

Figure 3.12 reports a sketch of a planar coil that will be fabricated for the generator. As can be observed, the shape is quite complex. The outline is that of a circular trapezoid. Such form maximizes the active surface with respect to one magnetic pole and allows for the rotor shaft to pass through the stator. At the same time, in order to maximize the number of turns per coil, the turns shape shifts to a circular sector as the available room decreases. Figure 3.13 represents a cross section of two adjacent turns. The horizontal encumbrance e is obviously not an independent parameter, but since it will be used extensively in the following development, it is here put in evidence. All the relevant parameters are reported in Table 3.5. As for the materials, the same line of reasoning seen for the rotor applies, in the sense that the lower the resistivity, the better the performances.

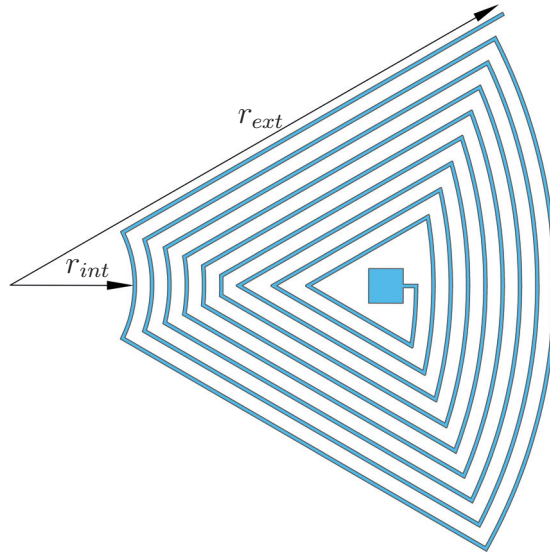


Figure 3.12 – Shape of a planar coil (one layer).

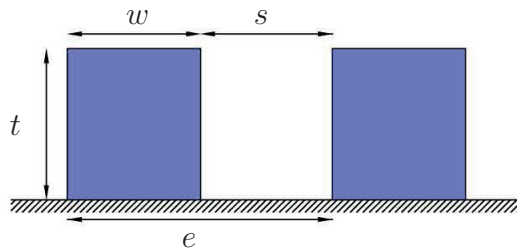


Figure 3.13 – Cross section of two adjacent turns.

Table 3.5 – Stator construction parameter

	units	symbol
number of turns per sector	–	n_s
number of layers	–	n_l
turn width	μm	w
turn thickness	μm	t
turn spacing	μm	s
horizontal encumbrance	μm	e
outer radius	mm	r_{ext}
inner radius	mm	r_{int}

3.3.2 Definition of the objective function

In order to discuss the generator optimization, it is convenient to develop a bit more the expression of the phase constant k_{ph} , which in the previous paragraphs was just arbitrarily set equal to a given value. In order to do so, the development seen in

paragraph 2.2.3 can be used. Considering just one harmonic component, the magnetic flux between the magnet and the stator coils and its derivative with respect to the rotor angular position can be expressed as

$$\begin{aligned}\psi(\vartheta) &= \hat{\psi} \cos(p\vartheta) \\ \frac{d\psi(\vartheta)}{d\vartheta} &= -p\hat{\psi} \sin(p\vartheta)\end{aligned}\tag{3.5}$$

and the final model can thus be rewritten as

$$\begin{cases} J\dot{\Omega} + p\hat{\psi} \sin(p\vartheta)I + \beta\Omega = T_{in} - T_{fr} \operatorname{sgn}(\Omega) \\ L_i \frac{dI}{dt} - p\hat{\psi} \sin(p\vartheta)\Omega + (R_i + R_l)I = 0 \end{cases}\tag{3.6}$$

As already discussed in Chapter 2, the optimization of the purely mechanical parts of the system can often be addressed independently with respect to the electromagnetic ones. The aim is usually to minimize viscous and dry friction effects, which are definitely undesired in the vast majority of application. In the present application, viscous effects are assumed negligible due to the very low speed of operation, while the dry friction depends entirely on the features of the watch movement. As for the moment of inertia J , it does have an upper limit (*cf.* paragraph 3.2.3). However, since the latter is not particularly constraining, its compliance to the functional requirements can be verified after the general optimization of the generator. In this sense, the electrical and electromagnetic parameters are actually defining the generator performances.

The optimization procedure has to pass through the definition of one or multiple objective functions. In general, the choice is arbitrary and depends on the application. Typical objective functions include electromagnetic torque, power output and so on. For a generator of the type considered, a general objective function can be expressed in the following form:

$$f_{obj} = \frac{(p\hat{\psi})^i}{\left(\sqrt{R_i^2 + (p\Omega L_i)^2}\right)^j} \approx \frac{(p\hat{\psi})^i}{R_i^j}\tag{3.7}$$

where, the last approximation is legit whenever $R_i \gg L_i$ (as it is likely to be for a MEMS

Chapter 3. MEMS Generator for the regulation of a mechanical movement

device). In other words, the device performances are defined by a particular ratio between the phase constant and the inner impedance, defined by the coefficients i and j (both assumed to be positive). Equation (3.7) basically expresses a compromise between the electromagnetic coupling between the rotor and the stator, and the losses that are generated in order to obtain it. In this sense i and j have to be intended as priority coefficients. Choosing i higher than j means that higher ohmic losses are tolerated as long as the electromagnetic coupling is enhanced (and vice versa). For obvious reasons, equations (3.7) cannot be considered as exhaustive of any possible objective function. Nevertheless, a great variety of criteria can be represented in such form (see for example [DBP17]). In particular, Table 3.2 reports some significant combinations of the priority coefficients with their physical interpretation.

Table 3.6 – Significant priority coefficients combinations

i	j	physical meaning
1	0	back EMF
0	1	ohmic losses
1	1	current, power output
2	1	electromagnetic torque

As discussed, the most binding objective is a back EMF of 0.35 V at the speed of 33.5 rad.s⁻¹ which translates into a phase constant of 0.0104 V.s. Hence, the back EMF was considered as the primary objective function:

$$f_{obj} = p\hat{\psi} \quad (i = 1; j = 0) \quad (3.8)$$

Maximizing equation (3.8) in compliance with the boundaries specified in Table 3.3 is in principle enough to ensure the functionality of the device. In turn, this strategy does not guarantee that the generator will be the best performing among all the functional ones. In order to push the design in this sense, a secondary objective function is considered. In particular, in order to enhance the braking performances, the electromagnetic torque was chosen:

$$f_{obj} = \frac{(p\hat{\psi})^2}{R_i} \quad (i = 2; j = 1) \quad (3.9)$$

The reason why this function was not chosen in first place is that an optimization based on (3.8), allows to obtain an entry configuration which also minimizes the

technological effort for the fabrication. In order to clarify this concept, it is convenient to analyze the construction parameters and how they affect the expressions of $p\hat{\psi}$ and R_i .

3.3.3 Optimization variables

As discussed in paragraph 3.3.2, a wide variety of objective functions can be expressed in the form (3.7). It follows that any optimization routine must pass through the estimation of the inner resistance R_i and the phase constant $p\hat{\psi}$. The resistance only depends on the coils characteristics and can be expressed in a purely analytic form. For a single phase generator comprising planar coils with n_l layers, in the same number $2p$ of the magnetic poles, the overall resistance as:

$$R_i(p, n_l, n_s, r_{ext}, r_{int}, w, s, t) = 2pn_l R_i^{sec} = 2pn_l \sum_k^{n_s} \rho \frac{l(p, k, r_{ext}, r_{int}, w, s)}{tw} \quad (3.10)$$

where R_i^{sec} is the resistance of one sector (*i.e.* one single layer coil, as in Figure 3.12), k indexes the turns, l is the length of each turn and ρ the material resistivity. (3.10) can be conveniently rearranged as in (3.11), by considering that the conductor length (assumed to be coincident with the average line) is the same for turns with the same horizontal encumbrance. This reduces the evaluation domain of the most cumbersome part of the equation to 5 variables. The evaluation of (3.11), is not computationally expensive, even for a high number of turns.

$$R_i = 2pn_l \frac{\rho}{tw} \sum_k^{n_s} l(p, k, r_{ext}, r_{int}, e) \quad (3.11)$$

The phase constant depends on both coils and rotor characteristics. Its evaluation requires in first place the evaluation of the magnetic induction in the air gap B , for which one can write:

$$B = B(\vec{r}, p, r_{em}, r_{im}, h_m, h_t, r_y, h_y, r_{sh}) \quad (3.12)$$

where \vec{r} is a spatial vector. Note that the term B is a scalar, and designates here the axial component of the induction field (*i.e.* the component that is significant for the determination of the flux linkage).

Then, B has to be integrated on the coils surface in order to obtain the phase constant. As in the previous case, for coils comprising a total number of $2pn_l$ sectors, the phase constant can be written as

$$p\hat{\psi} = 2p^2n_l\psi_{sec} \quad (3.13)$$

where ψ_{sec} is the flux coupled to one sector. The writing (3.13) is a legit approximation as long as different layers see the same induction field. This is likely to be the case in a double yoke configuration (*cf.* Figure 3.4). The phase constant can thus be written as

$$2p^2n_l\psi_{sec} = 2p^2n_l \sum_k^{n_s} \int_{S_k} B(\vec{r}, p, r_{em}, r_{im}, h_m, h_t, r_y, h_y, r_{sh}) dS \quad (3.14)$$

where $S_k = S_k(p, k, r_{ext}, r_{int}, w, s)$ is the surface of the k -th turn. Unlike the inner resistance, the phase constant is in general difficult to handle. The main reason is that while B in the air gap can be considered as constant along the axial direction, it cannot be considered as such in the radial direction. Moreover, because of the complex form of the coreless coils, expression (3.14) has to be evaluated for each turn individually. If this is done using FEM, which is likely to be the case for the aforementioned reasons, the computational time becomes important.

3.3.4 Variables reduction

As it can be deduced from expressions (3.10) and (3.14), an objective function of the form $\frac{(p\psi)^i}{R_i^j}$ depends on 15 constructions parameters, including both continuous and discrete variables (*e.g.* the number of turns and layers). In absence of a comprehensive analytic expression, an empirical model could be envisioned. The method basically consists in evaluating the function of interest at given points and then using some regression technique in order to interpolate the data. There is a vast literature addressing such matters. In particular, the design of experiments theory (see for example [BL59, PP13]) focuses on reducing the evaluation points while maximizing the level of information that can be gained. The problem with such approach is that even with a reduced number of points, the number of evaluations will still be $(n_{points})^{15}$, so that even the sparsest grids will result in at least in $\sim 10^8$ simulations. As a consequence, disregarding the method that will be used for the actual optimization of the device, the number of variables has to be reduced. This can be done by analyzing *a priori*

their impact on the overall performances, the constraints between different variables in order to eliminate redundancy and, finally, by taking into account technological factors. This procedure entails an overall loss of generality, since the criteria are strictly related to the objective function of interest. For example, cutting out from the optimization process the height of the rotor yoke, is totally reasonable (as will be discussed shortly) for this application, but it would be misleading if minimizing the total height of the device was among the declared objectives. For several construction parameters, the impact was assessed from the analysis of a simplified magnetic circuit. In order to increase readability, only the conclusions will be reported here, while motivated readers are invited to refer to Appendix C for a more rigorous treatise.

- The smaller is the air gap h_t , the higher is the associated permeance Λ_δ (cf. equation (2.40)) and, consequently, the magnetic field. Hence, a crude but effective strategy is to perform the optimization with the air gap locked at a given value. In this study, the air gap was set equal to 200 μm . Such value was considered as prudential from a technological standpoint, considered that for example, the device by Merzaghi analyzed in Chapter 2 has an air gap of 75 μm .
- Similar considerations apply to the geometric parameters of the magnet. A larger surface allows to enhance the magnetic coupling with the stator. Hence, the outer radius of the magnet r_{em} is put equal to the maximum allowed by the size constraints, while the inner radius r_{im} as small as possible. This coincides with the radius of the rotor shaft. In general, increasing the magnet thickness boosts the magnetic coupling as well. It should be noted however that in practice, because the magnet is a commercially available one, there is limited control over such parameters. The magnet that was actually used is made of NdFeB, has an outer radius of 2.3 mm, an inner radius of 1.05 mm and a thickness of 250 μm .
- The yoke role is to offer a high permeance path to the magnetic field generated by the magnet. The permeability of its ferromagnetic material is thus expected to be 2 or more orders of magnitude higher with respect to the air gap and the magnet. As a consequence, as long as the yoke thickness h_y is comparable with the magnet and the air gap thicknesses, the associated permeance is basically negligible and so is its influence on the device performances.
- As for the yoke radius r_y , any configuration providing $r_y < r_{em}$ has to be considered as aberrant, since it is likely to increase magnetic field leakage (cf. Figure 3.11). At the same time, if $r_y \gg r_{em}$ is chosen, the extra length will not contribute to lower the reluctance of the ferromagnetic path. It can therefore be assumed that a reasonable design choice is to put $r_y \approx r_{em}$.
- The rotor shaft influences the shape of other parts of the rotor (e.g. the magnet), but because of the symmetries of the system, it does not affect directly the induction field B . In the following, its diameter will be assumed equal to 1.0 mm.

Chapter 3. MEMS Generator for the regulation of a mechanical movement

The variables are thus reduced to 8, summarized in the array x below.

$$x = (p, n_l, n_s, t, w, s, r_{ext}, r_{int}) \quad (3.15)$$

A final consideration concerns the number of magnetic pole pairs p . In line of principle, such variable affects significantly the performances of the device, and cannot be suppressed by making general assumptions. For this particular application however, choosing $p = 3$ offered several practical advantages. In first place, a ring shaped magnet with such characteristics was practically available. Secondly, the existing electronic command was designed for operating at an electrical frequency of 16 Hz, which is a submultiple of the reference frequency provided by the quartz crystal (32 kHz). At the targeted speed of 33.5 rad.s^{-1} , 16 Hz are obtained, in fact, with $p = 3$ (*cf.* equation (3.6)).

Based on the above considerations, one can observe that the optimization problem is basically reduced to the optimization of the stator, since all the variables related to the rotor are constrained or assigned *a priori*. Such will be the subject of the next section.

3.3.5 Optimization routine

As already stated in paragraph 3.3.2, the design objectives are as follows:

- Maximizing the output voltage
- Enhancing the electromagnetic torque
- Simplifying the fabrication

The question that remains open at this point, is how to take into account for the fabrication issues while designing the generator. In fact, any routine which does not consider the actual technological possibility is likely to converge towards solutions which are not actually feasible. As for example, hundreds of conductor layers or disproportionately large sections. In order to overcome these issues, the algorithm of Figure 3.14 was used. The latter is based on the main assumption that the more constraining technological variable is the number of layers n_l . In fact, any additional layer entails the iteration of the fabrication steps used for the patterning of the conductor, thus making the total number of steps skyrocket. Moreover, the probability of failure increases as the number of layer increases, since all the layers have to be functional in order to ensure the overall performances of the coil. The algorithm goes as follows.

1. First, an evaluation domain is defined. This is done by selecting the conductor width w and the spacing between two adjacent turns s (the horizontal encumbrance e is defined as a consequence). The choice is dictated by the resolution achievable with a standard UV lithography process.
2. Starting from the evaluation domain, a series of FEM simulations, aiming to determine the flux linkage, are launched. In each simulation the number of turns n_s is increased until the complete filling of the available space is reached (n_s^{max}). Firstly, this procedure allows to determine the best choice for the outer radius r_{ext} . Most importantly, for $n_s = n_s^{max}$ the objective function (3.8) is maximized.
3. The number of layers n_l that are necessary in order to obtain the desired back EMF at the desired speed are calculated. Since the sector maximizes the flux linkage, the number of layers is the smallest possible for a given configuration. If the number is too high, the fabrication is considered too challenging and the solution is rejected.
4. If the number of layers is acceptable, a second control is performed. In particular, on the theoretical section that, given a certain conductor width, number of turns and layers, the coil should have, in order to have an overall resistance R_i equal or below $30 \text{ k}\Omega$ (*cf.* Table 3.3). If the required aspect ratio $\frac{t}{w}$ is not technologically feasible, the solution is rejected. If that is not case, a functional configuration has been found.
5. At this point, the secondary objective function (3.9) is evaluated. Since $j \neq 0$, the optimal number of turns is expected to be lower than n_s^{max} . The new configuration will thus maximize the electromagnetic torque, but will have a lower back EMF.
6. The number of layers n_l is evaluated once again. If it is higher than before, it means that the electromagnetic torque cannot be enhanced without complicating the fabrication, which entails the rejection of the new configuration. On the other hand, if n_l is the same, the configuration allows to fulfill the technical requirements while at the same time enhancing the electromagnetic torque without complicating the fabrication, and it is therefore accepted.

One should notice the calculation of the conductor section could in principle be performed after the maximization of the electromagnetic torque. As explained, configurations optimized in this sense have a reduced number of turns, which leads to lower resistances and more feasible aspect ratios. In practice however the difference is usually negligible, and unfeasible aspect ratios are likely to remain as such. This pushed to evaluate this aspect before in the algorithm, so that undesired configurations are immediately rejected.

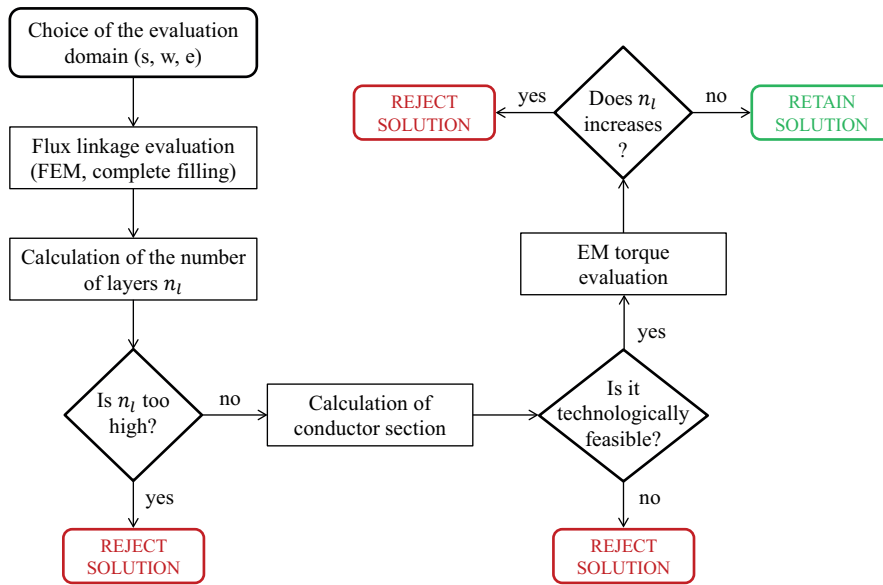


Figure 3.14 – Optimization routine.

3.3.6 Evaluation domain

As a general rule, coils with smaller encumbrance (and thus higher turn density) lead to a reduced number of layers but they will also present an increased technological hazard when it comes to the minimal conductor section. On the other hand, fulfilling the inner resistance requirement with larger turns is easier, but because of the limited number of turns per sector, the number of layers increases. These considerations drove the definition of the evaluation domain. In practice, it was verified that configurations with encumbrances below $4\ \mu\text{m}$ led to unfeasible aspect ratios (> 4), while encumbrances larger than $6\ \mu\text{m}$ required a challenging number of layers (> 6). To promote readability, such configurations will not be considered, and in the following the analysis will focus on the coils reported in Table 3.7. It should be noticed that for the evaluation of some functions (*e.g.* the aspect ratio) the horizontal encumbrance is not sufficient, and the conductor width as well as the spacing between turns must be defined explicitly. In principle, this would entail expanding the evaluation domain by testing different combinations of width and spacing for each given encumbrance. However, as will be discussed extensively in Chapter 4, the actual ratio $\frac{w}{s}$ is highly dependent on the fabrication process. For this reason, at this stage of optimization it was considered more effective to just set the spacing at $2\ \mu\text{m}$ and postpone finer tuning after having established the actual technological tolerances.

Table 3.7 – Evaluation domain

Coil ID	e (μm)	w (μm)	s (μm)
a	4	2	2
b	5	3	2
c	6	4	2

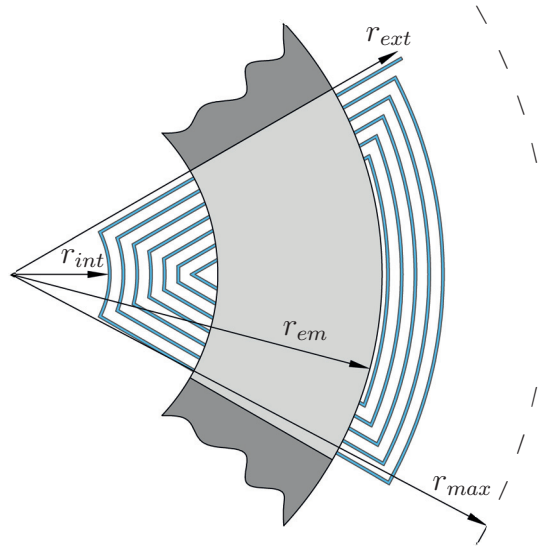


Figure 3.15 – Superposition of one magnet pole and a coil sector.

3.3.7 Inner and outer radius

Figure 3.15 shows the superposition of a magnetic pole, whose construction parameters are all known, and a coil sector, whose parameters need to be determined. A first problem concerns the choice of the inner and outer radius. For what concerns the inner radius r_{int} , it should be chosen as small as possible, as this condition allows to increase the number of turns that can be housed on the sector surface. It was therefore decided to put $r_{int} = r_{sh} + \epsilon$, where $\epsilon = 100 \mu\text{m}$ is a security tolerance to ensure proper assembly. On the other hand, the outer radius r_{ext} , cannot be determined *a priori*. It is safe to assume that it is pointless to put $r_{ext} < r_{em}$, as this will clearly not allow to exploit all the magnet surface for the coupling. In principle, increasing r_{ext} allows to house more turns, but since the magnet surface is limited, this effect will not continue indefinitely. In order to determine the right value, the outer radius was varied between $r_{em} = 2.3 \text{ mm}$ (which is the highest magnet radius allowed by size constraints) and the maximum allowed by the size constraints $r_{max} = 3.6 \text{ mm}$. For each value of r_{ext} , the maximum number of turns was calculated (complete surface filling) and the total flux linkage was obtained using FEM. The procedure was repeated for the three configurations of interest and the results are reported in Figure 3.16.

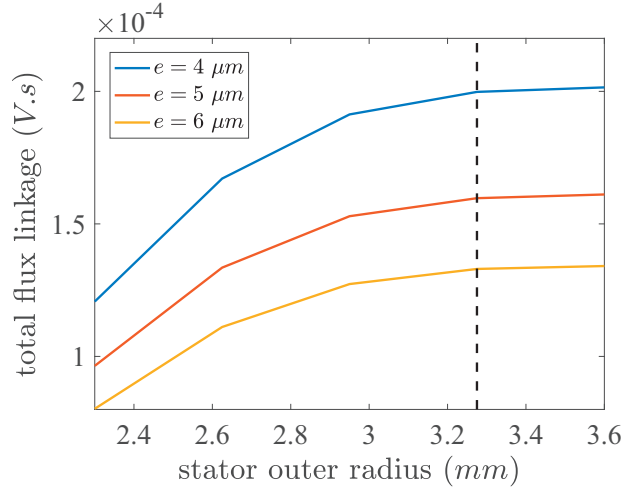


Figure 3.16 – Total flux linkage for different values of the stator outer radius.

As can be observed, the coupling is stronger for low encumbrance coils, which is hardly surprising considering that such configurations can house a higher number of turns. As the outer radius increases, the total flux linkage increases until a saturation is reached. Increasing r_{ext} further will only result in higher resistance due to the presence of additional turns which however do not contribute to the overall magnetic coupling. The saturation point is marked by the dotted line, which identifies $r_{ext} = 3.275$ mm.

3.3.8 Flux linkage and resistance

Once the outer radius was determined, additional simulations were run in order to obtain the flux linkage ψ_{sec} as a function of the number of turns for the three coils considered. As can be observed in Figure 3.17, where the turns are added from the outside to the inside, the flux linkage is not linear and the contribution of each additional turn becomes less and less significant. This is a direct consequence of the fact that the coils have a spiral shape, so that the active surface decreases from one turn to the next. Still, the function is monotonically increasing, so it is maximized by choosing $n_s = n_s^{max}$ (cf. paragraph 3.3.5).

Following the logic of Figure 3.14, the number of layers can be easily calculated using equation (3.13) and the required value of the phase constant reported in Table 3.3.

$$2p^2 n_l \psi_{sec}(n_s^{max}) \geq 0.0104 \text{ V.s} \rightarrow n_l \geq \frac{0.0104}{2p^2 \psi_{sec}(n_s^{max})} \quad (3.16)$$

Since the number of layer is a discrete number, the value computed by (3.16) must be

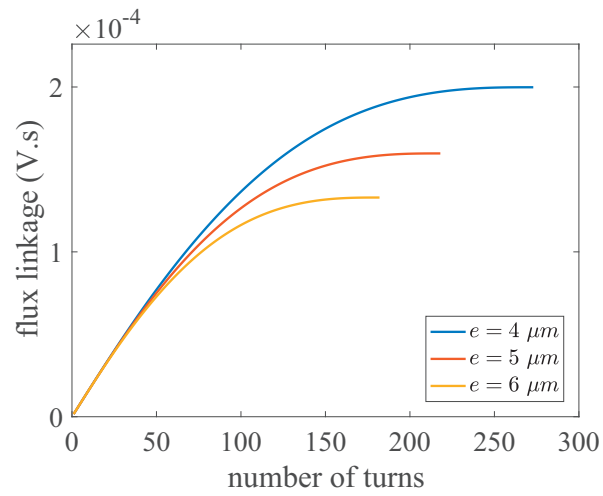


Figure 3.17 – Flux linkage (sector) as a function of the number of turns for the three coils configurations.

rounded to the next integer. This gives 3, 4 and 5 layers for the three configurations (Table 3.8). The 5 layers of the c solution seems relatively high, nevertheless at this stage c coils cannot be rejected, since the other two configurations might require challenging or even non feasible aspect ratio in order to comply with the resistance constraint. In order to evaluate this aspect, the total length of the conductor forming a sector l_{sec} is computed as a function of the turns number (Figure 3.18).

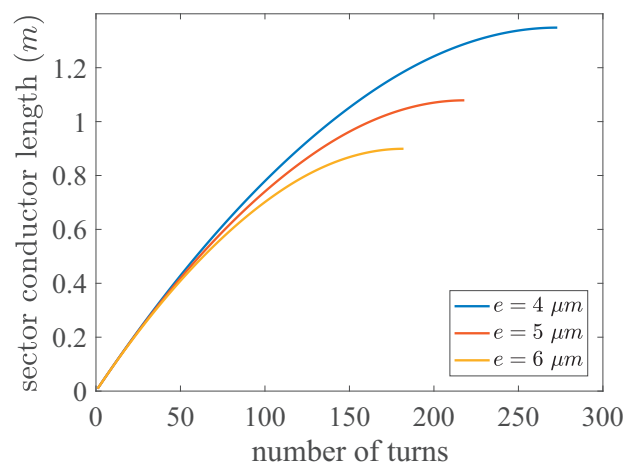


Figure 3.18 – Conductor length (sector) as a function of the number of turns for the three coils configurations.

Chapter 3. MEMS Generator for the regulation of a mechanical movement

The minimum aspect ratio can thus be easily calculated from equation (3.11):

$$R_i = \frac{\rho}{wt} 2p n_l l_{sec}(n_s^{max}) \leq 30 \text{ k}\Omega \rightarrow \frac{t}{w} \leq \frac{\rho 2p n_l l_{sec}(n_s^{max})}{30 \cdot 10^3 w^2} \quad (3.17)$$

Since the material is not known at this point, the aspect ratio was calculated using the bulk resistivities of copper and aluminum. Although these are not the only possible choices, they are very common materials for small scale applications, whose patterning methods are relatively assessed (more on this subject in Chapter 4). Table 3.8 reports the global results of the first steps of optimization. The conductor section is also reported, since for the reasons specified in paragraph 3.3.6 it might be useful to refer to these values rather than the aspect ratio itself.

Table 3.8 – Phase constant optimization

Coil ID	e (μm)	turns #	layers #	k_{ph} (V.s)	Aspect ratio Cu - Al	Section (μm^2)
a	4	273	3	0.0108	3.4 – 5.6	13.7 – 22.4
b	5	218	4	0.0115	1.6 – 2.6	14.4 – 23.4
c	6	182	5	0.0120	0.9 – 1.5	14.4 – 24.0

As expected, the configuration *a* is the most problematic. In particular, the solution involving aluminum for the fabrication should be rejected in compliance to the criteria defined above (Figure 3.14), and should be considered as border line even if copper is employed instead.

3.3.9 Electromagnetic torque

The final part of the routine provides to optimize the coils for boosting the electromagnetic torque (objective function (3.9)). This can be done easily starting from the flux linkage and the length of one sector obtained in the previous paragraph. Theoretically, the material resistivity and the section of the conductor should enter the calculation as well, but since such variables do not depend on the number of turns, they will scale the objective function, but not modify the global maxima. The electromagnetic torque as a function of the turns number is reported in Figure 3.19.

The function is not monotonically increasing, and a maximum can be found. Table 3.9 reports the optimal number of turns n_s^{opt} associated to such point as well as the updated number of layers, aspect ratio and section. For the three configurations considered, the number of layers has not changed with respect to the previous case (Table 3.8), so no configuration is rejected. As can be observed, since $n_s^{opt} < n_s^{max}$,

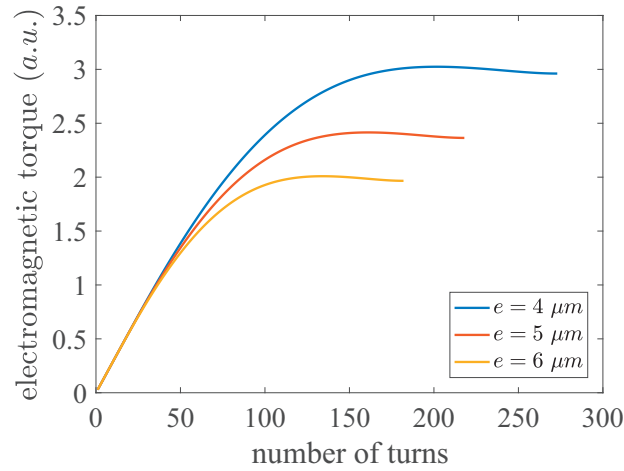


Figure 3.19 – Electromagnetic torque (sector) as a function of the number of turns for the three coils configurations.

the theoretical phase constant is slightly lower but still complies with the functional constraint of 0.0104 V.s. For the same reason, the resistance requirement can be fulfilled with smaller conductor sections. As anticipated in paragraph 3.3.5, such reduction is substantially negligible, especially considering that the actual section is going to differ from its nominal value due to the peculiarities of the fabrication method. Table 3.9 also provides for each solution the electromagnetic torque (*i.e.* the braking torque) in short circuit at the targeted speed of 33.5 rad.s^{-1} . The value was obtained by solving the dynamics equations (3.6), and assuming an inner resistance of $30 \text{ k}\Omega$.

Table 3.9 – Electromagnetic torque optimization

Coil ID	e (μm)	turns #	layers #	k_{ph} (V.s)	T_{em} ($\mu\text{N.m}$)	Aspect ratio Cu - Al	Section (μm^2)
a	4	199	3	0.0105	0.062	3.1 – 5.1	12.4 – 20.4
b	5	159	4	0.0111	0.069	1.5 – 2.4	13.3 – 21.7
c	6	132	5	0.0116	0.075	0.9 – 1.4	13.8 – 22.5

On the basis of the the aspect ratios reported in Table 3.9, a trend in terms of technological feasibility can be identified. For a preliminary qualitative analysis, a reasonable rule of thumb is to consider aspect ratios around 1 as feasible, challenging around 2, and unfeasible around 3. In this sense, the data show that if a copper based process is employed, the type *a* coil has a challenging fabrication, while the types *b* and *c* appear as less problematic. On the other hand, if an aluminum based process is chosen, *a* becomes substantially unfeasible, *b* challenging and *c* accessible. In this sense, since *c* requires the highest number of layers, such configuration becomes particularly interesting if an aluminum process has to be employed. At the present stage however,

these observations are conjectural and experimental data are necessary in order to complete the analysis. As for example, the actual dimensions are likely to vary with respect to their nominal values, thus modifying the aspect ratio. Harvesting such kind of information will be among the objectives of the next chapter.

3.4 Summary and conclusion

This chapter has addressed the design of a MEMS generator for an electronic escapement. Starting from the technical requirements, the reasons that led to the choice of an axial flux electromagnetic generator comprising two rotor yokes and a multipole ring shaped magnet were discussed.

The electromechanical model derived in Chapter 2 was then extensively used for assessing the most suitable configuration for the application and for simulating the working conditions. The study demonstrated the better suitability of a single-phase over a three-phase generator. The operating principle was clarified and two functional constraints that were not explicitly declared in the list of technical requirements were deduced. In particular, upper limits for the rotor moment of inertia and the stator resistance were specified.

A generic objective function, defined through priority coefficients, was defined and the associated domain was analyzed. The number of optimization variables was strongly reduced by eliminating those variables whose influence on the generator performance was known *a priori* as well as the variables that are restricted by technical contingencies. On the basis of these results, an optimization strategy capable of taking into account the technological hazard associated to the fabrication of the coils was conceived and used for the stator design. The primary objective was fulfilling the requirement on the output voltage magnitude while at the same time simplifying the fabrication process. Secondly, a finer optimization was launched in order to enhance the braking performances of the device.

The outcome of the study consisted in three coils configurations with different horizontal encumbrance. While all of the three are theoretically functional and feasible to some extent, additional information on the actual capabilities of the technology employed for the fabrication is needed in order to designate the most suitable solution.

4 Modeling and manufacturing of single layer planar coils

This chapter consists of a comprehensive study on single layer planar coils for low operational frequencies, from design to manufacturing. With respect to the previous treatise, the role of such components will be discussed from a more general perspective, going beyond their use for the MEMS generator. For this reason, the design strategy, based on both analytic formulas and FEM, will not aim to enhance the magnetic coupling with another element, but rather to boost the self inductive properties of the component itself.

After the design, two different manufacturing techniques, based on copper and aluminum respectively, will be presented and used for the coils fabrication and the key aspects as well as the technological limits of each process will be explored. The inductance measurements performed on the completed coils show good agreement with the theoretical predictions, typical discrepancy being below 4%. Finally, the overall performances of the components are evaluated in terms of surface and volumic inductance density and inductance to resistance ratio.

In the context of the MEMS generator development, the results of this study are significant at different levels. First, they give an experimental validation of the discussion on scaling laws in Chapter 2. Most important, they will allow to complete the analysis pursued in Chapter 3 and choose the better configuration on the basis on the actual capabilities of the technology employed for the fabrication (Chapter 5).

4.1 Applications of small scale inductors

In recent years, small scale inductors have become ubiquitous in multiple fields of technology. Other than MEMS electrical machines, these include wireless energy transfer, power conversion, energy harvesting, inductive sensing, biomedical applications as well as integrated circuits (IC) in general. Due to the reduced size of these components, usually in the millimeter or submillimeter range, the fabrication is normally pursued by making use of the ensemble of MEMS technologies. As a consequence, planar layouts are predominantly adopted, even though several fabrication methods aiming to obtain 3D-like structures have also been proposed [GL07, BKB⁺09]. The electromagnetic performances of microfabricated inductors however, are limited with respect to their macro counterparts, with lower quality factors [MdMHL99] and typical DC inductance of the order of hundreds of nH. Furthermore, achieving strong magnetic coupling with other elements (*e.g.* permanent magnets) is challenging as well. As discussed in Chapter 2, while some of these issues are directly associated with size reduction, there are also technological factors playing a role. Among the others, the absence of magnetic paths for the generated or coupled flux, and the limited number of conductor turns in each coil (typically less than 50). As a result, multiple improvement strategies were proposed throughout the years, involving different materials and geometries. For example, a commonly used technique is to increase the number of turns by fabricating multilayer coils [KSY⁺07, HJA08], while numerous authors demonstrated the implementation of magnetic materials [GSP⁺09]. In this context, a complementary approach that has yet to be fully explored, is to reduce the spacing between adjacent coil turns in order to enhance the interwinding magnetic coupling. Increasing the turns density is also particularly useful whenever the application requires a high number of turns to be implemented on a limited surface. In general, the sole drawback of reducing the spacing between the turns is the increasing of the interwinding capacitance, which however does not represent a fundamental issue in the majority of practical applications, since the capacitance is likely to be negligible with respect to other parasitic effects [YW00]. Nevertheless, obtaining smaller spacing usually entails smaller conductor sections, with heavy consequences on Joule heating and ohmic losses. In this pilot study, such technological challenge will be addressed. In particular, air core planar coils will be designed and fabricated following two different manufacturing approaches. The choice of this type of inductors, is motivated by the fact that planar geometries are the easiest to fabricate as MEMS, while the aforementioned alternatives (3D-like structures and coils with magnetic materials) require custom, less scalable processes. Also, the square geometry was chosen as it is easily modeled and it is also handled smoothly by layout generators software.

4.2 Design

4.2.1 Definition of the objective function

The optimization objective for a planar inductor may vary a lot, depending on the application and the contingent constraints. Typical objective functions may include the quality factor, the coil shape or the coupling with other magnetic entities (*cf.* Chapter 3). In this sense, the coils presented here, represent a simplified structure with respect to the previous chapter, considering that no other magnetic element is present. Moreover, under certain conditions that will be precised in the next paragraph, the system can be essentially reduced to an electric bipole, thus reducing the degrees of freedom to one. As long as the inductor can be described by lumped parameters (see paragraph 4.2.2) a generic objective function is identified by the writing

$$f_{obj} = \frac{L^i}{(\text{parasitic effects})^j} \quad (4.1)$$

where L is the coil inductance, intended as coincident with its "DC" value, the coefficients i and j are priority coefficients in the sense specified in paragraph 3.3.2 and the term "parasitic effects" is self explanatory. Table 4.1 points out some significant combinations for i and j .

Table 4.1 – Significant priority coefficients combinations

i	j	physical meaning
1	0	self inductance
1	1	quality factor

It was decided to maximize the self inductance ($i = 1$; $j = 0$), as this particular criterion leads to configurations that are closely related to the MEMS generator's stator from a technological perspective.

4.2.2 Lumped element models

Lumped parameters models offer significant advantages in terms of design with respect to distributed parameters structures. As a general rule, the use of lumped parameters is legit whenever the conductor length is much smaller than the signal wavelength [LC97]. As the size of the coil decreases, the aforementioned condition is likely to be satisfied, considering that the overall conductor length for micro inductors hardly exceeds the mm range, making them electrically short for operational frequencies up to some GHz. The coils that will be designed here, as well as the coils used for the

MEMS generator, represent a particularly unfavorable case from this point of view. In fact, due to the high turns density, total conductor lengths can reach the meters range (*cf.* Figure 3.18). Nevertheless, the long wavelength assumption still holds true for operational frequencies of tens of MHz. Furthermore, it is not uncommon for this class of components to be used for low frequencies applications, such as energy harvesters and sensors (see for example [JKK12, HMCM15]), as well as the extensively discussed MEMS electrical machines. For these reasons, equivalent circuits based on lumped parameters representing relevant parasitic effects were extensively studied and used [PKW⁺88, YRL⁺96]. In these models, the parasitic effects usually appear as resistors and capacitors, whose expressions are physically intuitive and can be often obtained analytically. On the other hand, the lumped inductance calculation is far from being straight forward. A possible approach, is to compute the inductance using FEM. This method however, presents the inconvenience of requiring significant computational resources. As a consequence, significant effort has been put throughout history in order to establish more flexible analytic models. We will briefly revise and compare the results obtained with both strategies.

4.2.3 Analytic formulas

The first ready-to-use formulas were proposed by Wheeler back in 1928 [Whe28]. Several years later, Grover [Gro46] published an authoritative compendium of formulas applicable to different geometries, including single layer planar coils. Starting from Grover expression for the self-inductance of a straight line conductor, Greenhouse [Gre74] has derived an accurate expression for the inductance of a rectangular planar coil which takes into account the negative mutual inductance between conductor segments carrying current in opposite directions. Finally, Mohan [MdmHBL99] has proposed three simplified expressions for single layer spiral coils, reported below, which can be easily adjusted to different shapes. These include square coils of the type schematized in Figure 4.1, which make the object of the present study.

$$L_{MW} = K_1 \mu_0 \frac{n_s^2 d_{avg}}{1 + K_2 \xi} \quad (4.2)$$

$$L_{CS} = \frac{\mu_0 n_s^2 d_{avg} c_1}{2} (\ln(c_2/\xi) + c_3 \xi + c_4 \xi^4) \quad (4.3)$$

$$L_{MF} = \mu_0 \zeta d_{out}^{\alpha_1} w^{\alpha_2} d_{avg}^{\alpha_3} n_s^{\alpha_4} s^{\alpha_5} \quad (4.4)$$

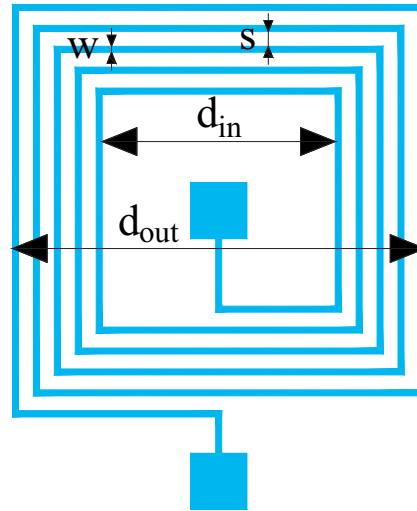


Figure 4.1 – Schematic of a square planar inductor (adapted from [MdmHBL99]).

In the formulas above, n_s is the number of turns, d_{avg} is the average diameter and ξ is the filling ratio of the coil. The last two parameters can be calculated from the outer and inner (generalized) diameters d_{out} and d_{in} (Figure 4.1) as

$$d_{avg} = \frac{1}{2}(d_{out} + d_{in}); \quad \xi = \frac{d_{out} - d_{in}}{d_{out} + d_{in}} \quad (4.5)$$

Finally, the coefficients $K_1, K_2, c_1, c_2, c_3, c_4, \zeta, \alpha_1, \alpha_2, \alpha_3, \alpha_4$ and α_5 depend on the coil shape.

Expression (4.2) is obtained by modifying the original Wheeler's formula, (4.3) is derived by approximating the sides of the coil as symmetrical current sheets with uniform current density and (4.4) is obtained by fitting a monomial form over a wide variety of inductors. While all the expressions were proven to be effective, a particular care should be put when they are used for design purposes. In fact, (4.2) originates from empirical observations [Whe28] and as a consequence the computed value might be influenced by the particular set of observations originally used to obtain the expression coefficients. At the same time, (4.4) is characterized by an even higher level of empiricism, since it is obtained using a pure regression technique. On the other hand, expression (4.3) is derived following a rigorous analytic approach, but it also incorporates a number of approximations (mainly concerning the geometry of the conductor) which inherently affect the accuracy of the final result. In order to deal with possible calculation errors, the inductance will be calculated using all of the three formulas, and the results will be compared to the dataset obtained using FEM. It should be noted that none of the formulas takes into account any effects activated at high frequency (*e.g.*

skin and proximity effects) that are known to have an impact on self-inductance (see for example [PXP11, DMLP13]). At the frequencies of interest however, the conductor section can be considered small enough to neglect these phenomena.

4.2.4 Influence of interwinding spacing

The analytic models discussed in the previous paragraph provide a basis for discussing the effect that interwinding spacing has on the overall coil inductance. A case of practical interest is when the inner and the outer diameter are constrained. In this situation, the average diameter d_{avg} and the filling ratio ξ appearing in equations (4.2), (4.3) and (4.4) are fixed parameters, and the spacing only affects the number of turns that can be housed on the coil surface:

$$n_s = \frac{1}{2} \frac{d_{out} - d_{in}}{s(1 + 1/\chi)} \quad (4.6)$$

where $\chi = s/w$ is the ratio between the spacing and the conductor width. Figure 4.2 shows the number of turns as a function of spacing according to (4.6) for different values of χ . The curves were obtained considering an outer diameter of 3 mm, an inner diameter of 300 μm and a spacing ranging from 1 to 5 μm . Such values were chosen in order to ensure consistency with the features of the coils presented in this work, nonetheless this choice doesn't entail a loss of generality. As can be observed, a reduced spacing always results in an increased turns number, the increase becoming less pronounced for larger conductor widths (lower χ). It is important to notice that, according to the presented analytic models, increasing the turns number has a boosting effect on the overall inductance, since the latter is proportional to n_s^κ with $\kappa > 1$. For coils of the size considered here, the enhancement is considerable even under relatively unfavorable conditions. For example, for $\chi = 0.1$ and a spacing reduction from 5 to 4 μm , the formulas predict an enhancement of the theoretical inductance between 49 and 56%. This motivates the interest towards fabrication processes that allow to reduce the interwinding distance.

4.2.5 Finite element simulations

From a finite element perspective, a three-dimensional magnetostatic problem has to be solved in order to evaluate the coils inductance. For this class of problems, scalar potential formulations are more efficient, in terms of computational effort, than vector potential formulations. This is due the drastical reduction of degrees of freedom to solve when using scalar formulations [SSCM98]. In particular, in order to allow current sources to be accurately represented, a reduced scalar potential is employed. The

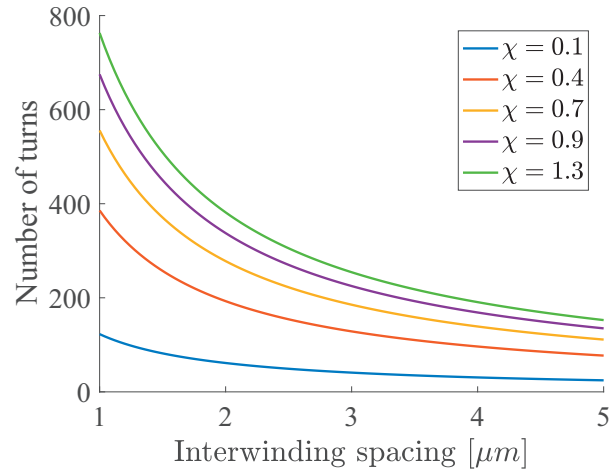


Figure 4.2 – Number of turns as a function of turns spacing for different χ values ($d_{out} = 3$ mm, $d_{in} = 300$ μ m).

magnetic field is decomposed into two components:

$$H = H_0 + H_m \quad (4.7)$$

with

$$H_m = -\nabla\phi \quad (4.8)$$

where H_0 is the magnetic field generated by current sources, H_m is the reduced magnetic field and ϕ represents the reduced scalar potential. The magnetic field H_0 complies with Ampère's law. Hence, the equation to solve using FEM is obtained by rewriting the divergence-free equations for the magnetic flux:

$$\nabla \cdot [\mu(H_0 - \nabla\phi)] = 0 \quad (4.9)$$

where μ is the magnetic permeability of the medium. In the absence of high magnetic permeability elements, this formulation leads to accurate results [BC07].

4.2.6 Evaluation domain

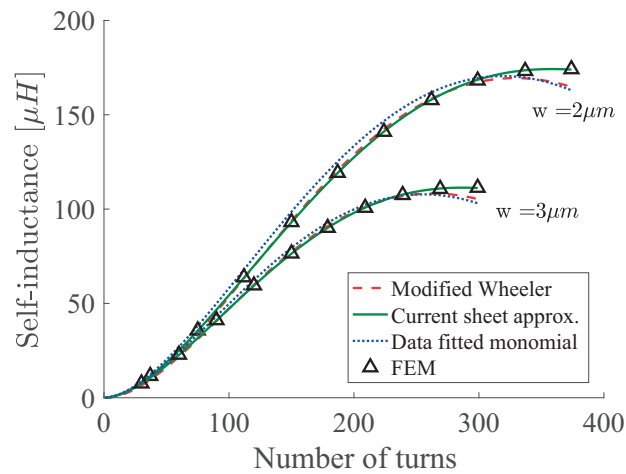
In order to explore the possibilities offered by the technologies employed for the fabrication, it was chosen to design and fabricate multiple coils configurations. All of them provide square shaped coils with a side length of 3 mm, however they differ when it comes to the conductor width and the interwinding spacing. In total, six types of coils were considered: 2 coils will be fabricated using a copper based process (from now on addressed as type A), while the remaining 4 configurations will make use of an aluminum based process (type B coils). The details of each configuration are listed in Table 4.2, where w is the width of the conductor and s is the spacing between two adjacent conductor lines. The nominal values were chosen by estimating the capabilities of each fabrication method by means of preliminary tests. Nevertheless, the actual fabrication results are expected to vary (see section 4.3 for further discussion on this topic). From an optimization perspective, the choice of keeping multiple configurations greatly simplifies the routine, in the sense that for each configuration the number of turns n_s is left as the only optimization variable. The conductor thickness was not taken into account since it normally has little influence on the overall inductance. Furthermore, as long as the current density inside the conductor can be considered as uniform (which happens to be the case at low frequencies of operation), it can be assumed that the device will perform better as the conductive layer becomes thicker. Achieving such goal is therefore left among the objectives of the fabrication process rather than the design itself. One should notice that the same consideration applies to the stator coils for the MEMS generator (*cf.* paragraph 3.3.6).

Table 4.2 – Coils configurations features

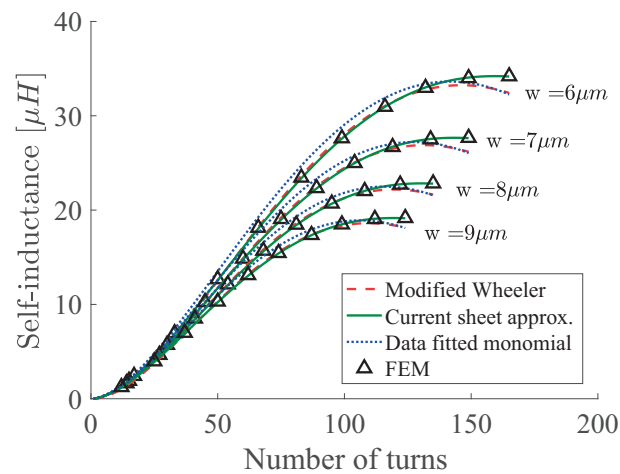
s (μm)	w (μm)	fabrication process
2	2	type A (Cu)
2	3	type A (Cu)
3	6	type B (Al)
3	7	type B (Al)
3	8	type B (Al)
3	9	type B (Al)

4.2.7 Results and comparison

Figure 4.3 shows the self-inductance as a number of turns, for the type A and type B coils, computed using the three simplified formulas by Mohan and FEM. The turns are increased proceeding from the outside to the inside of the coil, so that the lower the turns number, the hollower the coil is, while the highest number of turns corresponds to the complete filling of the surface.



(a)



(b)

Figure 4.3 – Self-inductance as a function of turns number according to the three analytic formulas and FEM: (a) type A coils, (b) type B coils.

As can be observed, at the beginning the self-inductance tends to increase almost linearly as the number of turns increases. However, since the area of each additional loop decreases, the contribution to the overall inductance becomes less and less significant. Eventually, a saturation is reached, at which point adding any more turns will basically just increase the resistance and complicate the fabrication. This behavior is associated to the spiral arrangement of the coils, and is similar to what was found in paragraph 3.3.8 for the flux linkage and the resistance. It is worth noticing that the modified Wheeler (4.2) and the monomial fit (4.4) formulas compute a decrease of the inductance when the last inner turns are added. From a physical viewpoint, this is misrepresentative of the coil behavior, and is likely to be considered as a glitch

Chapter 4. Modeling and manufacturing of single layer planar coils

generated by the interpolation technique used to obtain the formulas. This is also proved by FEM data as well. Figure 4.4 shows the relative error between the analytic calculations and the values obtained via FEM for a type A coil with both the spacing and conductor width equal to $2\ \mu\text{m}$. For the three formulas the relative error is more significant for low numbers of turns, and tends to decrease as the number of turns increases. For formulas (4.2) and (4.4) the error increases again at the end for the aforementioned reason. On the other hand, the formula based on current sheet approximation is highly coherent with the FEM data, with a maximum deviation of 1.2% for the considered case. The trend is however common to all coils configurations. Since the inductance function increases monotonically, the goal of maximizing the self-inductance is in principle reached by designing the coils with as many windings as possible. However, in order to keep the results comparable, the number of turns was chosen so that the faulty result produced by (4.2) and (4.4), is basically cut out. This was done by simply choosing the number of turns that corresponds the pseudo maximum inductance in (4.2). As a result, the complete filling of the surface is avoided. This has a negligible impact on the components performances (below 1%) and at the same time allows the fabrication of an inner pad (Figure 4.1) with a surface large enough to ensure a simple electrical connection with the outer world (*e.g.* by wire bonding). The characteristics of the optimized coils in terms of number of turns and predicted inductance are reported in Table 4.3. As will be discussed, due to the peculiarities of each fabrication method, the actual dimensions are expected to vary with respect to the nominal values.

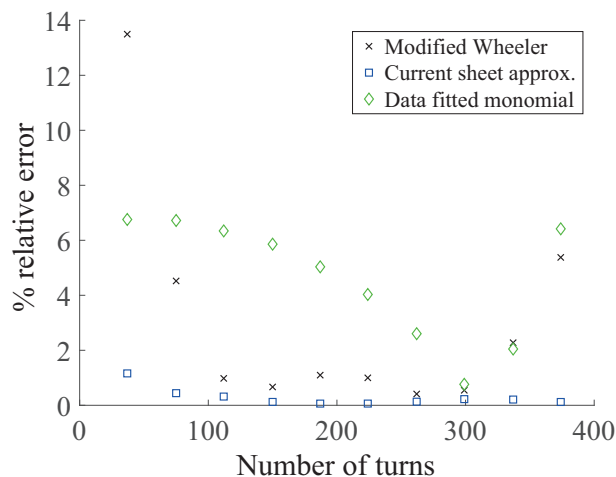


Figure 4.4 – Relative error between FEM data and analytic formulas for a type A coil with conductor width and spacing equal to $2\ \mu\text{m}$.

Table 4.3 – Optimal number of turns

s (μm)	w (μm)	Opt n_s #	L_{MW} (μH)	L_{CS} (μH)	L_{MF} (μH)	L_{FEM} (μH)
2	2	329	169.4	172.9	170.3	172.6
2	3	263	108.3	110.5	107.7	110.3
3	6	146	33.2	33.9	33.6	33.9
3	7	131	26.9	27.4	27.2	27.4
3	8	119	22.2	22.6	22.5	22.6
3	9	109	18.6	19.0	18.9	19.0

4.3 Fabrication

4.3.1 Aluminum vs Copper

At the end of the 1990s significant technological effort was spent in order to replace aluminum with copper in IC interconnects. This was motivated by the fact that for IC circuits with high level of integration, the total resistance of the connecting lines have a non-negligible impact on the performances of the device [BAZG14]. In this sense, copper has a lower bulk resistivity than aluminum. This leads to increased electrical performances and serves well the purpose of scaling, as the conductors sections can be smaller with respect to the aluminum counterparts while still limiting Joule heating and ohmic losses. Furthermore, copper offers in general better results in terms of reliability, due to the higher thermal conductivity and resistance to electromigration. While the use of copper is basically mandatory in modern ULSI devices, where the conductor width is of the order of tens of nm, for devices with larger metallic tracks aluminum should still be considered as a decent alternative. The reason is that despite its superior performances, copper processing is more demanding from a technological point of view. In fact, while aluminum is normally deposited and patterned by conventional dry etching techniques (typically chlorine based plasmas), the same top down approach cannot be applied to copper as easily, mainly due to the low volatility of the copper compounds formed during the process. Although several developments in this sense are reported in literature (see for example [JKHS95, LPC⁺98, KL00]), a reliable dry etching technique for copper as yet to be established, and patterning is normally pursued by mean of additive techniques like selective chemical vapor deposition or damascene processes. Furthermore, copper atoms tend to diffuse with relative ease in adjacent materials, so that a diffusion barrier is normally required. Using aluminum might therefore be a cheapest and equally effective alternative depending on the application. Both domains were thus investigated by optimizing two different process flows. Next paragraphs will give detailed insights on the fabrication methods, while the actual morphological and electrical characterizations will be presented all at once in order to facilitate the comparison.

4.3.2 Copper based process

Figure 4.5 shows a schematic cross section of the process flow, which can be considered to be a variation of the Damascene process, first established by IBM in the late 90s [Mad02]. It's an additive technique, consisting in etching trenches into a dielectric layer, filling the trenches with copper and then removing the copper from the untrenched area through a step of chemical mechanical polishing (CMP). While the basic principle stayed the same, multiple combinations in terms of materials (silicon, dioxides, polymers) and deposition techniques (electroplating, electroless deposition) were studied throughout the years. Here Polyimide (PI) was chosen as the mold material due to its low- κ properties and its low internal stress, the latter being especially important due to the targeted high density of copper lines. Using a similar method, Pisani [PHB⁺05] has demonstrated the fabrication of 5 μm thick square coils with a track width between 10 and 40 μm , and interwinding spacing between 5 and 20 μm . More recently, Matsumura [MET⁺10] has adopted imprint lithography in order to obtain a denser pattern, consisting of 5.6 μm thick copper lines with a spacing of 3.9 μm and a width of 5.5 μm . The targeted pattern for the type A coils is even more dense (*cf.* Table 4.2), so the process was optimized in order to address such challenging task. Also, a novel approach based on Ion Beam Etching (IBE) for the cleaning of the coil surface after the CMP step was adopted. The fabrication steps are discussed in detail below, making reference to Figure 4.5.

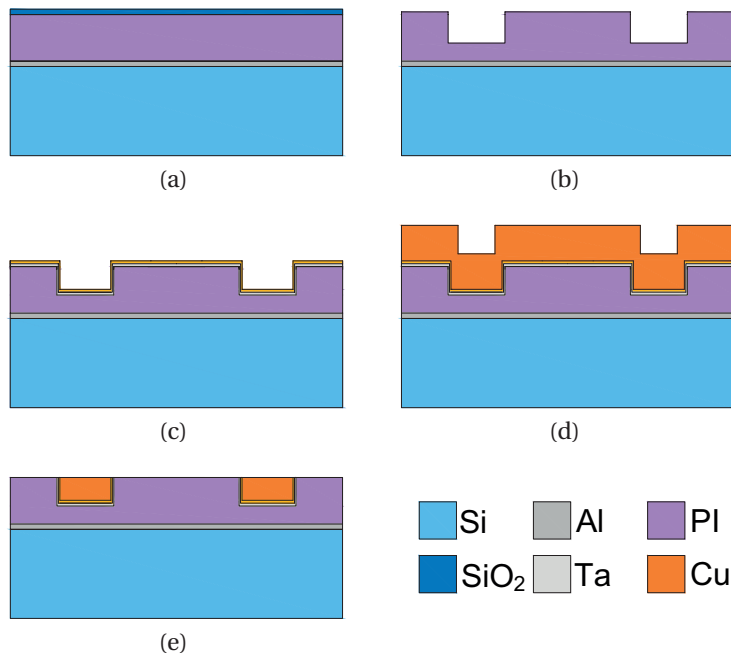


Figure 4.5 – Schematic of the Cu process flow: (a) 150 nm Al + 10 μm PI + 200 nm SiO₂ deposition on Si substrate, (b) PI mold structuration, (c) 40 nm Ta + 350 nm Cu deposition, (d) Cu electroplating, (e) CMP + IBE cleaning.

Step (a)

The first step consists in the deposition of a 150 nm aluminum layer on a blank silicon wafer using a Physical Vapor Deposition (PVD) technique. In particular sputtering was chosen due to its relatively high deposition rate (up to $1.2 \text{ nm}\cdot\text{s}^{-1}$). The function of this layer is enhancing the adhesion between the PI and the underlying silicon substrate, so there are no particular requirements in terms of purity. It should be noticed that using a conductive material for the adhesion layer is likely to generate a parasitic capacitance with the coils (Figure 4.5(e)). As a consequence, dielectric materials are a wiser choice whenever the application provides high operational frequencies. The author obtained equally good results in terms of adhesion using a 200 nm layer of SiO_2 obtained via thermal oxidation. After the deposition of the adhesion layer, liquid Polyimide (PI 2611 by HD Microsystems) is spun on the wafer surface and cured at $300 \text{ }^\circ\text{C}$ in a N_2 environment, the targeted thickness being equal to $10 \text{ }\mu\text{m}$. Subsequently, a 200 nm layer of SiO_2 is sputtered on the PI with the purpose of serving as a hard mask for PI etching. The use of a hard mask is motivated by the fact that the oxygen based plasma used for PI etching is very selective ($> 20 : 1$) with respect to SiO_2 . This allows to use sub-micrometer thick resist during the lithography process, with consequent benefits in terms of achievable resolution.

Step (b)

After the patterning a 550 nm thick positive tone photoresist, the SiO_2 hard mask is structured by mean of a CF_4 plasma. Subsequently, an oxygen plasma recipe is used for the PI etching. Such technique is highly anisotropic and allows to etch relatively deep trenches with almost vertical walls without compromising the isolation in between, which is a key point in order to obtain a high turn density. The etch depth however requires significant effort to be optimized. In fact, a deeper etch depth will result in a larger section of the conductor, leading to better electric performances in terms of ohmic losses and Joule heating. On the other hand, the etching technique is far from being 100% anisotropic and the PI walls between the trenches are also affected by the process. While a thinning of such structures with respect to their nominal value is desired, as it leads to a larger conductor section, an excessive etch depth might compromise mechanical stability or even cause complete degradation of the material. The effect can be visualized in Figure 4.6, which shows properly processed trenches (left), trenches mechanically deformed due to excessive thinning of the insulation material (right) and complete the material deterioration (down). For the given nominal insulation of $2 \text{ }\mu\text{m}$ it was found an optimal etch depth around $5 \text{ }\mu\text{m}$.

Once the PI etch is complete, another CF_4 plasma is used for the removal of the SiO_2 hard mask. Such step is particularly important and skipping it may cause problems at different levels. In particular:

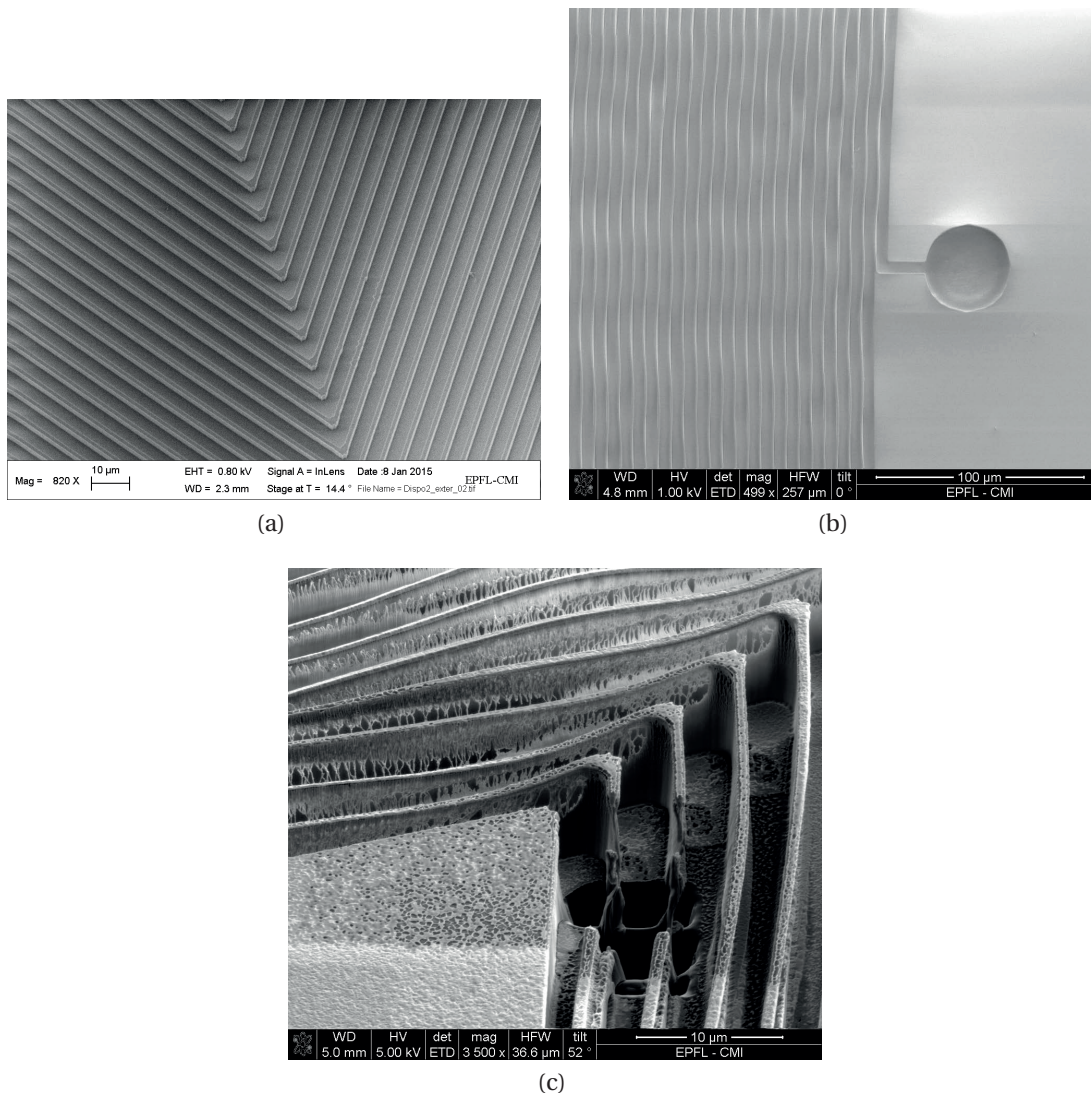


Figure 4.6 – PI etching: (a) properly etched trenches, (b) deformed trenches due to overetch, (c) complete deterioration of the insulating material.

- Since SiO_2 is very resistant to the O_2 plasma, a capping structure is likely to be formed during PI etching (Figure 4.7). Such structure has a shadowing effect which hampers a uniform deposition of the following materials.
- The adhesion between SiO_2 and the seed layer that follows is poorer with respect to PI. Hence, keeping the SiO_2 hard mask may cause delamination issues during CMP.
- Any residual SiO_2 will end up in being removed during the CMP, resulting in stray hard particles that are likely to scratch the much softer copper surface.

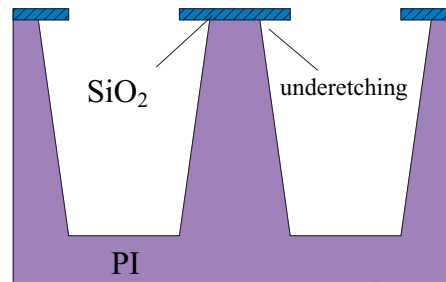


Figure 4.7 – Shadowing effect of the SiO₂ cap.

Steps (c)-(d)

Once the PI mold is complete, the process flow provides to fill the trenches with copper. For this purpose, electroplating technique was chosen. The fundamentals of the method have been known for decades (see for example [Sch14]) and nowadays the technique is employed in many industrial environments for multiple applications. At MEMS scale, it combines good trench filling properties with the possibility to deposit thick layers with relative ease. However, electroplating can only be applied to conductive substrates, and since PI is a dielectric material, the preliminary deposition of a conductive seed layer is necessary in order to accomplish the step. A two metals seed layer was used, consisting of 40 nm of tantalum followed by 350 nm of copper, both deposited by sputtering. While the copper function is to promote electroplating, the tantalum prevents the diffusion of copper into the PI mold and enhance the adhesion to the substrate [SC01]. Equally good results were obtained using 40 nm of titanium followed by 250 nm of copper deposited by evaporation [OF86, OF88]. To further enhance adhesion to PI, a relatively mild O₂ plasma treatment is performed prior to seed layer deposition in order to clean and functionalize the substrate. Another key point is to obtain good step coverage, as any interruption in the conductive layer will result in filling defects, for which an example can be observed in Figure 4.8. To improve the quality of step coverage, the substrate is put in relative motion with respect to the target material during the PVD deposition, whether is sputtering or evaporation. Figure 4.9 shows an optical profiler measurement performed right after the seed layer deposition on a type A coil. Measured etch depth is equal to 4.75 μm. The trench filling via electroplating is normally performed immediately after the seed layer deposition in order to prevent the oxidation of the surface, which might result in a poor quality of the electroplated copper as well as adhesion issues.

Step (f)

After the electroplating, the copper in excess is removed with a CMP step. The technique is based on the use of both mechanical abrasion and chemical etching. The wafer is fixed on a rotating support, and pressed against a rotating abrasive pad (Figure

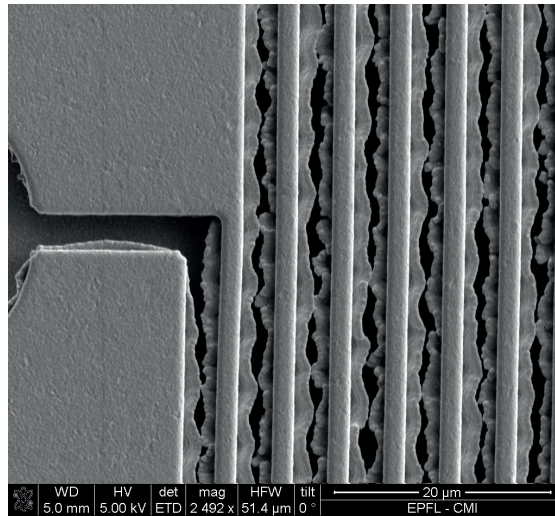


Figure 4.8 – Incomplete filling of the PI after electroplating, caused by poor seed layer step coverage.

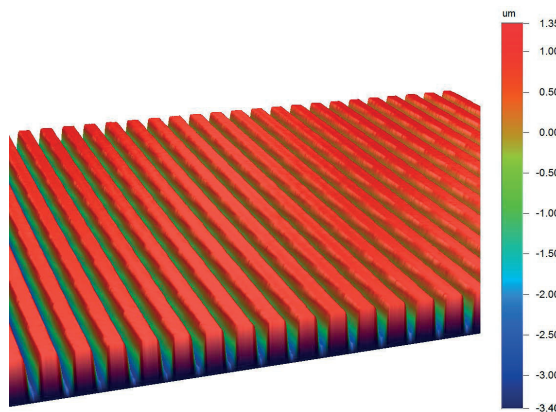


Figure 4.9 – Optical profiler measurement performed on a B type coil after the seed layer deposition.

4.10). The process is assisted by the injection of a slurry, *i.e.* a suspension of abrasive particles in a solution of chemical agents that attack the surface to be polished [Rob04]. In the present case, silica particles with an average diameter of 100 nm in a sulfuric environment was used.

During the process a wide variety of defects may be induced on the wafer, including contamination issues, scratches [PKVC12], slurry residues as well as design dependent defects like dishing and erosion. Among the others, the absorption of the sub-micron slurry particles on the copper surface was found to be a major issue, as the non conductive nature of such particles compromises the contact resistance of the coils. Post-CMP cleaning is normally based on brush scrubbing [Wol90], and a number of efforts were made in order to increase the efficiency of the process, focusing both

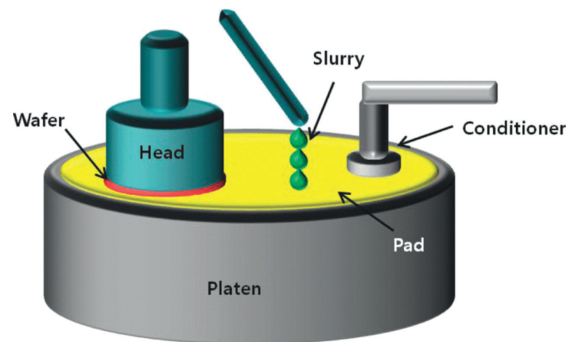


Figure 4.10 – Operating principle of CMP (from [JKKCKH⁺12]).

on the modeling [BLM⁺02] and the chemicals involved [RAS⁺95, MBC⁺15]. Here, a completely different approach based on IBE was chosen. The technique is based on the generation of a broad band of Argon ions from an Inductive Coupled Plasma (ICP) source. The ions are then accelerated and directed towards the substrate, where the material is etched by purely mechanical scattering. With respect to the brush scrubbing, the IBE cleaning offers several advantages. First of all, assumed that the ion beam etcher is provided, the process doesn't require a dedicated setup. Also, since no chemicals are involved, the etching being purely physical, the optimization of the procedure is relatively simple. At the same time issues related to the compatibility of the materials are drastically reduced. Finally, a dry technique is particularly useful when working with copper, since the latter tends to get oxidized easily in moist environments. However, a major drawback is that the ion beam has no selectivity with respect to the silica particles, so that the PI/copper structures are also affected by the process. An attentive control of the cleaning parameters, especially the beam energy and the duration of the process is thus needed in order to preserve the coil functionality. For the same reason the method is not suitable whenever the application requires a high smoothness of the surface, since the etched silica particles tend to leave footprints on the underlying copper. Figure 4.11 shows a detail of a completed coil before and after the IBE cleaning, while an aerial view of a finished coil can be observed in Figure 4.12.

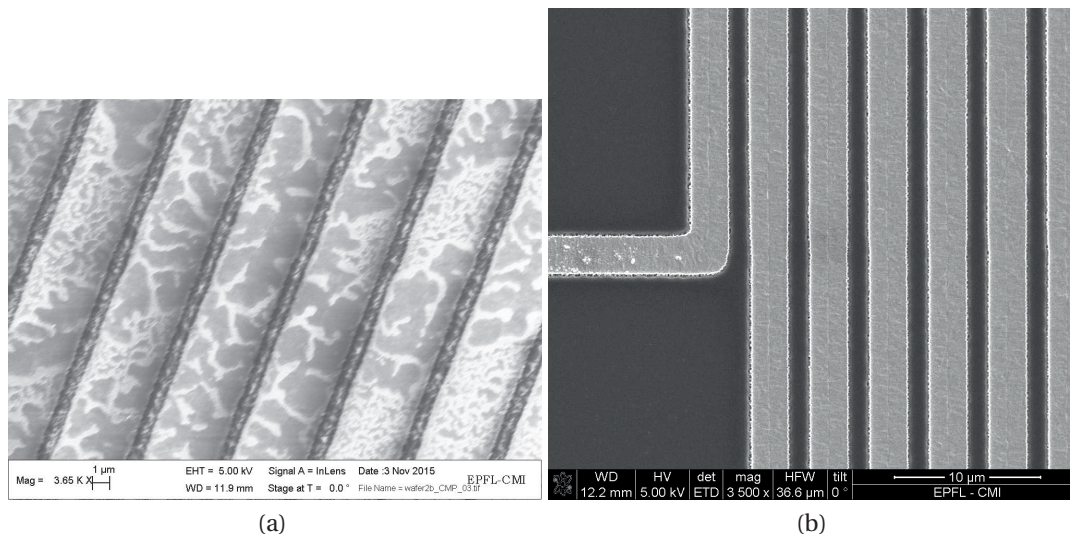


Figure 4.11 – Detail of a coil surface (a) before and (b) after IBE cleaning.

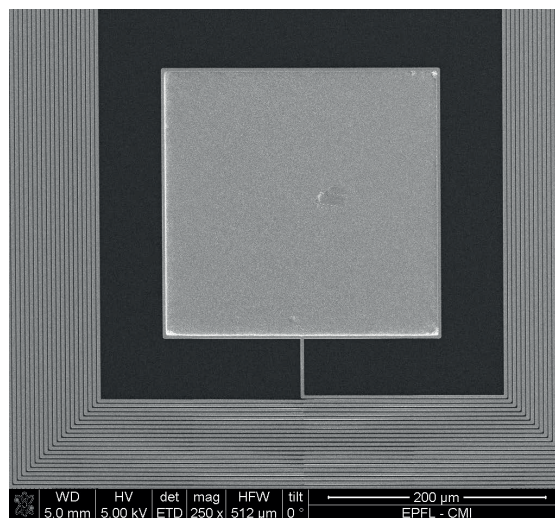


Figure 4.12 – Aerial view of a finished copper coil.

4.3.3 Aluminum process

The second proposed process is based on aluminum and its basic steps are presented in Figure 4.13. As can be observed the, principle follows a top down logic, exploiting the fact that Al can be patterned directly. A similar approach was demonstrated by Carazzetti [Car06] for the fabrication of planar inductors for RF applications. The smallest spacing obtained in his work is equal to 4 μm for 20 μm wide lines with a thickness of 3 μm . Coils comprising thicker conductor lines of 8 μm were also presented by the same author, however the spacing was also increased to 8 μm . The process used here can be considered as an evolution in this sense, since it was optimized in order

to allow the fabrication of four configurations of square coils (type B) with a targeted spacing of $3\ \mu\text{m}$ and a thickness of $8\ \mu\text{m}$. The nominal turn width ranges from 6 to $9\ \mu\text{m}$ (*cf.* Table 4.2). The fabrication steps are discussed in detail below, making reference to Figure 4.13.

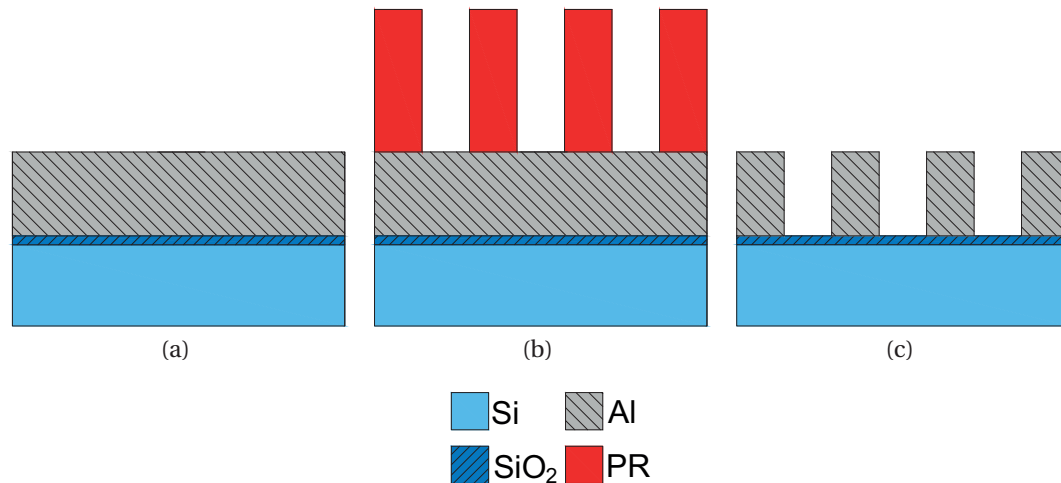


Figure 4.13 – Schematic of the Al process flow: (a) Sputtering of $8\ \mu\text{m}$ Al, (b) lithography on $10\ \mu\text{m}$ thick resist AZ9260, (c) deep ICP etching and resist stripping.

Step (a)

The starting substrate is a Si/SiO₂ wafer, on which a $8\ \mu\text{m}$ layer of Al is deposited. Unlike the copper process, in which the etch depth (and thus, the conductor section) was determined through process optimization, the targeted conductor thickness can be decided relatively freely (to some extents). In this sense, the value of $8\ \mu\text{m}$ was chosen by taking into account the resistivity difference between aluminum and copper and aiming to obtain comparable resistances per length unit. While in principle any PVD technique can be used, the choice was mainly dictated by practical constraints. In particular, the large thickness of the layer motivated the use of a sputtering machine in which aluminum is deposited at the high rate of $8\ \text{nm}\cdot\text{s}^{-1}$, even though the material resistivity was expected to be relatively poor.

Step (b)

The next step consists in the deposition of a $10\ \mu\text{m}$ thick positive tone photoresist layer (AZ2960), followed by patterning via direct exposition with a $405\ \text{nm}$ laser diode. The reason why the photoresist layer is thicker than the aluminum itself is that the Cl_2/BCl_3 plasma used for the Al patterning attacks the two materials at the same rate, so the

Chapter 4. Modeling and manufacturing of single layer planar coils

photoresist in excess guarantees that the Al layer is not directly exposed to the plasma. This is particularly important in the final stage of the process, as plasma exposure is extended in order to guarantee the proper clearing of aluminum from unwanted areas.

Step (c)

Finally, a Cl_2/BCl_3 based plasma is used for the patterning of the Al layer and the residual photoresist is subsequently removed in a wet environment using a commercially available remover. It is crucial for this operation to be performed immediately after the etching step, since chlorine byproducts that are still present on the wafer (especially in between the coil turns) are likely to react with air forming HCl, thus causing dramatic corrosion of the patterned aluminum. One main issue associated with the etching technique is its inherent non uniformity with respect to the layout that is being patterned. In fact, the Cl_2/BCl_3 tends to attack at higher rates areas with less exposed aluminum. The effects are shown in Figure 4.14(a). As can be observed, for the same etching time peripheral turns are far more affected than packed structures, which ultimately leads to mechanical failure. An approach that was proficiently adopted to deal with this problem is to use filler structures (Figure 4.14(b)) in order guarantee uniform etching rate on the wafer surface. It should be noted however that these additional metallic structures might become the siege of parasitic eddy currents at higher operational frequencies, so their removal should be envisioned for such applications. An aerial view of a finished coil can be observed in Figure 4.15.

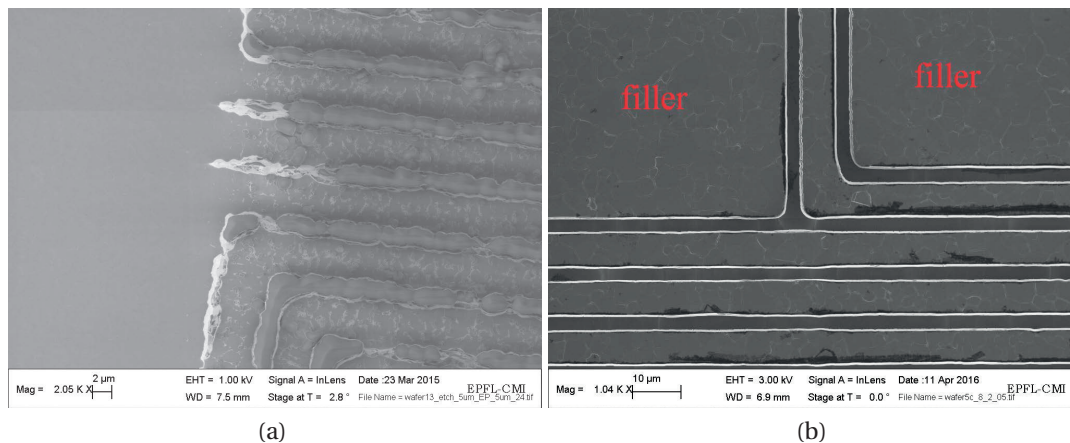


Figure 4.14 – Peripheral turns after Al etching: (a) without filler and (b) with filler.

4.3.4 Key aspects and comparison

The most blatant difference between the two processes is the number of process steps. From this point of view, the copper based process is far more complex, providing

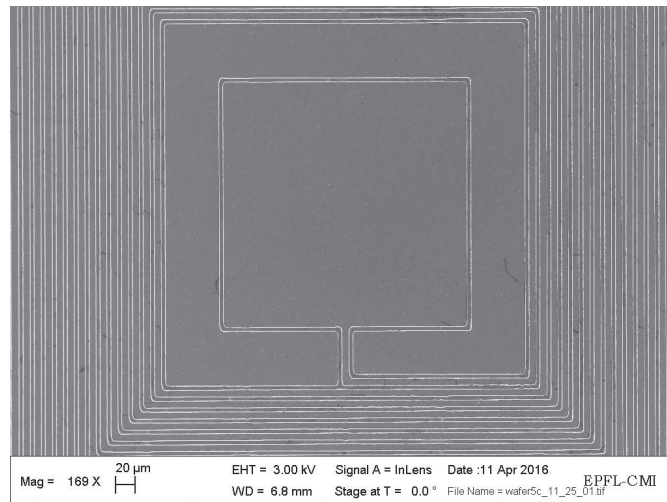


Figure 4.15 – Aerial view of a finished aluminum coil.

a higher number of steps, many of which (like the seed layer deposition and the CMP) require a strict control of the process parameters in order to be performed correctly. On the other hand, achieving a high resolution with the aluminum process becomes more challenging, due to the higher thickness of the photoresist layer used for photolithography (550 nm vs 10 μm). For both processes a driving key point is the degree of anisotropy that characterizes the etching techniques employed and which affects both the masking and the underlying material. In the ideal case, the material is not attacked in directions other than the main etching direction, meaning that the material can be etched at virtually any depth with perfectly straight side walls. In practice this is hardly the case, and etching along the main direction is always accompanied by (usually unwanted) lateral overetch, which can easily reach the 20 – 30% of the etch depth depending on the material, the thickness and the environmental conditions. In the proposed copper process, the material to be etched is PI. This means that lateral overetch entails a thinning of the insulation between the copper lines. While an excessive lateral overetch may compromise the mechanical and electrical stability of the insulation (*cf.* Figure 4.6) the phenomenon may also be controlled in order to increase the conductor section and the turns density. In the aluminum process on the other hand, the conductor material itself is attacked. This basically means that any etch on the sidewalls is unwanted, as it leads to smaller sections and sparser turns (see Fig. 4.16). An effective strategy that was extensively used for the management of overetch is to compensate for it at a lithographic level, by exposing narrower photoresist lines (assuming a positive PR tone). It is worth noticing that such technique cannot be used indefinitely and its applicability is limited, among other factors, by the lithographic setup (especially the radiation source).

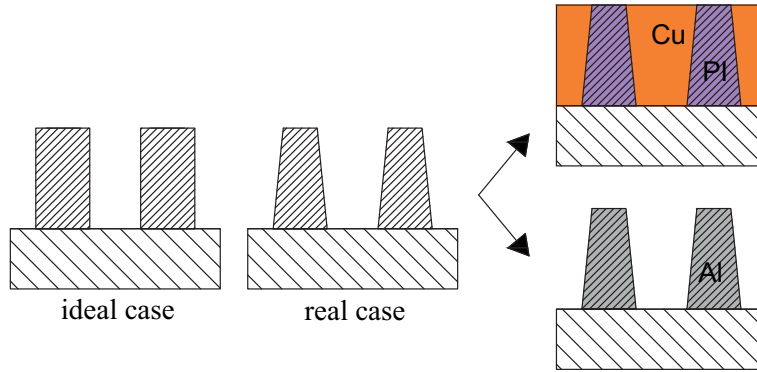


Figure 4.16 – Effect of etching anisotropy on the two process flows.

4.4 Characterizations and Measurements

4.4.1 Fabrication results

For the purpose of characterizing morphologically the coils fabricated with the Cu/PI process, a destructive analysis was performed using a Focused Ion Beam (FIB). Figure 4.17 shows the cross sections obtained from both types of coils fabricated with this method. As can be observed, the PI trenches are perfectly filled with copper. Nevertheless, a minor difference between the conductor and the insulator heights can be observed. This is due to the combined effect of the dishing occurred during the CMP and the IBE cleaning. Measurements showed however that the difference is below 220 nm and is therefore negligible with respect to the total thickness of the conductor. The coil with the nominal turn width of 2 μm has a thickness of about 4 μm , while the coil with the 3 μm lines has a thickness of 4.5 μm . The difference is given by the fact that the O₂ plasma used for the PI mold structuring tends to etch larger unmasked areas at higher rates. This is true for the lateral overetch as well, which is less pronounced for the coil with nominal 2 μm lines. The resulting turns densities are equal to 0.25 *lines*/ μm and 0.20 *lines*/ μm , while the aspect ratios of the conductors are equal to 1.69 and 1.13. Table 4.4 recaps these results.

Table 4.4 – Fabrication results for Cu/PI coils

s_{theo} (μm)	s_{meas} (μm)	w_{theo} (μm)	w_{meas} (μm)	Section (μm^2)	Density (<i>lines</i> / μm)	Aspect ratio
2.0	1.3	2.0	2.7	10.8	0.25	1.69
2.0	1.0	3.0	4.0	18.2	0.20	1.13

For what concerns the aluminum process, the FIB could not be used as a characterization tool. The main reason is that due to the free space between the lines, the cross-section results severely deformed after the ion etching, thus making any measurement impossible. The conductor thickness was instead measured using an optical

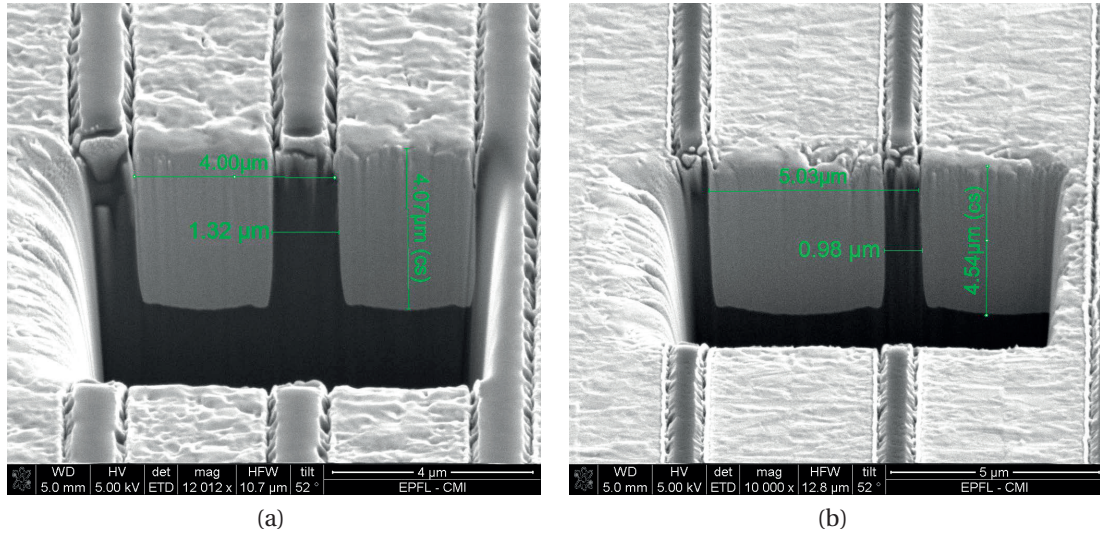


Figure 4.17 – FIB cross sections of completed copper coils with nominal lines widths equal to 2 μm (a) and 3 μm (b).

profilometer (Fig. 4.18a). The measured thickness is common to all coils and is equal to 7.7 μm . A coincident value was obtained using an image measurement tool on a tilted sample (Figure 4.18b). This result is unsurprisingly coherent with the targeted thickness of 8 μm for the sputtered Al layer. As can be observed from both Figure 4.18b and Figure 4.19, the effect of the lateral overetch on the conductor sidewalls is much more pronounced with respect to the previous case. A rough estimation of the actual section of the conductor can be obtained by assuming a trapezoidal shape and measuring the line width at the top and the bottom (Fig. 4.19). The same approximation allows to compute an average aspect ratio, which ranges from 1.48 to 0.95 as the nominal width of the lines increases. Finally, turns density ranges from 0.11 to 0.08 *lines*/ μm . These results are summarized in Table 4.5.

Table 4.5 – Fabrication results for Al coils

s_{theo} (μm)	w_{theo} (μm)	Section (μm^2)	Density <i>lines</i> / μm	Aspect ratio
3	6	43.33	0.11	1.48
3	7	44.66	0.10	1.41
3	8	49.36	0.09	1.22
3	9	61.50	0.08	0.95

Morphological characterizations offer a basis for discussing the performances of each process, in particular for what concerns the anisotropy of the etching technique (*cf.* Figure 4.16). As can be grasped from Figure 4.17, PI insulating structures etched throughout the copper process have nearly vertical walls with a slope of about 1 – 2°. In

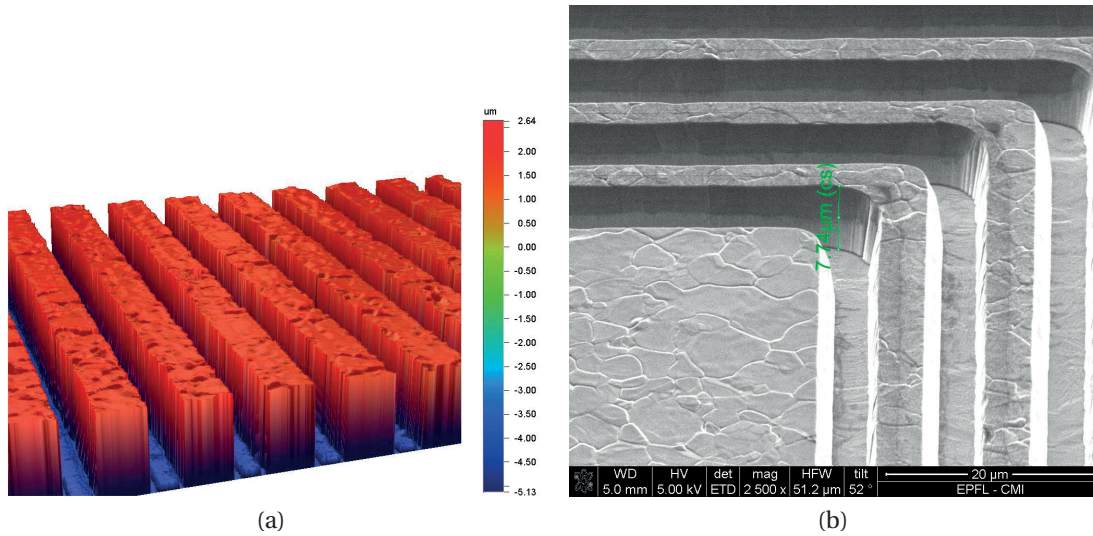


Figure 4.18 – Thickness measurement on a completed type B coil with nominal lines width equal to 7 μm lines: (a) 3D optical profilometry and (b) SEM measurement,

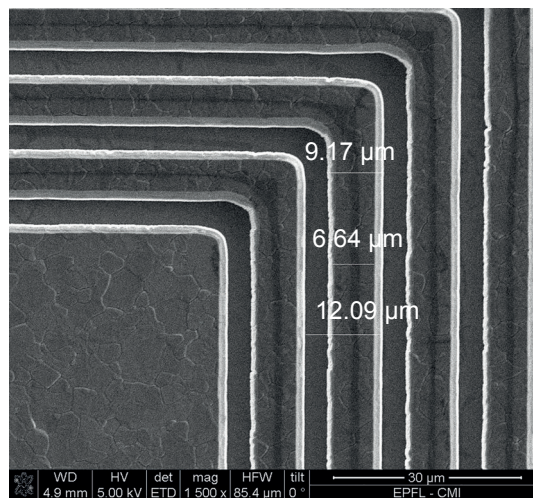


Figure 4.19 – Detail of a completed type B coil with nominal lines width equal to 9 μm.

this sense, the quality offered by the aluminum process is lower, since Cl_2/BCl_3 plasma attacks aluminum with a much wider angle of about $8 - 10^\circ$. It should be clarified however that both etching techniques are layout dependent. As a consequence, these considerations must not be intended as universal rules. Moreover, in the context of this study, better aspect ratios or larger conductor sections do not directly entail better functionality of the component, which has to be assessed as a separate issue. Such will be the focus in the following paragraphs.

4.4.2 Electrical measurements

The measurements on the completed coils were performed using an Agilent 4294A precision impedance analyzer. In particular, the frequency was swept, and the signal was compared to the reference circuit in Figure 4.20. The best fit was obtained in a range comprised between 5 and 800 kHz. Although this study focuses on DC inductance, increasing the upper limit of the frequency sweep was necessary in order to reduce the incertitude on the measurement. Nevertheless, as discussed in paragraph 4.2.2, at 800 kHz the high frequency phenomena that might affect the validity of the models are still inhibited. For the same reason, the influence of the parasitic capacitance C_p appearing in the reference circuit will not be discussed.

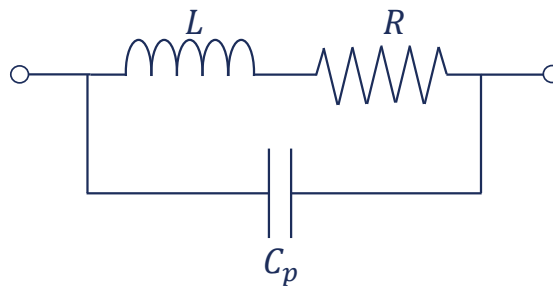


Figure 4.20 – Reference circuit for electrical measurements.

The measured resistivity values for copper and aluminum are equal to $2.0 \cdot 10^{-8} \Omega.m$ and $3.9 \cdot 10^{-8} \Omega.m$ respectively. Both are higher than the bulk values and are strictly dependent on the deposition technique. The theoretical DC resistance of the devices can be estimated from the sections obtained from the morphological characterizations. It should be noted however, that while for type A coils the section was measured with relatively high accuracy using the FIB, the sections of the type B coils were estimated with a far larger degree of approximation, with a consequent propagation of the error on the overall resistance calculation. The results are listed in Table 4.6 (theoretical spacing and widths are reported in order to facilitate coils identification).

Table 4.6 – DC Resistance Measurements

s_{theo} (μm)	w_{theo} (μm)	R_{est} ($k\Omega$)	R_{meas} ($k\Omega$)	Discrepancy
2	2	4.094	4.254	3.9%
2	3	1.957	1.918	2.0%
3	6	0.901	1.005	11.5%
3	7	0.786	0.758	3.6%
3	8	0.646	0.513	20.6%
3	9	0.475	0.467	1.7%

The theoretical values for the inductances must in principle be recalculated for the

Chapter 4. Modeling and manufacturing of single layer planar coils

actual conductor thickness, width and spacing. In practice, all the analytic formulas neglect the conductor thickness. Furthermore, (4.2) and (4.3) compute the same values as long as the average diameter d_{avg} and the filling factor ξ do not change. This happens to be the case, since in both processes what is lost in insulation is gained in terms of conductor width (and vice versa). On the other hand, expression (4.4), in which spacing and width appear explicitly, does compute slightly different values. Although the difference is quite low, the comparison with the measurements will take into account the updated values. Nevertheless, it is worth clarifying that the difference is generated on a purely numerical basis, and formula (4.4) should not be considered as descriptive of width and spacing influences in a comprehensive way. As for the FEM data, simulations showed to be completely insensitive to the section variation. The inductance measurements are reported in Table 4.7 together with the relative errors with respect to the three analytic formulas and the FEM data.

Table 4.7 – Inductance Measurements

s_{theo} (μm)	w_{theo} (μm)	L_{meas} (μH)	ε_{MW}	ε_{CS}	ε_{MF}	ε_{FEM}
2	2	171.1	1.0%	1.1%	3.6%	0.9%
2	3	112.5	3.7%	1.8%	6.4%	2.0%
3	6	33.8	1.8%	0.3%	0.1%	0.3%
3	7	26.7	0.7%	2.6%	3.8%	2.6%
3	8	20.9	6.2%	8.1%	10.1%	8.1%
3	9	18.7	0.5%	1.6%	2.1%	1.6%

As can be observed, all the theoretical predictions are in good agreement with the measured values, with the exception of the type B coil with 8 μm lines. For this configuration, the discrepancy between the theoretical and the measured resistance exceeds 20%. While the aforementioned uncertainty on the estimation of the section can partially explain the discrepancy, the fact that the measured inductance is also the furthest one from the theoretical predictions (7.5% on average depending on the calculation method) with respect to the other configurations, suggests the presence of some fabrication defects in the conductor. In particular, the fact that the resistance and the inductance are lower than expected, endorses the hypothesis that there might be minor short circuits between the conductor lines, probably due to some residual aluminum at the bottom. However, all the aluminum coils were fabricated on the same wafer and were therefore etched under the same conditions. Furthermore, considering that these defects happen to be in a middle configuration, they are likely to be generated by aleatory fluctuations of the process parameters, rather than being a problem of the fabrication method per se.

4.4.3 Comparison with previous works

The measured inductance ranges from 18 to 171 μH . While these values appear far higher with respect to components of equivalent size, it is also true that due to the variety of applications and manufacturing approaches, the evaluation of the performances of inductors designed for different purposes might not be intuitive. An effective and commonly used indicator for fulfilling such task is the inductance density (ID), *i.e.* the inductance per unit area. The values for the presented inductors can be easily computed from the electrical measurements and are listed in Table 4.8. The ID ranges from 2.07 to 19.01 $\mu\text{H}\cdot\text{mm}^{-2}$, with type A coils unsurprisingly performing better. Table 4.9 provides some context, showing a comparison with other significant published works (if not explicitly stated in the reference, *ID* was estimated using the device surface and the peak inductance value). Inductors without a magnetic core usually have ID in the order of hundreds of $\text{nH}\cdot\text{mm}^{-2}$ [SGA01, SM05], and can reach the $\mu\text{H}\cdot\text{mm}^{-2}$ range if multilayer geometries are adopted [TWL02, VC14]. In order to further enhance the performances, a magnetic material is in general needed [LA99, GSP⁺09, MRW⁺15], nevertheless the associated fabrication processes are normally more complex and less scalable. As can be observed, the coils presented here offer the significant advantage of a relatively easy, single-layer, air-core process, with performances above the ones of magnetic core inductors. It should be considered however that maximizing the DC ID was the sole aim of the design strategy (*cf.* paragraph 4.2.1), which in turn didn't take into account for any of the existing trade-offs between achievable inductance, overall impedance and frequency. As a consequence, the quality factor in the frequency range of interest (up to approximately 6 MHz) can be estimated between 0.05 (Al coil with 6 μm lines) and 0.35 (Cu coil with 3 μm lines), while the quality factors in the previous referenced work are far above unity at the respective operational frequencies. In this sense, the technological approach proposed in this work has to be intended as a complementary and non-exclusive strategy for enhancing the performances of small scale inductors.

Table 4.8 – Inductance density

s_{theo} (μm)	w_{theo} (μm)	Inductance density ($\mu\text{H}\cdot\text{mm}^{-2}$)
2	2	19.01
2	3	12.50
3	6	3.75
3	7	2.96
3	8	2.32
3	9	2.07

Chapter 4. Modeling and manufacturing of single layer planar coils

Table 4.9 – Inductance density comparison with previously published inductors

Reference	Core material	Inductance density ($\mu\text{H}\cdot\text{mm}^{-2}$)
[SGA01]	air	0.25
[SM05]	air	0.40
[TWL02]	air	0.94
[VC14]	air	1.12
[LA99]	FeNi	1.60
[GSP ⁺ 09]	CoZrTa	1.70
[MRW ⁺ 15]	MnZn	12.80
This work	air	2.07 – 19.01

4.4.4 Additional indicators evaluation

In order to compare the fabricated coils, 2 different indicators were defined. The first one is the volumic inductance density (VID), defined as the ratio between the measured inductance and the volume occupied by the coil. The choice of evaluating the VID in addition to the ID is motivated by the willingness to take into account the peculiarities of each process. In fact, due to the high resistivity of the material, aluminum coils require thicker lines in order to achieve the same performances in terms of ohmic losses. Such effect is invisible to ID, since it only consider the surface occupied by the coil. For the calculation of the VID, only the active part of the coil was taken into account, while the substrate was not considered. The reason is that in both processes the substrate is far thicker (hundreds of micrometers) than coil themselves, so taking it into account would have numbed the indicator sensitivity. Furthermore, both manufacturing processes allow in principle to reduce the substrate thickness with respect to the starting wafer (*e.g.* with a mechanical grinding step on the backside, as will be seen in next Chapter). Since this was not the case, evaluating the substrate contribution would have not got particular relevance. The second proposed indicator is the inductance to resistance ratio (IRR), which can be considered a simplified form of the commonly used quality factor which does not take into account the frequency. The indicators are reported in Figure 4.21.

As can be observed, the VID tends to decrease as the line width increases. This is a direct consequence of the fact that thinner conductor lines entail higher numbers of turns. In this sense, the copper process performs better, with VID values up to 4 times bigger than the best performing type B coil. As for the IRR, all coils perform between 0.03 and $0.04\mu\text{H}\cdot\Omega^{-1}$, with the exception of the type A coil with 3 μm lines, which shows a particularly favourable IRR. Such configuration also showed (*cf.* Figure 4.17b and 4.4) the thinnest isolation between two adjacent turns. These empirical results show that the Cu/PI process achieves overall better results at the cost of an increased complexity of fabrication. At the same time, they also prove that the Al process is still

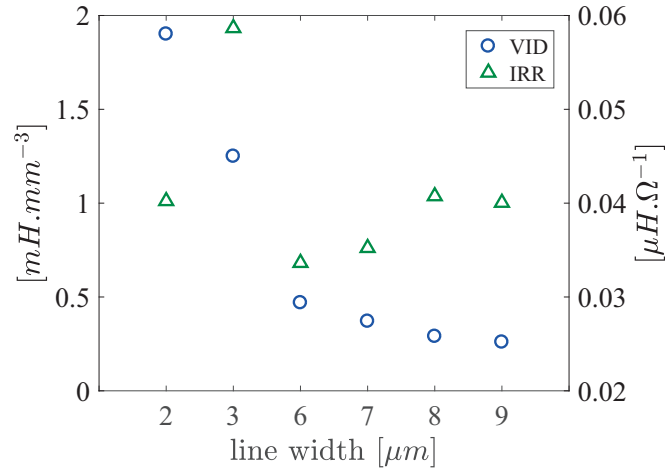


Figure 4.21 – Volumic inductance density (VID) in $mH.mm^{-3}$ and inductance to resistance ratio (IRR) in $\mu H.\Omega^{-1}$ for the type A and type B completed coils.

a valuable option whenever the application requires high inductance to resistance ratios rather than high volumic inductances per se. A significant aspect that needs to be highlighted, is the fact that despite the relatively high ID and VID and disregarding the fabrication process, all the coils have IRR is in the $\mu H.\Omega^{-1}$ range. In other words, the resistive behavior is strongly predominant with respect to the inductive one, and operational frequencies up to tens of MHz are needed in order for the reactance to be comparable with the resistance. This result is highly coherent with the conclusions drawn in Chapter 2 on the consequences of size reduction in MEMS devices.

4.5 Summary and conclusion

In this chapter the design and fabrication of multiple types of planar coils with high turns density was presented. The design was pursued by making use of both analytic formulas and FEM analysis, aiming to maximize the self-inductance of the components. In order to accomplish this objective, two process flows, based on copper and aluminum respectively, were optimized for the reduction of the interwinding spacing. The critical aspects and the limits of each manufacturing approach were discussed. The finished coils were characterized morphologically using different techniques and electrical measurements were performed. The results are in good agreement with the theoretical predictions and the inductance per unit area ranges from 2.01 to 19.01 $\mu H.mm^{-2}$, among the highest values reported in the literature.

In order to evaluate and compare the performances of the completed coils, two indicators were defined and analyzed: the volumic inductance density (VID) and the inductance to resistance ratio (IRR). In particular, VID up to 1.90 $mH.mm^{-3}$ were ob-

Chapter 4. Modeling and manufacturing of single layer planar coils

tained using the copper based process (2 μm linewidth), while a maximum VID of 0.47 $\text{mH}\cdot\text{mm}^{-3}$ was obtained using the aluminum process (6 μm linewidth). As for the IRR, the copper coil with 3 μm linewidth was the best performing, with a value of 0.06 $\mu\text{H}\cdot\Omega^{-1}$. This result is particularly significant as it provides an experimental validation of the assumptions made on the basis of the scaling laws.

From a more general perspective, both manufacturing methods are reliable and versatile. Each process has its own advantages and drawback and the choice of the most suitable one depends on the particular application. In this sense, next Chapter will focus on the fabrication of the MEMS generator on the basis of the morphological and electrical characterizations of the single layer coils presented here.

Publications related to this chapter:

- J. Poliakine, Y. Civet, Y. Perriard, Design and Manufacturing of High Inductance Planar Coils for Small Scale Sensing Applications, In *Procedia Engineering*, Volume 168, 2016, Pages 1127-1130.
- J. Poliakine, Y. Civet and Y. Perriard, "Microfabricated planar coils with high turns density: Design and manufacturing," 2016 19th International Conference on Electrical Machines and Systems (ICEMS), Chiba, 2016, pp. 1-6.
- J. Poliakine, F. Copt, D. M. Araujo, Y. Civet and Y. Perriard, "Modeling, Design, and Manufacturing of Microfabricated Coils With High Inductance Density," in *Journal of Microelectromechanical Systems*, vol. PP, no. 99, pp. 1-11.

5 MEMS generator prototyping

This chapter presents the fabrication and the characterizations of the MEMS generator for the watchmaking application described all along this thesis.

At the end of Chapter 3, several possible configurations were optimized. Nevertheless, a final choice could not be made, due to lack of information on the actual technological possibilities. In this sense, the results obtained in the framework of pilot study presented in Chapter 4, were used in order to discriminate feasible and non feasible solutions, and finally operate a selection on such basis.

Then the copper based process used in Chapter 4 for the fabrication of single layer coils will be upgraded for the manufacturing of multilayer structures. Pursuing this objective, required modification at a layout level as well as the optimization of additional fabrication steps. In this context, the reader will be made aware of the motivations behind the technological approaches that were adopted, with a particular focus on the realization of the interlevel insulating layer and the devices liberation from the substrate.

Finally, the implementation of the generator in the watch movement will be presented and electrical characterizations will be performed and discussed in detail.

5.1 Choice of the fabrication method

In Chapter 3 an algorithm was conceived and used for the optimization of the stator construction parameters. The procedure identified three possible configurations, reported in Table 3.9, which represented a compromise between performances and ease of fabrication. At this stage however, feasibility was roughly assessed on the basis of the technical and scientific literature on the subject. This was not sufficient for a finer determination of the more suitable solution, which in turn had to take into account the actual limits of the available technology. In this sense, the results obtained from the study in Chapter 4 helped to fill such gap. A first implication of such findings concerns the resistivity values of the employed materials. In fact, an important parameter for each possible stator configuration is the minimal value for the conductor section in order to comply with the resistance requirement. However, this value was calculated by taking into account the bulk resistivities of copper and aluminum, while the study on single layer coils revealed poorer performances. Table 5.1 reports the three possible solutions (namely *a*, *b* and *c*) identified by the optimization algorithm with the updated value for the minimal section. Theoretical aspect ratios were removed, as they referred to the nominal value of conductor width, which was also found to vary significantly.

Table 5.1 – Electromagnetic torque optimization results (updated)

Stator ID	e (μm)	turns #	layers #	k_{ph} (V.s)	T_{em} ($\mu\text{N.m}$)	Section (μm^2)
a	4	199	3	0.0105	0.062	14.7 – 30.0
b	5	159	4	0.0111	0.069	15.8 – 31.9
c	6	132	5	0.0116	0.075	16.4 – 33.1

In paragraph 3.3.9, it was conjectured that the most packed configurations, *a* and *b*, were challenging or unfeasible with the aluminum process due to the high values of theoretical aspect ratios. The results of the study on single layer coils definitely confirm this assumption, since the combined effect of the increased material resistivity and the conductor width reduction due to overetch (*cf.* paragraph 4.3.4) tends to complicate the fabrication even more (*i.e.* even higher aspect ratios would be required). As for the copper process, it can be observed from Table 4.4, that the section requirement is met only for configuration *b* ($18.2 \mu\text{m}^2$), while *a* has a smaller section ($10.8 \mu\text{m}^2$). In such case, the etching of PI could in principle be slightly pushed further in order to enlarge the section (Figure 4.17(a)). Even so, the required section is unlikely to be obtained before compromising the interturn insulating layer. For what concerns configuration *c*, it cannot be considered attractive in the context of the copper process, since *b* is equally feasible and it also includes a lower number of layers. In turn, the implementation of this solution using the aluminum process needs to be discussed. This can be done on the basis of the results obtained in previous chapter (Table 4.5) as well, even though a coil with the same horizontal encumbrance was not directly

fabricated in that framework. The minimal section for c is equal to $33.1 \mu\text{m}^2$, so that if the nominal values of width and spacing are considered (4 and $2 \mu\text{m}$), a thickness of $8.3 \mu\text{m}$ would be necessary. However, lateral etching will tend to thin the conductor. The entity of such phenomenon was actually quantified: for a comparable Al thickness, the amount of total overetch was of about $2.5 \mu\text{m}$ (*cf.* Figure 4.19), which is bigger than the nominal spacing itself. In line of principle the phenomenon could be compensated at a lithographic level. In this particular case however, this approach would entail the fabrication of $8 - 10 \mu\text{m}$ thick photoresist patterns with submicron resolutions, which is substantially impossible with standard lithographic techniques. For these reasons, only the solution b was retained.

In order to keep the development compatible with the available resources, it was chosen to demonstrate the process by manufacturing a simplified prototype including only 2 layers instead of 4. Nonetheless, the following dissertation will always contemplate the extension of the process for the fabrication of the complete 4 layers device. Such topic will be repeatedly brought to attention. From a functional point of view, since the magnetic coupling is linear with respect to number of layers (*cf.* (3.13)), expected phase constant is halved with respect to the values reported in Table 5.1. On the other hand, braking torque is expected to decrease more, since it depends quadratically (*cf.* equation (3.9)) on the magnetic coupling.

Because the process flow for single layer coils has already been discussed extensively in Chapter 4, the following sections will just focus on some subtle design and layout modifications that were introduced, and later jump directly to the electrical characterizations of the first layer coils.

5.2 Multilayer coils fabrication

5.2.1 Design modifications

In order to pursue the fabrication of the stator, the copper process shown in Chapter 4 must be upgraded in order to allow the building of multilayer structures. Other than the obvious introduction of supplementary process steps, this task also comprises some modifications at a design level. In fact, when it comes to multilayer coils, several issues arise which were not problematic for single layer structures, especially in terms of planarity and uniformity. The first issue, is the presence of relatively large features in the polyimide mold, an example of which are the connection pads. These structures are squares with a side of $250 \mu\text{m}$, much larger than the conductor width (see Figure 4.12). When it comes to filling the trenches (Figure 4.5(d)) these structures become problematic. In fact, copper growth during electroplating is substantially omnidirectional (Figure 5.1(a)). As a result, smaller gaps reach complete filling earlier and since the process is usually stopped at this point, a recess is created over the pad (Figure

5.1(b)).

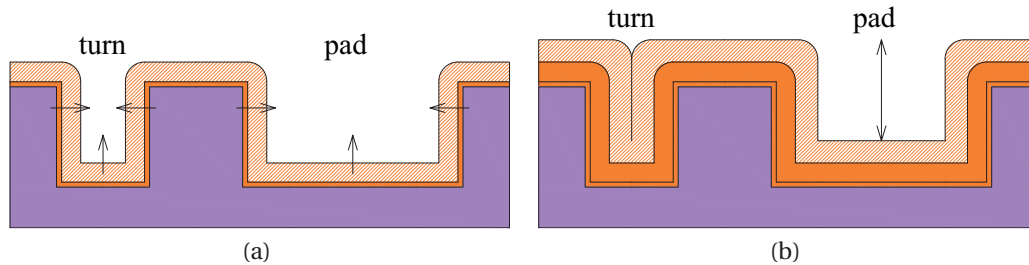


Figure 5.1 – Omnidirectional copper growth during electroplating: (a) early stages, (b) filling of smaller gaps.

The depth was measured using a mechanical profilometer and found equal to $3.5\ \mu\text{m}$. For single layer coils, this does not represent a problem, since an incomplete filling does not compromise electrical continuity. However, stacking additional layers becomes difficult due to the fact that the recess depth is significant with respect to the thickness of the materials to be deposited and patterned on top of it (*cf.* Figure 5.9). In practice, the pads become epicenters of mechanical defects, causing local and global delamination issues (especially during the CMP of the second layer). Several strategies were considered to address the issue. A first possibility was to reduce the pads size and thus the associated recess depth. However, such approach would have complicated the alignment of the VIAs between the two copper layers. Electrical measurements would have become difficult as well, since the needle probes used for this purpose have a relatively large diameter and therefore require a large pad to be landed correctly. The second strategy, that was actually tested, was to extend the electroplating duration in order to completely fill the pads from the bottom. While the technique proved to be effective, the main drawback is that several microns of unnecessary copper are also grown on top of already filled trenches. This translates into overly increased duration of the CMP step (up to four times), with consequent wear of the equipment and poor results in terms of uniformity. Finally, the most effective strategy was to modify the pad by introducing some polyimide patterns as in Figure 5.2. The role of these structures is to act as poles for the copper growth. Their size is chosen so that the resulting copper lines match the width of the coil turns, so that the filling is completed in the same amount of time. This method allows keeping a pad large enough to guarantee effortless measurements as well as a simple alignment. Moreover, since the resulting copper lines are variously connected, there are no significant consequences in terms of contact resistance. Figure 5.3 shows a pad obtained with such method. Mechanical profilometer measurements showed a final gap of about $600\ \text{nm}$ for both the pad and the conductor network. Such height difference is inherently associated with the CMP step itself (dishing and erosion) and although it could be theoretically reduced, it cannot be completely erased. In practice, $600\ \text{nm}$ were sufficient to ensure the stability of the remaining fabrication steps.

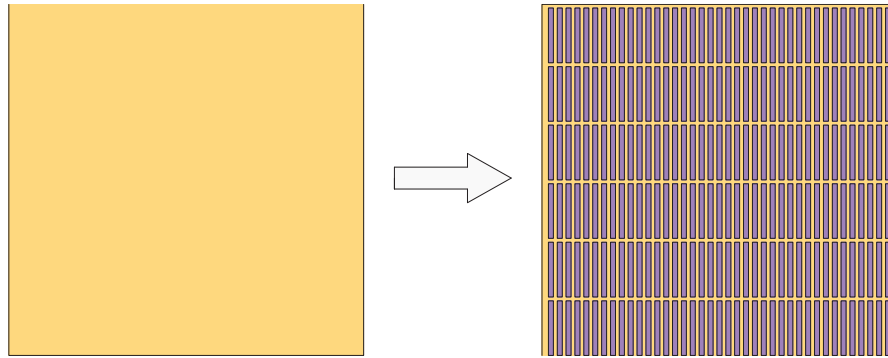


Figure 5.2 – Modification of the connection pad by introducing PI structures.

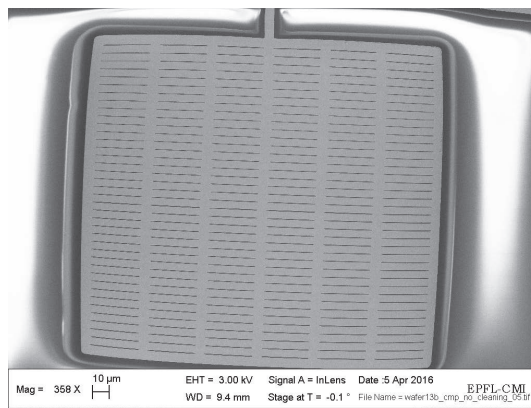


Figure 5.3 – A completed pad (first layer) including PI pattern.

5.2.2 Connection scheme

The disposition of the six coils of the first and second layer are shown in Figure 5.4.

The connection scheme goes as follow. On each layer, the coils sectors are equally oriented. Because of the alternating magnetization of the magnet, if a sector sees a back EMF promoting clockwise circulating current, contiguous sectors will undergo opposing electric polarization. Hence, on the first layer, the coils are connected in pairs, so that the induced voltages are in series. As for the second layer sectors, they have a mirrored geometry and are electrically linked to the first layer through the squared VIAs in the center. This ensures that the induced voltage is coherent between the two layers. Second layer coils are then connected in pairs with a sector shift with respect to the first layer, so that the total EMF can be harvested. This method allows to reduce the overall number VIAs. Moreover, the process steps are also reduced, since all of the necessary connections are automatically obtained once the second layer is completed. The major drawback however, is that the coils cannot be characterized independently. In fact, any electrical measurement will forcibly include either the series of two sectors (first layer) or the completed stator (second layer). In general, this

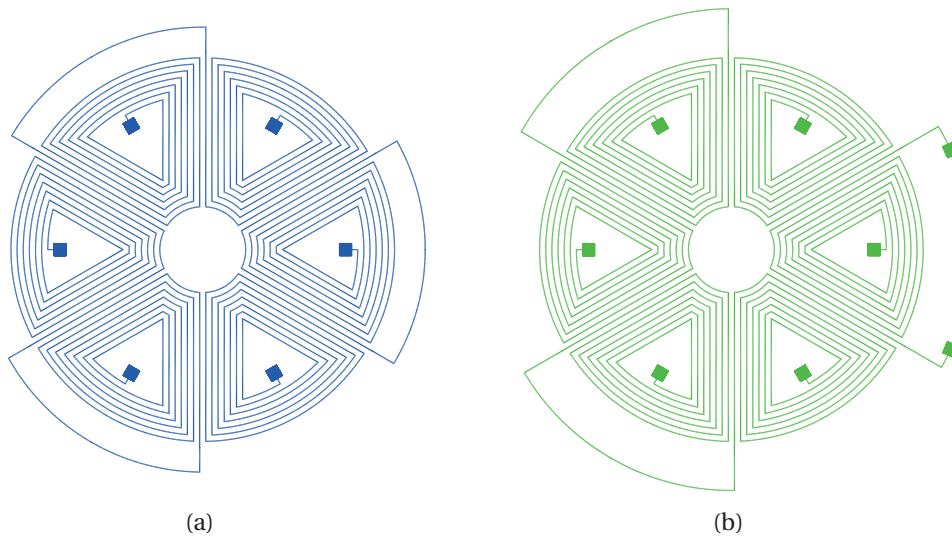


Figure 5.4 – Stator coils layout: (a) first and (b) second layer.

is not a main concern, especially as long as many functional structures can be found and used as a reference. Nevertheless, locating small defects and diagnosing failures becomes more difficult.

5.2.3 Wafer layout

Silicon wafers with a diameter of 100 mm were used as the starting substrate. The disposition of the stators on the wafer surface can be observed in Figure 5.5.

Other than smaller features for alignment and testing, the layout comprises 48 stators, distributed in 6 rows. As can be observed, the number of devices could in principle be increased in order to better exploit the available surface. There are however two main reasons why this was not done. The first (trivial) one is that all the lithographic steps are pursued by directly exposing the photoresist using a laser source, which is put in relative motion with respect to the substrate. By all means, the procedure requires the pattern to be numerically handled by the machine. Because of the enormous quantity of information (each stator in Figure 5.5 consists of thousands of lines), such task may not be accomplished correctly. Hence the interest in limiting the number of stators. However, the most important reason is that copper deposited by electroplating is not uniform on the wafer surface and significant differences in thickness (in the micron range) may occur between the center and the peripheral areas of the wafer. In general, although the following CMP step reduces the impact of such issue, a perfect rectification is unlikely to be obtained. For single layer coils, this is not a major obstacle, since the process is basically stopped after the CMP. On the other hand, for multilayer coils it is crucial to keep the substrate as planar and defect-free as possible. In this sense,

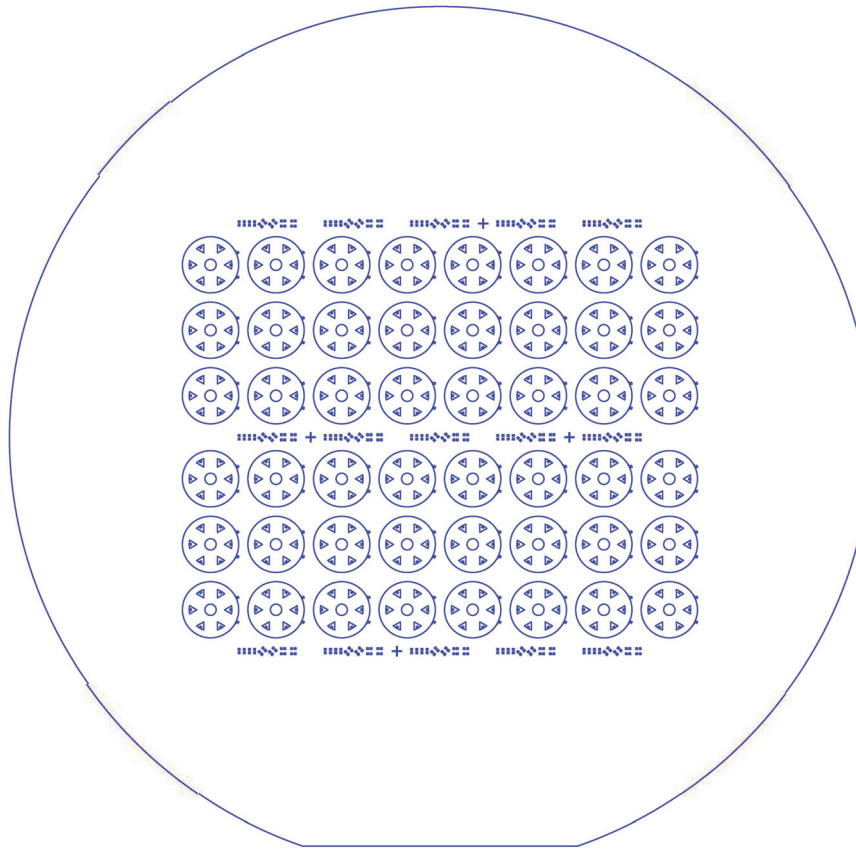


Figure 5.5 – Stators disposition on the surface of the 100 mm wafer.

the layout of Figure 5.5 concentrates the devices in a relatively uniform deposition zone (empirically determined) and keeps the peripheral zone clear of devices that are likely to end up non functional.

5.2.4 First layer measurements

After the fabrication of the first layer, pursued following the standards discussed above, the coils are characterized electrically. In particular, a simple 2-points resistance measurement allowed to identify the functional stators, in which the resistance has an acceptable value, as well as the defective ones, for which the resistance is too high or too low. The theoretical resistance for each sector is equal $1.1 \text{ k}\Omega$, while the targeted value for the whole stator is equal to $30 \text{ k}\Omega$ (hence $15 \text{ k}\Omega$ for the 2-layer prototype). Since on the first layer the 6 sectors are connected in pairs, the measured values refer to the series of two coils. Considering that the layout comprises 48 stators (*cf.* Figure 5.5), the complete electrical characterization of the first layer requires 144 measurements in total. Each measurement is conducted by applying a DC voltage sweeping between 0 and 500 mV . Such values were chosen as they reflect the actual operating conditions.

Chapter 5. MEMS generator prototyping

Figure 5.6 reports the results for one particular wafer, nevertheless the trends that will be identified and discussed are common to all the wafers processed during the project. Each square represents a stator and encloses the measured values for the three coils pairs (all of them must be functional). In order to increase readability, fitting measurements are highlighted in green, while disproportionately high and low values are highlighted in red and yellow respectively.

2.42E+03	2.29E+03	2.08E+03	2.34E+03	2.33E+03	2.34E+03	2.34E+03	2.65E+03
2.62E+03	2.36E+03	2.33E+03	2.03E+03	2.35E+03	2.37E+03	2.43E+03	2.67E+03
2.61E+03	2.31E+03	2.30E+03	2.33E+03	2.33E+03	2.34E+03	2.34E+03	2.53E+03
2.28E+03	2.26E+03	2.24E+03	2.23E+03	2.28E+03	2.34E+03	2.32E+03	2.60E+03
2.37E+03	2.18E+03	2.28E+03	2.25E+03	2.28E+03	2.33E+03	2.32E+03	2.45E+03
2.36E+03	2.25E+03	2.25E+03	2.24E+03	2.26E+03	1.93E+03	2.34E+03	2.35E+03
2.29E+03	1.65E+03	2.22E+03	2.24E+03	2.24E+03	3.72E+05	2.42E+03	2.45E+03
2.31E+03	2.25E+03	2.21E+03	2.21E+03	1.49E+03	2.14E+03	2.06E+03	2.41E+03
2.33E+03	2.27E+03	1.94E+03	2.22E+03	2.22E+03	2.31E+03	4.78E+05	2.41E+03
2.55E+03	2.49E+03	2.51E+03	2.50E+03	2.50E+03	2.61E+03	2.71E+03	2.71E+03
3.04E+05	2.49E+03	2.50E+03	2.50E+03	2.51E+03	2.58E+03	2.69E+03	2.71E+03
2.50E+03	2.47E+03	2.17E+03	2.48E+03	2.50E+03	2.55E+03	2.36E+03	2.71E+03
2.66E+03	7.44E+05	1.02E+06	2.50E+03	2.55E+03	2.64E+03	2.71E+03	2.78E+03
2.60E+03	2.49E+03	2.51E+03	2.50E+03	2.53E+03	2.64E+03	2.72E+03	2.74E+03
2.77E+03	2.49E+03	2.47E+03	2.49E+03	2.52E+03	2.61E+03	2.70E+03	2.68E+03
2.78E+03	2.53E+03	2.43E+03	7.06E+05	2.60E+03	2.68E+03	2.69E+03	2.88E+03
2.78E+03	2.51E+03	2.43E+03	2.48E+03	2.54E+03	2.62E+03	2.71E+03	2.78E+03
2.86E+03	2.62E+03	2.41E+03	2.48E+03	2.53E+03	2.62E+03	2.70E+03	2.18E+03

Figure 5.6 – Electric resistance (Ω) for the first layer coils (green = functional value, red = too high, yellow = too low).

The measurements show a narrow distribution around the average value, which for the stators in the first three rows is extremely close to the theoretical value of 2.2 k Ω . For the last three rows the measurements are also very little dispersed, but the average value is slightly higher (around 300 Ω). The reason is that these devices included slightly larger nominal insulation in order to compensate for lateral overetch. As a consequence, the resulting section is smaller. It can also be remarked that peripheral stators tend to have higher resistances. This is a direct effect of the non-uniformity associated with electroplating. In fact, copper tends to be deposited at a higher rate on the center of the wafer. As a result, when it comes to planarization, devices in the periphery are uncovered earlier during CMP with respect to the ones in the center. Therefore, such devices are more exposed to polishing, which reduces their section. The particular choice of the layout, discussed in previous paragraph, allows to contain this effect. Globally, up to 95% of the coils are properly manufactured, which in turn translates into 84% of functional stators. Such result is particularly significant, since the percentage of success is compatible with the fabrication of prototypes with 4 or more number of layers. As for the failures, "red" values, which basically correspond to the loss of the electrical contact, are usually associated with random abrasion of copper fragments from the conductor. This type of defects is usually induced by CMP and must be considered as inevitable. Other causes of failure include unexposed photoresist during

lithography, which results in faulty PI molds (Figure 5.7).

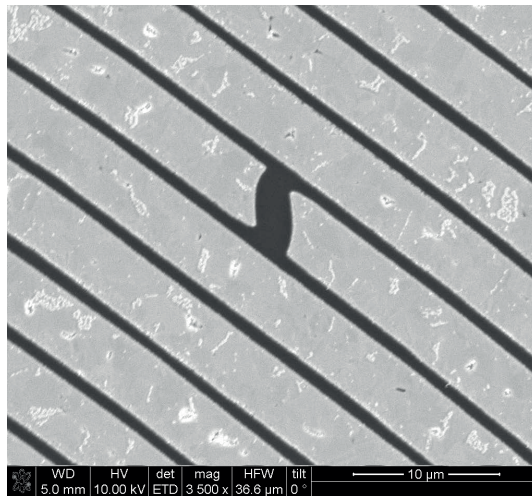


Figure 5.7 – Loss of electrical contact due to defective PI mold.

Low resistances ("yellow" values) are in general less frequent. One possible cause is mechanically deformed insulation (Figure 5.8(a)) causing short circuits between the coils turns. In this case however, the "yellow" values are likely to be numerous and have a broader distribution on the surface. Moreover, in the author experience, if the PI mold has not been processed properly, incomplete copper filling and delamination issues are likely to arise in earlier fabrication stages. In this context, occasional short circuits as depicted in Figure 5.6, are often caused by a residual thin layer of copper after IBE cleaning (Figure 5.8(b)). The issue can in principle be addressed by extending such treatment. However, since IBE is aggressive on copper, this will also endanger coils that are already functional. Trade offs in this sense must thus be balanced carefully.

Resistance measurements were repeated whenever possible throughout the process, in order to validate each step and diagnose any issues (*e.g.* unopened VIAs).

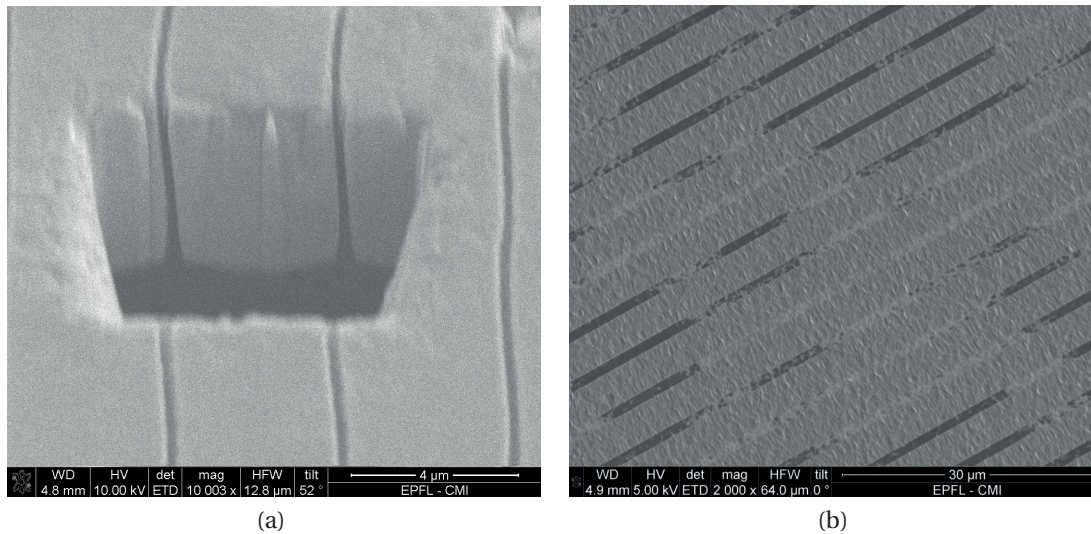


Figure 5.8 – Examples of defects leading to short circuits: (a) mechanical deformed insulation and (b) residual copper after CMP.

5.2.5 Updated process flow

An outlook of the updated process is shown in Figure 5.9. Other than the design modifications discussed above, the steps for the fabrication of the first layer are the same as presented in paragraph 4.3.2. In particular, prototypes with both Al and SiO₂ adhesion layers between substrate and polyimide were successfully fabricated. Also, for the seed layer it was preferred the combination of evaporated Ti/Cu with respect to sputtered Ta/Cu. This was motivated by overall better adhesion performances as well as by the fact that titanium is also involved in other fabrication steps (high consistency of materials is a good practice when designing MEMS). The fabrication of the second layer follows the exact same principle. In turn, a significant effort was dedicated to finding a reliable method for the realization of the insulating layer. The fabrication steps will be discussed individually below.

Step (a)

The objective of the first step is to cover the VIAs with a layer of titanium. The latter serves the purpose of protecting the underlying copper from direct exposure to the O₂ and CF₄ plasma used for the structuring of the second level PI mold. This would cause oxidation of the copper and, most important, contamination issues in the plasma chamber. Several methods were tested in order to accomplish this step, including lift-off [Mad02] and selective deposition through a silicon stencil mask. The first approach required multiple hours of treatment in a wet environment, which was problematic for the PI/Cu substrate. Moreover, the results observed were quite poor, with partial

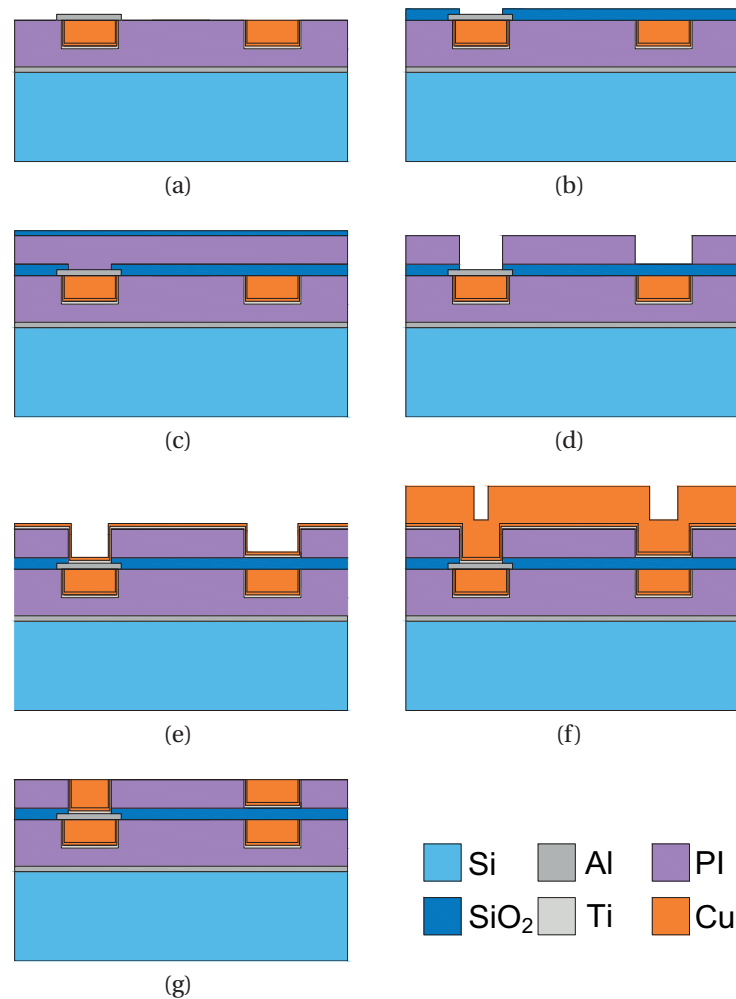


Figure 5.9 – Schematic of the Cu process flow: (a) Deposition and wet etching of 200 nm Ti, (b) 2 μm SiO_2 deposition and etching, (c) 4.5 μm PI + 200 nm SiO_2 deposition, (d) PI mold structuration, (e) 40 nm Ti + 250 nm Cu deposition, (f) Cu electroplating, (g) CMP + IBE cleaning.

delamination of the Ti layer over the pad and large Ti fragments randomly redeposited over the wafer surface (Figure 5.10). The stencil mask method was also tricky because of mechanical issues affecting alignment and quality of the deposited material.

A more effective strategy was instead to sputter titanium on the whole wafer surface, mask the connection pads using lithography and subsequently remove Ti from the unwanted areas. For this task, IBE was tested as the etching technique. Despite its effectiveness in terms of Ti removal, IBE presents two major drawbacks. First of all it has no selectivity with respect to copper (see paragraph 4.3.2). Also, the mechanical action exerted by argon ions has the effect of hardening the masking photoresist, which becomes insoluble in standard solutions. Finally, a successful method was to use a

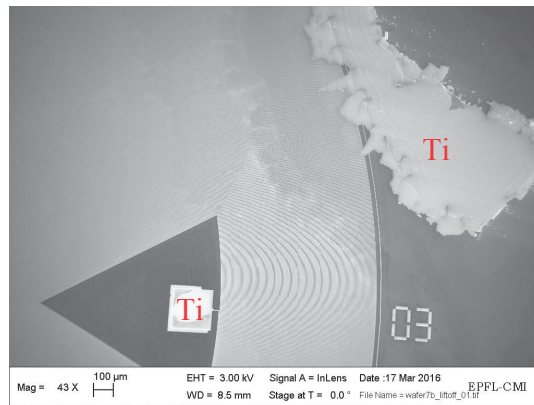


Figure 5.10 – Delamination and redeposition defects after Ti liftoff.

highly diluted ($\approx 1\%$) solution of hydrofluoric acid. The latter has the significant advantage of not attacking the PI/Cu substrate. Also, the etching rate with respect to titanium is extremely high (in the order of microns per minute) which allows the step to be performed rapidly and under visual control. Photoresist properties stay unchanged, so that the stripping is also accomplished easily. Figure 5.11 shows the protected pads for one coil and some test structures.

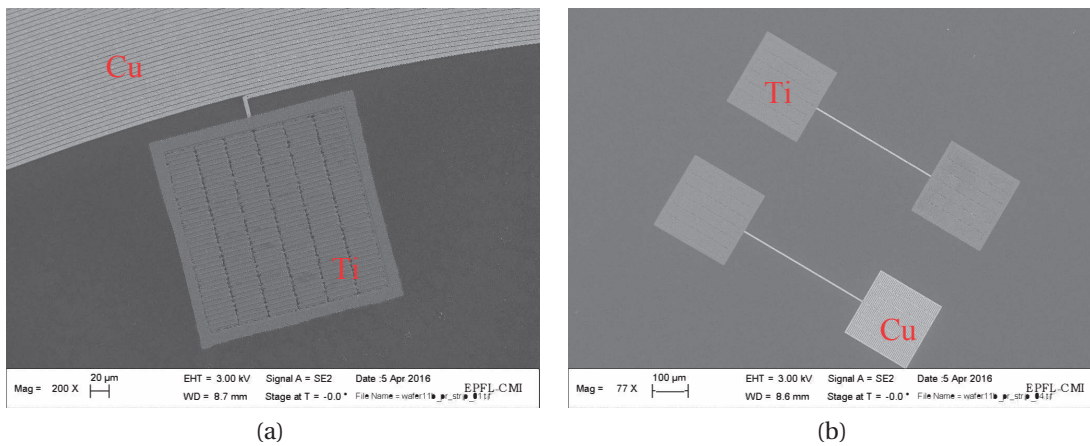


Figure 5.11 – Ti cap over interconnection pads: (a) coil and (b) test structures.

Step (b)

Once the VIAs are covered in Ti, a $2\ \mu\text{m}$ thick SiO_2 layer is sputtered all over the surface. Considering that silicon dioxide has a dielectric strength of about $10^9\ \text{V/m}$ and that at the controlled speed the voltage difference between the two layers is below 1 V, such thickness largely ensures proper electric insulation. The choice of SiO_2 as the insulating material requires however clarification. In fact, as discussed in paragraph 4.3.1, copper atoms tend to diffuse in adjacent materials (especially polymers and dielectrics like

SiO₂). In order to address this issue, a diffusion barrier is usually needed. The Titanium seed layer accomplishes this function between the copper and the polyimide mold, but in principle a diffusion layer is also needed at the interface with the insulating layer. For example Pisani [PHB⁺05], who also presented inductors based on a Cu/PI damascene process, solved the problem by depositing a thin Ta diffusion barrier on top of the first level copper, and realized the insulation in PI. The same strategy could not however be applied here. In fact, due to the comparatively high density of the pattern, the alignment of the diffusion barrier with the copper lines would have been impossible. Moreover, since Ti (as well as other diffusion barriers) is conductive, this would also have created short circuits between the turns, thus making the component unusable. In this context, the choice of a uniform SiO₂ layer as insulation, represents a compromise based on the assumption that the diffusion of copper atoms in such material is activated at high temperatures (≈ 400 °C as demonstrated by McBrayer [MSS86]) with respect to the operating conditions. This assumption was also validated to some extent during the process itself. In fact, the highest temperature reached is 300 °C and corresponds to the PI hard bake. In this sense, electrical measurements performed on the first layer coils after the hard bake of the second level PI did not show any problem associated with diffusion.

After the material deposition, another lithographic step is performed and the insulating layer is then etched using a CF₄ plasma until the electric contact on the VIAs is recovered. The step is controlled using an online interferometer and success is further validated by measuring electrical resistance and comparing the results with the values obtained before the completion of the first layer.

Steps (c)-(d)

At this point the actual fabrication of the second layer sectors begins with the deposition on the insulating layer of 4.5 μm of PI followed by 200 nm of SiO₂ for masking purposes. Unlike the sectors on the first layer, for which the PI layer was only partially etched, here the mold must be etched through all of its thickness. As a consequence, the deposition of PI requires additional vigilance. In fact, if the layer is too thick, the plasma treatment might damage the mold (*cf.* Figure 4.7) before electrical contact on the VIA is recovered. At the same time, if the layer is too thin, the risk is to obtain small conductor sections. A FIB cross section of the second level PI mold is shown in Figure 5.12. In this particular case, the PI layer was slightly thinner than the targeted value. As a result, the insulation is mechanically stable, but the resulting conductor section will be smaller. The blatant thickness difference between the interturn insulating structures of the two levels also certifies this fact. Figure 5.13 depicts the PI mold for a pad on the second level. The mold includes the patterns discussed in paragraph 5.2.1 and on the bottom the titanium protecting the underlying VIA (on the first level) can be spotted.

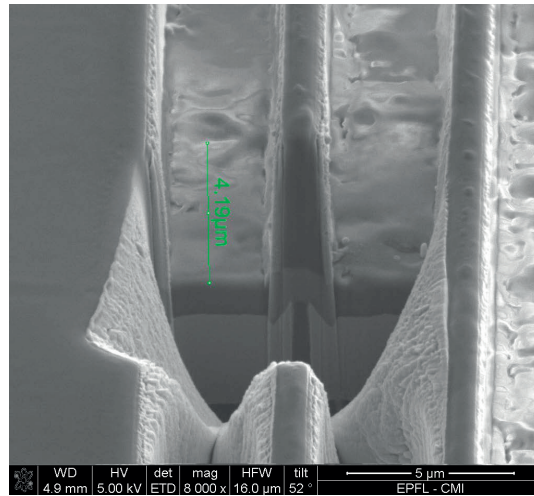


Figure 5.12 – FIB cross section of the 2nd layer polyimide mold.

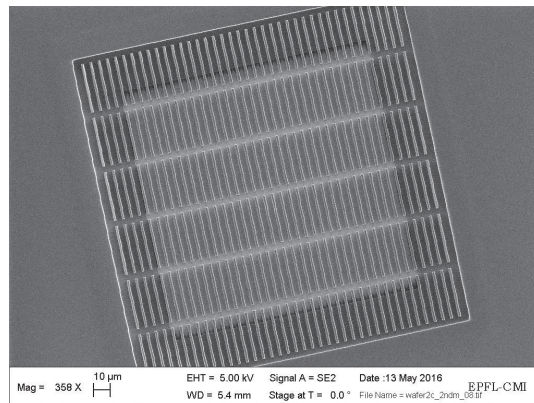


Figure 5.13 – 2nd layer connection pad and underlying Ti VIA.

Steps (e)-(f)-(g)

The seed layer deposition as well as the electroplating, the CMP and IBE cleaning are performed in the exact same way as for the first layer. From a functional point of view, the superposition of two layers leads to the generation of a capacitive coupling between the coils, which for the wide majority of applications, including the one of interest, is unwanted. One possible strategy to minimize this effect is to shift the first and second layer turns as in Figure 5.14 in order to minimize the overlapping surfaces. This, however, could not be implemented in this case, since the conductor width is larger than the interturn insulation (see Figure 4.17). A rough calculation based on the insulating properties of SiO_2 and the geometry of the system, allows to estimate a parasitic capacitance in the order of hundreds of pF. At the frequencies of interest, this translates into a reactance of tens of $\text{M}\Omega$, which is several orders of magnitude higher than the inner impedance of the coils. One can therefore conclude that for the present application the performance drop associated with this effect is not significant.

Nevertheless, the issue needs to be addressed for higher operational frequencies.

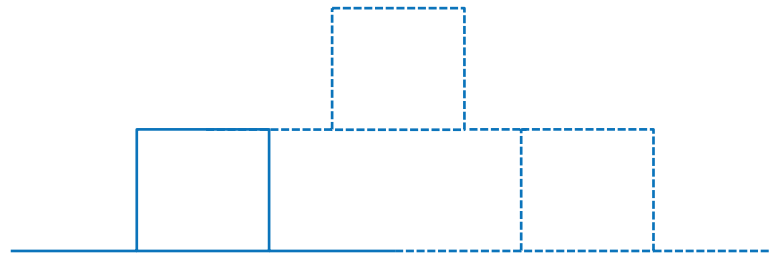


Figure 5.14 – Shift between first and second level turns.

Some details of a completed 2-layer stator are shown in Figure 5.15. Since PI is quasi transparent, the conductor on the first layer can be noticed (on a different focal plane). Below, Figure 5.16 shows a FIB cross section (for qualitative appreciation, since proportions are slightly distorted).

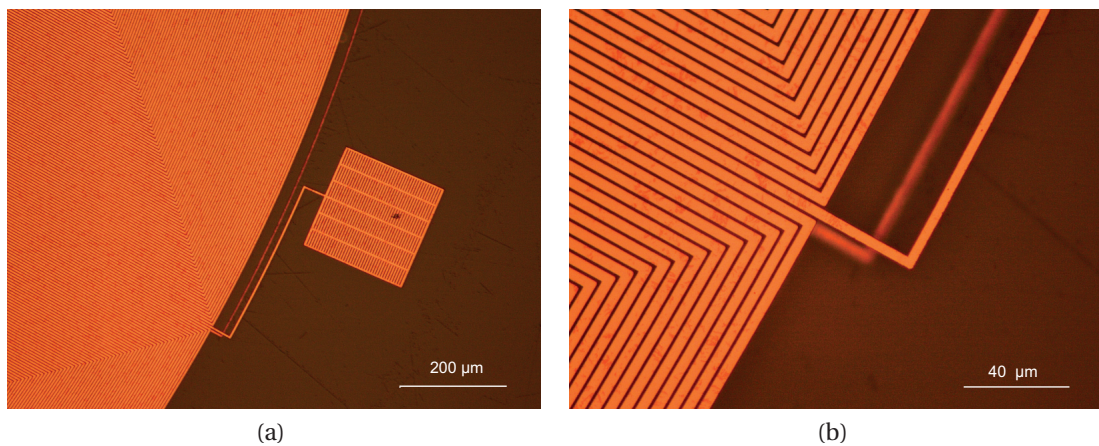


Figure 5.15 – 2nd layer after IBE cleaning: (a) connection pad and (b) pattern detail.

5.2.6 Second Layer measurements

After the IBE cleaning, resistance measurements are performed following the same approach discussed in paragraph 5.2.4. As previously discussed, the two layers are designed so that on the second level all of the 12 sectors result connected in series (*cf.* Figure 5.4). As a consequence, a complete characterization requires 48 measurements in total. Assuming that the conductor section is the same for the two copper levels, a theoretical value of 13.2 k Ω can be estimated for the overall resistance of the device. Of course, actual values are expected to vary, nevertheless this is not an issue as long as they comply with the functional requirements (15 k Ω) and their distribution is relatively narrow. Figure 5.17 reports an example of second layer characterization.

As can be observed, the measurements are highly coherent with the theoretical prediction,

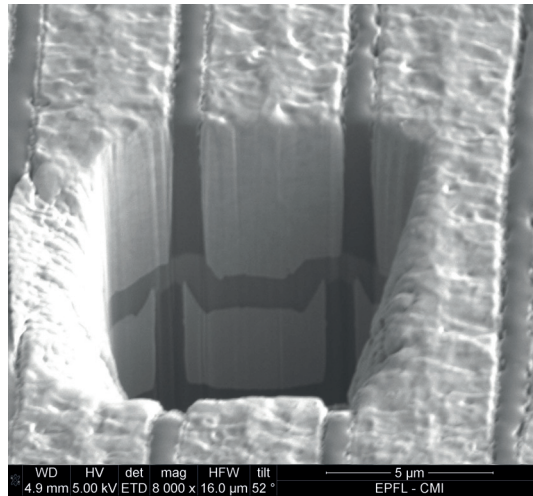


Figure 5.16 – Cross section of a 2-layer stator after IBE.

1.24E+04	1.10E+04	1.21E+04	x	1.22E+04	1.22E+04	1.06E+04
x	x	x	x	1.28E+04	1.24E+04	x
1.23E+04	1.22E+04	4.36E+03	x	1.25E+04	1.23E+04	1.25E+04
1.36E+04	1.32E+04	1.34E+04	x	1.26E+04	x	1.36E+04
1.37E+04	x	x	x	8.95E+03	1.34E+04	x
x	x	1.34E+04	1.32E+04	1.32E+04	1.34E+04	x

Figure 5.17 – Electric resistance (Ω) for the second layer coils (green = functional value, red = too high, yellow = too low).

with an average value of 12.2 k Ω for the upper three rows, and 13.4 k Ω for the bottom devices which, as discussed in section 5.2.4, provide larger nominal insulation. For this wafer, the success rate measured after the electrical characterizations on the first layer was of about 93 % (functional coils pairs), so that 30 functional devices were expected after the completion of the second layer. The actual number is however slightly lower and equal to 26. This is due to the fact that failures are not only inherent to the PI/Cu process block, but they are also induced by other intermediate steps (*e.g.* the fabrication of the insulating layer) and wafer manipulation in general. It should however be noted that the the success rate would still be sufficient for obtaining a significant number (> 10) of functional devices including four copper levels. Moreover, from a scalability perspective, sources of defects can in principle be minimized in a dedicated environment.

5.3 Stator Liberation

After the completion of the second layer, the stators needed to be extracted from the substrate in order to be assembled with the rotor. A common technique to perform such task in MEMS and microelectronic applications in general, is to use a dicing saw

5.3. Stator Liberation

in order to cut through the substrate and separate the samples. However, this approach could not be adopted due to the fact that dicing occurs along straight lines, while a round shape is required in order for the stator to be assembled in the watch movement. On top of that, in the chosen double magnet configuration (*cf.* Figure 3.1) the stator must be cut in the center to allow the passage of the rotor shaft. The process flow was therefore extended in order to obtain the desired geometry. The basic steps are reported in Figure 5.18, and will be discussed in detail below.

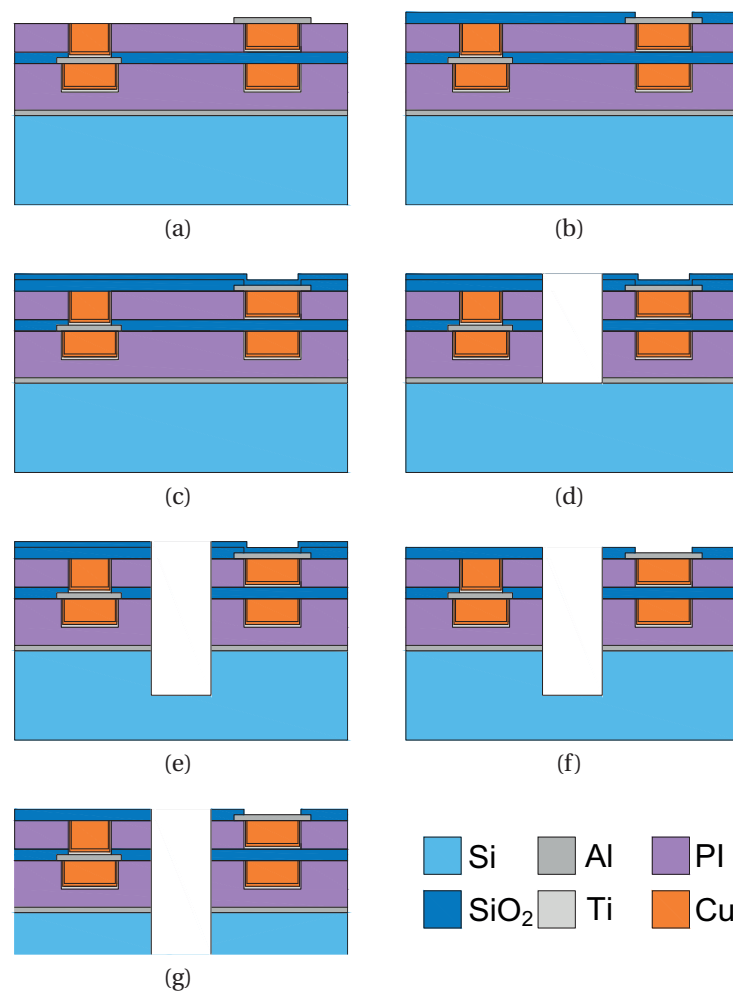


Figure 5.18 – Extended process flow for stators liberation: (a) Deposition and wet etching of 200 nm Ti, (b) 2 μm SiO_2 deposition and etching, (c) 1 μm SiO_2 deposition, (d) Plasma etching of 3 μm SiO_2 + 4.5 μm PI + 2 μm SiO_2 + 10 μm PI + 150 nm Al (or SiO_2), (e) DRIE of $\sim 90 \mu\text{m}$ Si, (f) Plasma etching of 1 μm SiO_2 , (g) Backside grinding.

Steps (a)-(b)-(c)

The first two steps recall exactly the fabrication of the insulating layer as seen in paragraph 5.2.5. The pads for the connection with the outer world are protected with a thin layer of Ti. Then 2 μm of SiO_2 are deposited and patterned using a CF_4 plasma in order to restore electrical contact. The oxide layer serves as a chemical protection towards the plasma treatments that will follow, but it also provides mechanical protection. The latter will be especially needed in the last stages of liberation, as will be discussed shortly. Figure 5.19 shows a FIB cross section of a 2-layer structure covered by the SiO_2 protective layer (on this particular wafer the thickness is below the targeted 2 μm).

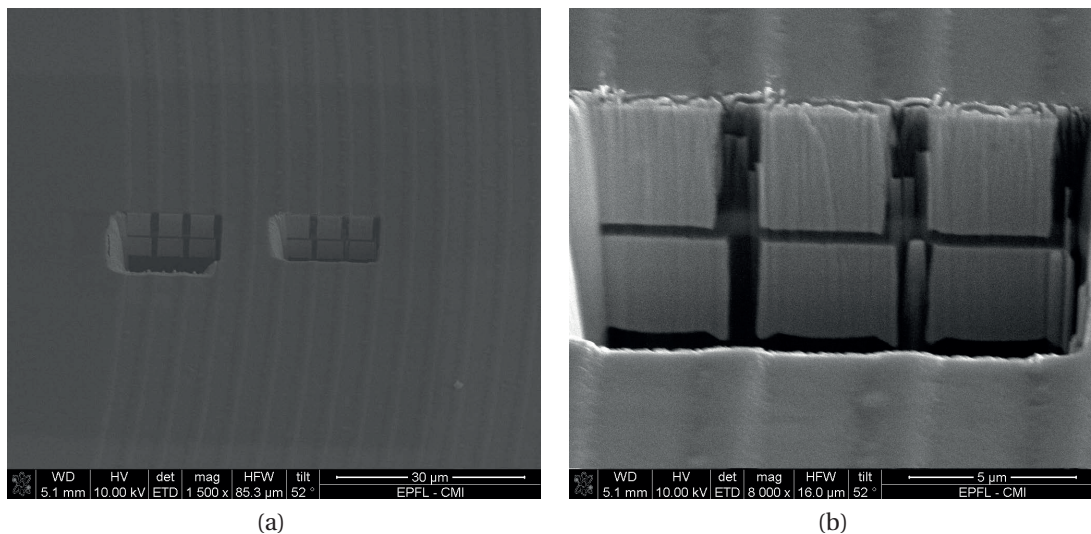


Figure 5.19 – Protective SiO_2 layer: (a) aerial view and (b) FIB cross section.

Once the oxide has been etched in correspondence of the connecting pads, an additional 1 μm of SiO_2 is sputtered on the surface. The usefulness of the double oxide layer will be clarified shortly.

Step (d)

This step defines the outer layout and the central hole of the stator and consists in the deep etching of all the materials until the silicon substrate is reached. This is done by using a sequence of plasmas whose chemical composition depends on the material to be etched (CF_4 for SiO_2 , O_2 for PI, Cl_2/BCl_3 for Al). In this sense, two key points, are ensuring the compatibility between plasma and the exposed substrate and optimizing the thicknesses of masking materials. An efficient solution for pursuing these objectives was to pattern 14 μm of photoresist first. Although involved plasmas are not selective with respect to photoresist (targeted materials are attacked at the same rate), the high thickness allows to etch safely the first 3 μm of protective oxide,

the 4.5 μm of polyimide of the second level coils and the 2 μm of insulating oxide. On the other hand, the photoresist will be completely vanished at approximately half way through the etch of the first level polyimide. At this point, about 5 μm of PI have yet to be etched while the SiO_2 on top is exposed to plasma. Such scenario does not present any issue since, as discussed in section 4.3.2, the O_2 plasma is highly selective with respect to SiO_2 . The step can thus be pursued to the end without compromising the protective layer at all. Finally, the adhesion layer can also be etched without problems regardless of whether it is Al or SiO_2 , since the thickness (150 nm) is far smaller with respect to the protective layer, whose thinning is therefore negligible. One should notice that this is also true in correspondence of the connection pads, which at this stage are covered by 1 μm of SiO_2 . It should be noted that this step is more complicated in the case of a 4 layers stator, since additional 4 μm of SiO_2 and 9 μm of PI have to be etched. A straightforward solution is to increase the thickness of the photoresist layer up to about 30 μm . This can be done with relative ease, considering that the features to be patterned are of the order of hundreds of microns.

Steps (e)

At this point, the original concept included to separate the the coils from the silicon substrate by dissolving the Al adhesion layer. For this purpose, several techniques were tested, including standard wet etching using an acid solution (a mixture of acetic, nitric and phosphoric acid) to attack Al and electro-etching in a sodium chloride solution. Both approaches however turned ineffective. A first problem is that the etching rates are in the order of hundreds of nm per minute. This translated into wet treatments of several hours, which is both impractical and dysfunctional for the other materials involved. Moreover, liberated stators floating in the etching solution are difficult to manipulate, which in turn complicates any additional treatment (*e.g.* rinsing). Finally, completed devices resulted severely deformed, most likely due to the internal stress of the oxide layers, which was no longer balanced by the supporting substrate. For these reasons, a different strategy, based on a Dicing Before Grinding (DBG) philosophy was conceived and implemented. DBG is a variation of simple dicing, whose principle is schematized in Figure 5.20. The wafer is only partially diced and a tape is applied on the surface. Then, an abrasive disk is used in order to grind the back side of the wafer until the dicing lines on the front side are reached. Finally, an UV treatment allows to reduce the adhesion of the tape, so that the chips can be separated.

The wafer was therefore submitted to an additional treatment in order to etch the silicon substrate. This was done with relative ease using Deep Reactive Ion Etching (DRIE), and in particular, a Bosch process. The latter represents nowadays a well established technique for Si etching and consists of alternating standard etching steps (based on SF_6 plasma) to the deposition of an inert passivation layer (C_4F_8). The technique allows to etch silicon with a terrific degree of anisotropy at the expense of

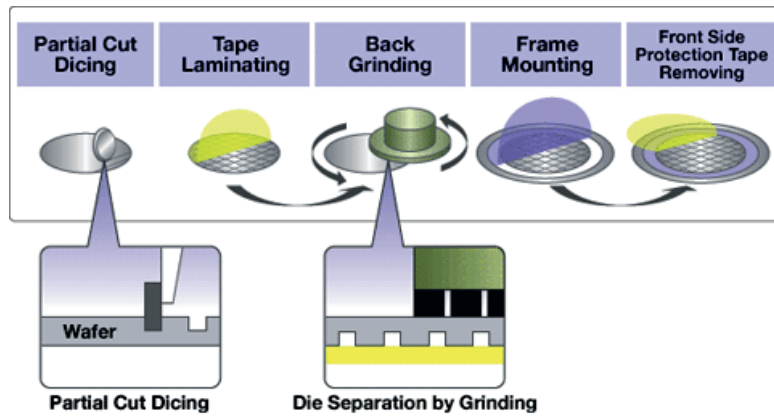


Figure 5.20 – Principle of Dicing Before Grinding (source: <https://www.disco.co.jp/>).

an increased roughness of the lateral surfaces (which has no impact for the present application). Another significant advantage is that the SF_6 plasma is highly selective with respect to SiO_2 ($> 200 : 1$), so that the protective layer on top of the stator allows to etch silicon up to hundreds of micrometers. It should be noted that the etching depth coincides with the final thickness of the supporting substrate, so that an insufficient etch depth will result in brittle devices. In this sense, it was found that a minimum of $60 \mu\text{m}$ are needed in order to ensure the overall functionality of the stators, although $90 - 100 \mu\text{m}$ are a fair compromise for enabling effortless manipulation of the devices. The results can be observed in Figure 5.21.

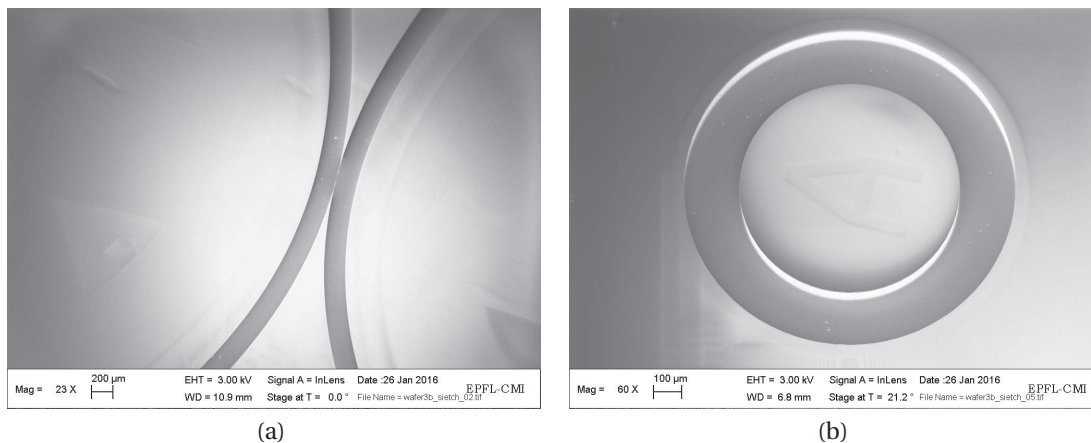


Figure 5.21 – Completed stators after Si etch: (a) borders and (b) center.

Steps (f)-(g)

The final step of the process consists of exposing the substrate to a CF_4 plasma with the aim of dissolving one micron of oxide in order to free the connection pads. This is done without using any masking materials. In fact, a lithographic step is no longer feasible

since the substrate is far from being planar. The consequence is that both the pads and the protective layer are attacked. However, since the oxide layer on the pad is thinner (*cf.* steps (b)-(c)), the electrical contact can be restored before the protection layer is completely vanished. On top of that, any byproduct associated with the interaction between the plasma and the exposed silicon, is basically irrelevant since it will be ground away. The grinding is then performed as described in the previous paragraph. After the abrasion of the silicon substrate, the devices can be individually separated from the tape. It is important to extend the UV treatment, since the adhesion force with the stator is significant. As for example, without the protective SiO₂ layer, copper is likely to be peeled off the PI mold at this point. Figure 5.22 shows completed stators from two different batches after liberation from the substrate. The specimen on the left makes use of SiO₂ as adhesion layer between the silicon substrate and the first layer of PI. Since SiO₂ is basically transparent, the silicon substrate confers a bluish vibe to the stator. On the other hand, the stator on the right has the adhesion layer in aluminum, which reflects light and makes it more brilliant. The measured thickness was equal to 80 μm for the stator on the left and 120 μm for the one on the right.



Figure 5.22 – Completed stators with adhesion layers in SiO₂ (left) and Al (right).

In total, 37 stators could be fabricated, 26 of which with SiO₂ as adhesion layer and a thickness of 80 μm and 11 with Al and a thickness of 120 μm. The measured resistance averages at 12.8 kΩ. It is worth mentioning that 100% of the stators that were functional after the completion of the second layer were also found functional after their liberation, which demonstrates the reliability of the proposed method.

5.4 Assembly and Measurements

After liberation, the stator had to be assembled into the watch movement. Such operation was performed outside the clean room environment and because of contingent constraints, it offered comparatively little space for optimization. Next sections will

present the main steps and discuss the electrical measurements.

5.4.1 Flexible PCB

In the first phase, the stator is glued to a flexible PCB, whose role is basically enabling an electrical connection once the generator is integrated into the gearing. The PCB includes holes in correspondence of the connection pads, so that the joining between the parts is achieved by aligning and filling the gaps with conductive glue. The ensemble is then submitted to a mild thermal treatment in order to speed up drying. The result can be observed in Figure 5.23.

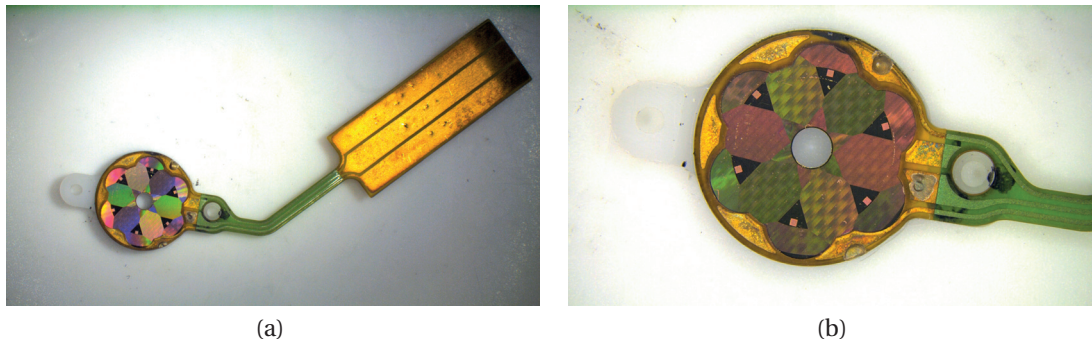


Figure 5.23 – Stator glued to flexible PCB: (a) complete view and (b) detail.

The operation is performed completely manually, which makes it problematic at different levels. As for example, the alignment between the PCB holes and the stator pads is done in a relative rough manner without any precise reference. Also, the joining relies entirely on the adhesion force provided by the conductive glue, which in turn needs to dry out before becoming mechanically (and electrically) effective. This may cause misalignment as well as dispersion of conductive glue on the wafer surface. In practice, multiple functional stators were damaged in the process, with electrical measurements performed after the PCB application showing unacceptable resistance values or no electrical contact at all. In practice, only one stator could be effectively mounted. In particular, the resistance measured before assembly was equal to 13.8 k Ω . This value only partially matched the measurement on the PCB, which was found equal to 11.7 k Ω . The causes that led to this result could not be investigated. A fair possibility is that the resistance drop might be caused by stray drops of conductive glue penetrated below the oxide protective layer causing local short circuits. Nevertheless, since the drop is not dramatic it was still decided to pursue the assembly, even though a performance drop was expected.

5.4.2 Rotor

The following step is to couple the stator with the rotor in order to form the generator and subsequently mounting it into the watch movement. As discussed in Chapter 3, the rotor that was taken into account for the stator optimization comprised 2 ferromagnetic yokes, each one coupled to a commercially available NdFeB magnet and an air gap of $200\ \mu\text{m}$. However, the apparatus that was provided for testing has different features, mainly because it was adapted from another application. In particular, while the magnet and the yoke match their geometric and magnetic parameters, the air gap is equal to $540\ \mu\text{m}$. Moreover, an additional magnet is installed on one of the yokes. A scheme is reported in Figure 5.24.

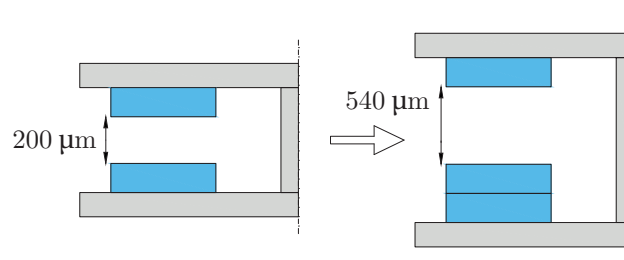


Figure 5.24 – Rotor configuration: (left) model version and (right) prototype version.

Some FEM simulations were launched in order to assess the impact of the rotor modifications on the overall performances of the device. The results were highly coherent with the ones obtained for the original rotor, the new theoretical phase constant being equal to $0.0050\ \text{V}\cdot\text{s}$ instead of $0.0055\ \text{V}\cdot\text{s}$. The reason is that what is lost in terms of induction due to the increased air gap, is compensated by the additional magnet. In this sense, even though the prototype is bulkier, the adapted rotor represents an interesting and cost effective testing tool. Figure 5.25 shows the generator assembled into the watch movement.

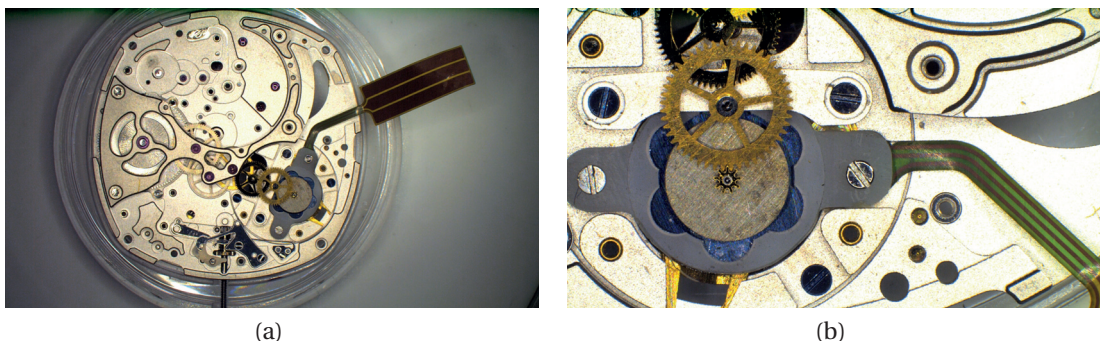


Figure 5.25 – Generator assembled into the watch movement: (a) complete view and (b) detail.

5.4.3 Induced voltage

After the assembly, the watch gearing can be put into motion by turning the winding pinion. Being mechanically linked to the rest of the movement, the rotor is also put into rotation as a result. This allowed to measure the induced voltage in open circuit conditions by simply branching an oscilloscope to the PCB terminals. Figure 5.26 reports an example of the raw signal with its associated fundamental harmonic, obtained by mean of a simple spectral analysis. As can be observed, aside from some high frequency noise, which is inherent to the measurement, the signal is effectively reconstructed without using harmonics of higher order.

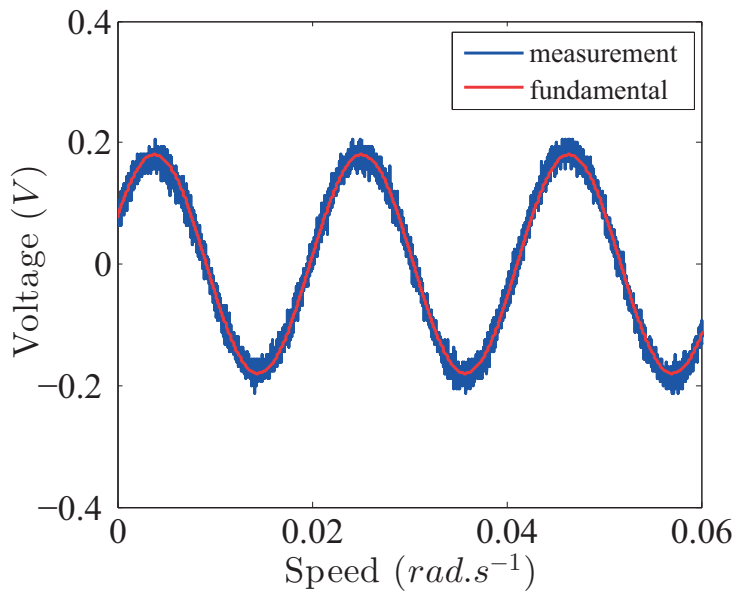


Figure 5.26 – Example of induced voltage measurement.

In order to estimate the phase constant, a series of measurements were performed with the aim of linking the rotor speed to the peak value of the induced voltage. The rotor speed was therefore varied by turning the winding pinion at different levels. It should be noted that this is possible because the assembly does not provide a traditional escapement nor the electronic command necessary for guaranteeing a steady pace of the gearing. As a result, if the barrel (*cf.* Figure 1.3) is armed, it will discharge quasi instantaneously. Also, more energy introduced in the barrel results in higher speed of the gearing. After having acquired several signal of the type reported in Figure 5.26, some post processing was performed. In particular, extensive use of the Savitzky–Golay filter was made in order to smooth the signal and retrieve the peak values of the EMF. The speed was instead obtained by analyzing the electrical pulsation ω_{el} of the signal, which is known (*cf.* Chapter 2) to be proportional to the mechanical speed through the number of magnetic pole pairs p . The results are reported in Figure 5.27.

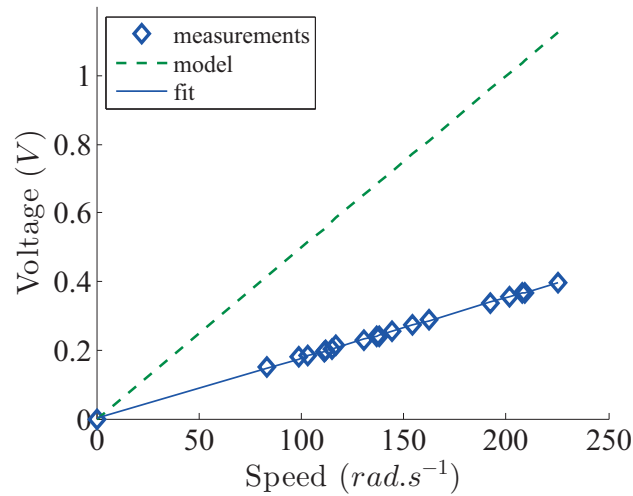


Figure 5.27 – Phase constant extrapolation from back EMF measurements.

As can be observed, the measured values are below the theoretical predictions. In fact, the phase constant obtained from the measurements is equal to 0.0017 V.s, while the theoretical value is 0.0050 V.s. Since the FEM model was even experimentally validated (*cf.* section 2.4), several conjectures were formulated in order to explain such result. A first explanation are the defects induced on the stator during the gluing of the flexible PCB. However, even though the presence of such flaws is attested, it is also true that the resistance variation is too small to explain the discrepancy between the theoretical and measured values of the phase constant. Another possibility that was investigated, is the severe demagnetization of one or more rotor magnets. Since the prototype could not be disassembled, direct measurements in this sense could not be performed. However, induction measurements using a Hall probe on magnets from the same manufacturer showed values coherent with FEM simulations. While these tests are clearly not exhaustive and do not allow to exclude the starting hypotheses, they still suggest that a degradation of magnetic properties of such entity is unlikely to occur. The effect of some originally underestimated parasitic phenomena, it is not a convincing alternative either, considering that the induced voltage increases linearly with the speed and such trend is not affected by frequency. Another possibility that was extensively investigated, is a misalignment between the magnets. This conjecture is motivated by the fact that the while one rotor yoke is actually bolted to the shaft, the other one is held in position using the magnetic forces exclusively. However, these are predominantly axial rather than tangential, which may cause a sort of dragging effect during the rotor spinning motion and thus the loss of the perfect alignment between the magnets. This would actually cause a diminution of the induction field magnitude in the air gap, which results in poorer flux linkage between the magnets and the coils. In fact, magnetic coupling reaches its maximum when magnetic poles on each side of the stator are perfectly aligned, while the lowest value (virtually zero for symmetric systems) is attained when magnetic poles are completely opposed (60° in the present

case). Figure 5.28 exemplifies this concept by showing the magnetic induction in the middle of the air gap for perfect alignment (0°), complete misalignment (60°) and the intermediate value of 40° . The induction was evaluated using FEM over a circular line whose diameter is coincident with the average diameter of the magnet.

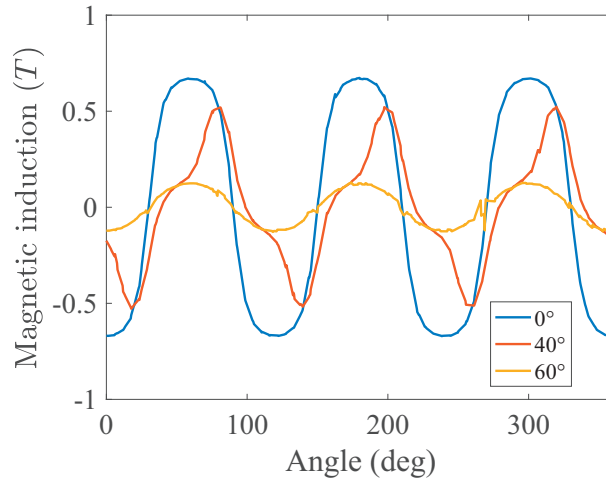


Figure 5.28 – Magnetic induction in the air gap for three different misalignment values (FEM).

From a quantitative point of view, a misalignment of 40° could actually explain the performance drop measured above. It is also worth noticing that the less regular shape of the induction in the air gap does not affect the quality of the output signal. Figure 5.29 shows for such misalignment, the actual flux linkage with a coil sector as a function of the rotor angular displacement. As can be observed, the trend remains purely sinusoidal and no higher order harmonics are introduced. In conclusion, the dragging effect seems a promising lead, nevertheless the analysis cannot be concluded without performing additional tests on the movement. Unfortunately, this was not possible since it would have required significant manipulation of the components and thus specialized personnel for this purpose.

5.4.4 Comparison with previous work

Table 5.2 provides a bit of context by comparing the findings in terms of phase constant with previously presented devices, comparable for size and layout. As can be observed, despite the discrepancy with expectations, the phase constant is still significantly higher, one to several orders of magnitude, with respect to the other considered machines. Fairness imposes however to clarify that the comparison only takes into account the phase constant, which is quite limiting considering the variety of applications for which each device was conceived. For example, the generator developed here has a resistance of $11.7 \text{ k}\Omega$ against values below 15Ω in the other cases. In this

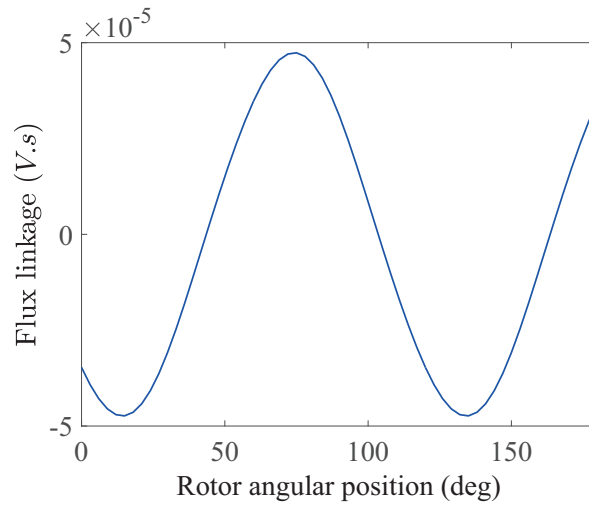


Figure 5.29 – Flux linkage as a function of the rotor angular position for a 40° misalignment between the magnets.

sense, it is more suitable for applications requiring high output voltages rather than high efficiency.

Table 5.2 – Phase constant comparison with previously published works

Reference	configuration	k_{ph} (V.s)
[MKP11]	three-phase	$3.8 \cdot 10^{-5}$
[DAZ ⁺ 05]	three-phase	$1.0 \cdot 10^{-4}$
[HJA08]	three-phase	$4.0 \cdot 10^{-6}$
This work	single-phase	$1.7 \cdot 10^{-3}$

5.5 Summary and conclusions

This chapter addressed the fabrication and the characterization of the MEMS generator designed in Chapter 3. On the basis of the results obtained in the context of the pilot study in Chapter 4, the most feasible stator configuration was selected. The latter consists of 4 layers of copper coils, with a nominal width of 3 μm, a spacing of 2 μm and a total of 159 turns for each sector. In order to simplify the prototyping and demonstrate the process, it was chosen to limit the layers to 2.

Although the copper process had already been used for the manufacturing of single layer coils, some modifications in terms of layout were needed in order to enable its upgrade for the fabrication of multilayer structures. As for example, some patterns were introduced on larger features (*e.g.* the connecting pads) in order to deal with non planarities originated during electroplating. Moreover, the disposition of the devices

Chapter 5. MEMS generator prototyping

on the wafer surface was discussed.

Electrical characterizations on the first layer showed a success rate of 85%, which *a priori* is sufficient to enable the fabrication of stators with 4 levels of copper. Multiple steps were then added to the original process flow. In this sense, a technique for the fabrication of the insulating layer, was presented. After the fabrication of the second layers coils, a hybrid technique based on plasma etching and inspired by Dicing Before Grinding, was employed for the liberation of the stators from the substrate. In total, 37 functional stators were fabricated. Among these, 26 include an adhesion layer in SiO₂ and a thickness of about 80 μm, while the rest of the devices has an adhesion layer in Al and a total thickness of 120 μm. Finally, the steps for the assembly of the stator and the rotor, as well as the implementation into the watch movement were presented.

The induced voltage was measured at different speeds in order to determine the phase constant of the generator. The resulting value is equal to 0.0017 V.s, far below the theoretical prediction of 0.0050 V.s. Several conjectures aiming to explain the discrepancy were made. A plausible hypothesis in this sense, compatible with the results obtained through a dedicated FEM study, concerns the possibility of a misalignment between the upper and lower magnet when the rotor is put into motion. Despite the discrepancy with expectations, the phase constant is still significantly higher, one to several orders of magnitude, with respect to previously published comparable devices.

The results presented throughout this chapter bring answers at different levels and assess the effectiveness of the process flow for the fabrication of the generator, from the blank wafer to the implementation into the watch movement.

Publications related to this chapter:

- J. Poliakine, J. C. Fiaccabrino, J. Zürcher, Y. Civet, Y. Perriard, *Microgénératrice pour pièce d'horlogerie et procédé de fabrication de microgénératrice pour pièce d'horlogerie*, European patent, 17174542.5 - 1559.

6 Conclusions and perspectives

This thesis has addressed the modeling and the fabrication of a MEMS generator for the regulation of a mechanical watch.

As it has been highlighted in the introductory chapter, rather than focusing on the specific application, the subject was approached from a more general perspective. This was done both for the theoretical aspects and for the technological development. The first step in this sense, was to derive a comprehensive electromechanical model by engrafting a very broad definition of synchronous machine on Hamilton's principle. Then, the focus was put on how size reduction affects the construction parameters appearing in the model. The trends that were determined allowed to calibrate the evolution equations of dynamics for the description of MEMS machines, thus providing some general design guidelines. A practical application was also shown, and some strategies for the evaluation of the significant variables were experimentally validated.

Once the theoretical and technological frame was defined, the watchmaking application was considered. The technical requirements were discussed and, on such basis, an axial flux generator, comprising planar coils and two rotor yokes coupled to multipole ring shaped magnets, was designated as the most suitable solution. In this context, the electromechanical model previously derived was used extensively in order to simulate the working conditions. This allowed to compare single and three phase configurations and deduce additional functional constraints that were not explicitly declared. The actual dimensioning of the device was pursued by making use of an optimization routine that was conceived with the aim of taking into account both functional and technological constraints. Additional information was however needed in order to operate a finer selection between the configurations identified by the routine.

This necessity triggered a study on modeling and manufacturing of single layer planar coils. These were considered as independent components, whose domain of application is therefore not limited to power generation in MEMS machines. Within this framework, two process flows, based on aluminum and copper respectively, were

optimized with the aim of reducing the interwinding distance without compromising the conductor section. Electrical measurements on the completed coils are highly coherent with theoretical predictions. Furthermore, morphological characterizations allowed to put in evidence several key aspects of the proposed manufacturing approaches. While the results obtained within this nested research have standalone significance, they also provided the technological knowledge required to operate a final choice between the MEMS generator configurations.

The retained solution is based on the copper process, which however needed to be upgraded in order to allow the manufacturing of multilayer structures. Several modifications in terms of layout were therefore introduced. Moreover, a significant number of steps were added to the original fabrication flow. These include the structuration of the insulating layer between the copper levels as well as the liberation of the stators from the silicon substrate. Finally, one specimen was selected out of 37 functional stators and implemented in the watch movement. The generator was then characterized in terms of induced voltage. Several conjectures were formulated and analyzed in order to interpret the discrepancy between measurements and theoretical predictions. Besides this aspect, the results showed a phase constant among the highest reported for similar devices.

6.1 Original contributions

The research conducted throughout this thesis work is related to different topics, from purely theoretical to technological. The main contributions can be summarized as below.

- *Electromechanical model for synchronous devices*

The model has been developed in order to provide a comprehensive description of synchronous machines. While time dependent models for the study of electrical machines are not new to the field (although their use is relatively limited), the one presented here has a very general character, as it includes a variety of static and dynamic reluctant effect. The significance does not reside however in the system of equation per se, but rather in its versatility. In fact, it can be used as a main frame in which complex analytic formulas and finer models can be easily implemented. Moreover, it proved its efficiency as a powerful simulation tool, for applications in which conditions and parameters are dynamically varied during operation, as it was demonstrated in Chapter 3.

- *Planar coils with high inductance density*

The planar coils presented in Chapter 4 represent a significant contribution to the state of art. The proposed technological approaches allowed to reach

inductance densities up to several orders of magnitude higher with respect to components with similar layouts and comparable to inductors fabricated using more complex and less scalable processes. The proposed coils are particularly suitable for applications where high inductive properties are required rather than high quality factors, an example being proximity sensors. Within this framework, the key aspects of two manufacturing techniques of common use were analyzed and some guidelines for the choice of the most suitable process were identified for the benefit of future designers.

- *Process flow for manufacturing of multilayer structures*

The process was developed and optimized for the purpose of manufacturing the generator's stator. Multilayer coils per se cannot be considered as new in the domain of MEMS, nevertheless the process presented in this thesis is valuable in different ways. A first fundamental aspect is that it allows the fabrication of highly packed patterns with relatively large conductor sections on every layer. In fact, high pattern densities are usually obtained at the expense of the conductor thickness. Alternatively, thick conductors are actually fabricated, but pattern complexity is limited to one layer only. For example, in many planar inductors the first level only provides a thin conductive track in order to retrieve the contact from the center of the component. Another key point, is the success rate of coils on each layer, which makes the overall process scalable and virtually suitable for the fabrication of even additional copper levels. Finally, its applicability is not necessary limited to the manufacturing of coils. Instead, the proposed approach can be used whenever a dense conductor network is needed. Also, some steps can be extracted and adapted to different purposes, an example being the trenching of the polyimide mold for microfluidic applications.

- *Generator with high phase constant*

Other than the theoretical aspects and the technological efforts dedicated to its development, the generator itself represents an advancement in the context of power generation at small scale. In fact, electromagnetic devices tend to have low output voltages and high rotational speeds are usually required in order to generate back EMF with a magnitude suitable for practical applications. In this sense, the generator designed in this thesis allows to reach such objective at relatively low speeds, thanks to its high phase constant. This is a significant advantage even for applications other than the electronic escapement discussed here. As for example, a high phase constant translates into higher sensibility in velocity sensing applications.

Other minor contributions can be identified. The approach used in Chapter 3 for the definition of the objective function and its associated optimization strategy has a general character and can be employed for designing generators for applications beyond

the watchmaking one presented here. Also, several strategies that were implemented during clean room prototyping were actually quite creative. As for example, using IBE for wafer cleaning after CMP is an effective approach which, unlike common methods based on soft polishing pads, does not require significant optimization. The patterning of the connection pads is also a valid method for reducing non uniformity problems during electroplating and can be employed in any process including such step. Sparks of originality can also be found at a design level. For instance, the connection scheme used for the stator coils allows to reduce the number of VIAs as well as the overall process steps, considering that all connections are automatically defined once the second level coils are completed.

6.2 Outlook

The research conducted so far can be pursued and completed at different levels, including purely theoretical as well as experimental aspect. Some interesting areas of investigation in this sense are summarized below.

- *Thermo-electromechanical model*

Because of the low magnitude of the currents involved in the application, thermal effects were not addressed directly. The subject is however relevant for electrical machines in the wide majority of applications. In these cases, thermal effects are usually addressed separately with respect to the electrical and mechanical parts of the system. In this sense, the electromechanical model presented in Chapter 2 could be enhanced by introducing additional degrees of freedom for the description of heating phenomena. In line of principle, this could be achieved by introducing thermal energies in the expression of Hamilton's principle.

- *Magnetic materials*

Another perspective that was opened concerns the implementation of magnetic materials, in order to enhance the performances of the presented components. In fact, self inductance, as well as magnetic coupling with other elements like permanent magnets, could be largely improved by combining the pattern densities achieved with the technological approaches presented in this work, with the use of magnetic materials in order to create high permeance magnetic paths.

- *Miniaturization*

A key point of the processes presented here, is the high density of conductor lines. In line of principle, this approach could be pushed further in order to fabricate even smaller and narrower conductor lines. From a lithographic point of view, further size reduction is not problematic, considering that next-generation techniques (either mature or undergoing intense development), such as x-ray,

e-beam or extreme UV lithography, allow the patterning of features in the order of tens of nanometers [Sil98, Che15, FC16]. However, obtaining conductor lines with low resistance becomes more complicated. In fact, higher resolutions are normally obtained at the expense of the photoresist layer thickness, thus limiting its effectiveness as a masking material and ultimately leading to smaller conductor sections. The issue could partially be addressed by using x-ray lithography, since the x-rays used for the exposure are relatively insensitive to resist thickness. Even so, the lateral overetch effect discussed in Chapter 4 will still prevent the same geometry to be transferred 1:1 to the actual conductor lines. The improvement of the etching technique performances should therefore be a main focus in order to pursue further miniaturization.

- *Electronic escapement*

Because this work has been largely inspired by an industrial project, it is worth discussing the enhancements required in order to enable the prototype to work as an escapement system. The MEMS generator presented comprises only 2 layers of copper instead of the 4 required. As a consequence, in order to drive the electronic command, a speed higher than the 33.5 rad.s^{-1} fixed by the technical requirements would be needed. If such compromise is not acceptable, electrical measurements pursued throughout the prototyping showed clearly that the coils success rate on each layer is sufficient to virtually allow the fabrication of stators with 4 copper levels. However, the number of fabrication steps, which is already high, would increase significantly. A particular effort should therefore be dedicated to ensure the repeatability of each step, in particular by enacting a strict control of the working environment with the aim of minimizing aleatory errors that could harm the specimens. An attractive alternative that could allow to overcome such issue, would be evolving the process in order to fabricate modular stators with 1 or 2 layers, that could later be stacked together according to the particular application. Finally, in the long term, printing technologies are a promising method that might replace the clean room development, with consequent benefits in terms of costs and versatility.

A Proximity effects in MEMS conductor

Proximity effects are caused by the interaction between the magnetic fields generated by adjacent current carrying conductors. The effect causes the current to be non-uniform over the conductor section, thus leading to an overall increase of the resistance. This phenomenon is absent at DC and becomes more and more important as the frequency increases. As a general rule (see for example [Ste06]), proximity effects are promoted by large sections as well as small spacing between conductors. MEMS synchronous machines usually operate in a range of frequencies from a few Hz to several kHz (rotational speed $\sim 1 \cdot 10^5 rpm$), while conductors have square or rectangular sections with widths and spacings up to tens of microns. While all the models of common use for the description of such effect are unanimous in predicting no significant proximity effects under such operating conditions, an empirical verification can be done using FEM. Figure A.1 shows some simulations run at different frequencies for a typical MEMS configuration, comprising an array of 5×5 square conductors with a width of $20 \mu m$ and a spacing of $2 \mu m$.

As can be observed, at 10 kHz, which can be assumed as an upper limit for MEMS synchronous machines, the current is still uniform on the section. For the given system, non-uniformity becomes significant above 1 MHz and severe at 1 GHz.

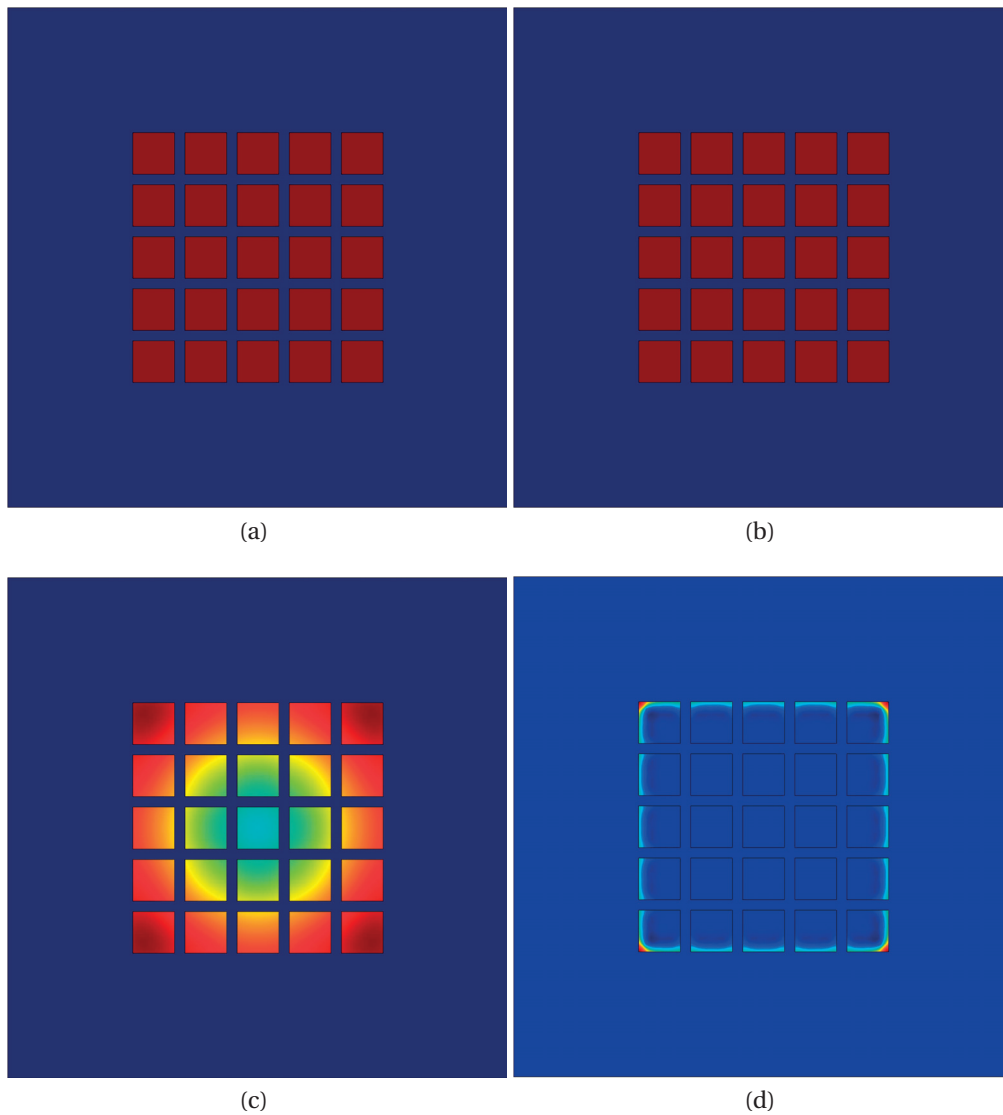


Figure A.1 – Effect of frequency on current distribution: (a) DC , (b) 10 kHz, (c) 5 MHz, (d) 1 GHz.

B Single and double yoke configuration - Field lines distribution

Figure B.1 shows the distribution of the magnetic induction field for two generator configurations comprising one and two rotor yokes. Although only a cross section of the generator is shown for readability reasons, original FEM simulations were run in 3D, taking into account all of the generator geometry.

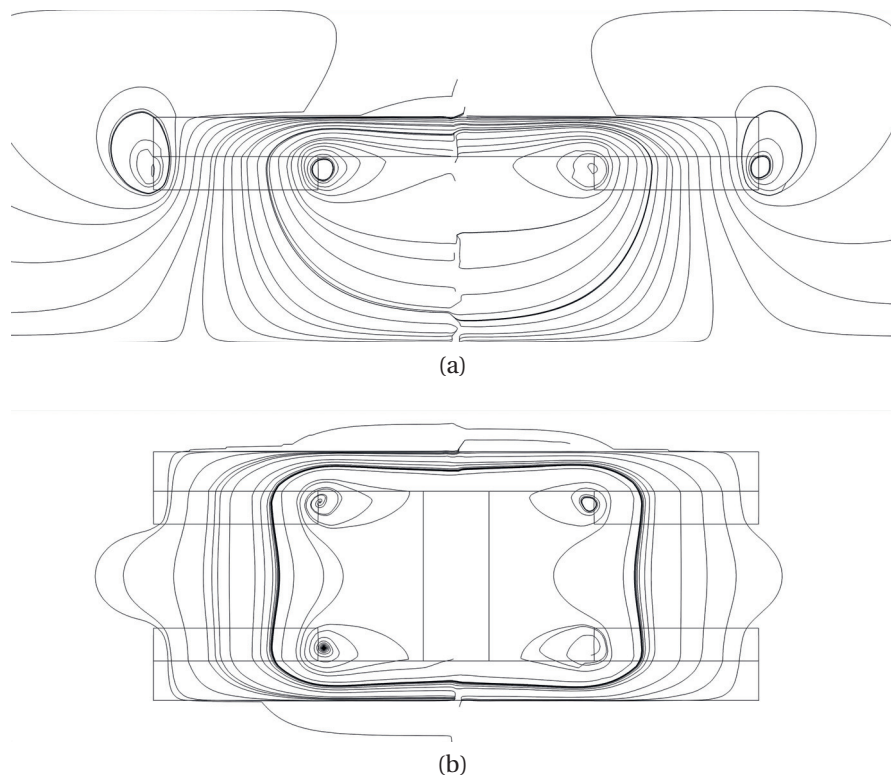


Figure B.1 – Distribution of the induction field for two axial flux generator configurations: (a) single yoke and (b) double yoke.

As can be observed in, in the single yoke configuration a significant part of the magnetic field is unconstrained (Figure B.1(a)). This represent a risk, since the coupling of

Appendix B. Single and double yoke configuration - Field lines distribution

stray field lines with high permeance materials in the environment might result in parasitic forces and torques that are likely to compromise the functionality of the device. The introduction of a second rotor yoke, as in Figure B.1(a)) allows to overcome this issue, since the induction field is basically confined around a small region around the generator. It is also worth noticing that the presence of the rotor shaft does not affect the streamlines distribution. This can be plainly explained by analyzing the symmetry of the system.

C Equivalent magnetic circuit

The impact of several construction parameters can be assessed *a priori* with quite limited modeling effort. Let's consider the double yoke generator of Figure C.1.

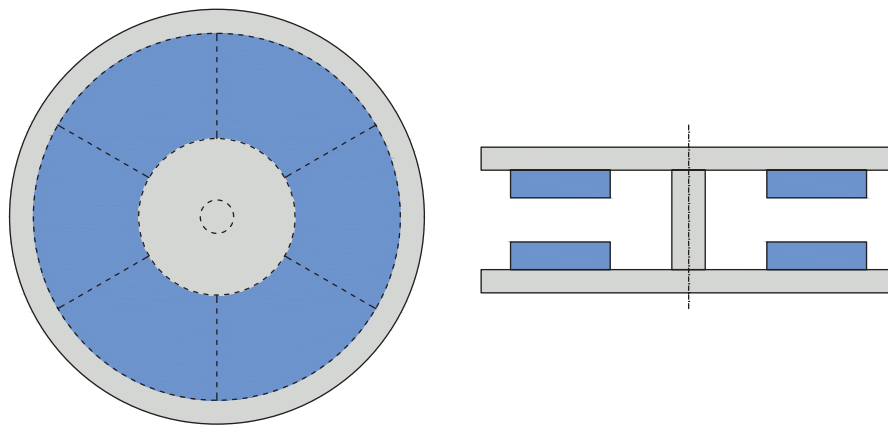


Figure C.1 – Upper view and cross section of a double yoke generator

Because of the symmetries of the system, describing the behavior of two opposing magnetic poles is enough to basically represent the whole system. The simplified magnetic magnetic circuit of Figure C.2, allows to fulfill such task.

The meaning of the terms appearing in the magnetic circuit is as follows. Θ_m is magnetomotive force associate to one magnet pole. The other terms are all permeances. In particular, P_{ry} is the permeance associated to one half of the ferromagnetic yoke length, Λ_{sh} represents the rotor shaft, Λ_δ the air gap and Λ_m the inner permeance of one magnet pole. The terms Λ_{il} and Λ_{el} represent the inner and outer permeances associated with magnetic field leakage at the borders of the air gap. Since the purpose of the circuit is just to estimate the impact of certain construction parameters, they can be neglected, however this operation is definitely not legit for quantitative studies. Following the same principle, for the calculation of the associated permeances it will also be assumed that the surfaces of the magnet S_m and the air gap S_δ , are coincident.

Appendix C. Equivalent magnetic circuit

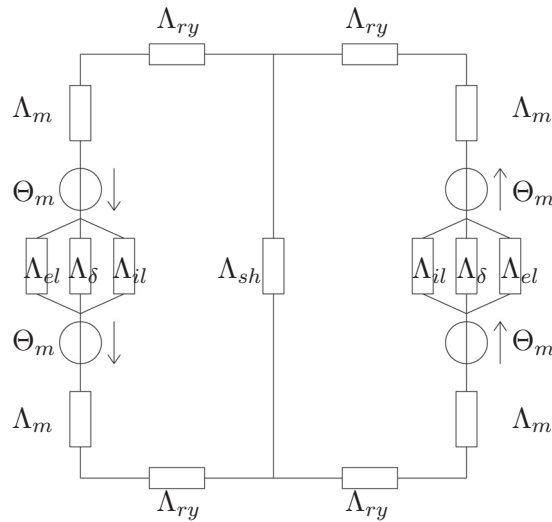


Figure C.2 – Equivalent magnetic circuit.

Since the left and right vertical branches of the circuit are mirrored, no magnetic potential is generated at the terminals of Λ_{sh} and no flux (see also Appendix B) is found here. The circuit is thus reduced to one magnetic loop, described in Figure C.3.

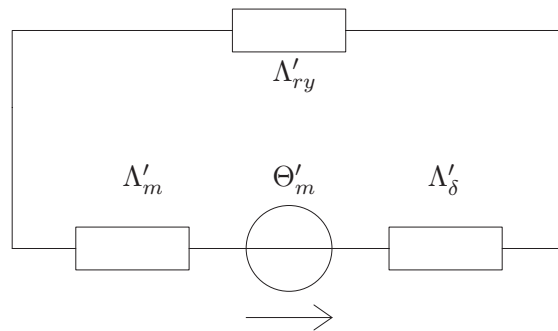


Figure C.3 – Simplified magnetic circuit (I).

The terms Θ'_m , Λ'_m , Λ'_δ and Λ'_{ry} represent the total contributions for the magnet, the air gaps and the rotor yoke segments. In particular, the series of the 4 magnetomotive forces exerted by the magnets can be expressed as [Juf95]

$$\Theta'_m = 4\Theta_m = 4 \frac{B_0}{\mu_m \mu_0} h_m \quad (\text{C.1})$$

where, B_0 is the residual flux density, μ_m is the relative permeability of the magnet, μ_0 is the vacuum permeability and h_m the magnet thickness. The other permeances can

be obtained using the definition (2.40).

$$\Lambda'_m = \frac{\mu_m \mu_0 S_m}{4h_m} \quad (\text{C.2})$$

$$\Lambda'_\delta = \frac{\mu_0 S_\delta}{2h_t} \quad (\text{C.3})$$

$$\Lambda'_{ry} = \frac{\mu_{iron} \mu_0 S_{ry}}{4r_{em}} \quad (\text{C.4})$$

Where h_t is the air gap length, μ_{iron} is the relative permeability of the yoke ferromagnetic material, and r_{em} is the outer radius of the magnet. The three permeances can be arranged in series as

$$\frac{1}{\Lambda_{tot}} = \frac{1}{\Lambda'_m} + \frac{1}{\Lambda'_\delta} + \frac{1}{\Lambda'_{ry}} \quad (\text{C.5})$$

It should be noted that the permeability of iron μ_{iron} is several orders of magnitude higher with respect to the μ_0 and μ_m . As a consequence, unless the rotor yoke is disproportionately thin, the third term in equation (C.5) is negligible. In this sense, the rotor yoke thickness is not a parameter worth optimizing, as it has very limited impact on the overall performances of the device. The circuit can finally be reduced to the one reported in Figure C.4.

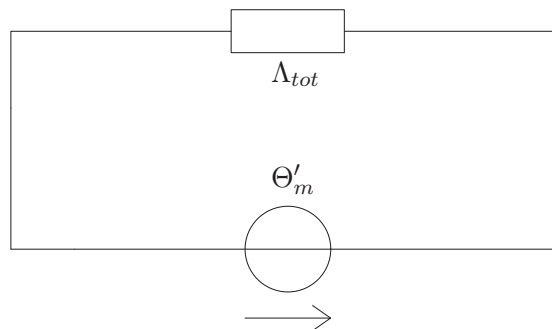


Figure C.4 – Simplified magnetic circuit (II).

At this point, the magnetic flux in the air gap, which is directly related to the magnetic

Appendix C. Equivalent magnetic circuit

coupling between rotor and stator, can be calculated easily using Hopkinson's law (2.39):

$$\psi = \Theta'_m \Lambda_{tot} = \frac{B_0 S_m}{1 + \mu_m \frac{h_t}{h_m}} \quad (\text{C.6})$$

As can be observed from equation (C.6), for the same air gap, thicker magnets will enhance the magnetic coupling. However, since the magnet is commercially available, the control of the designer over such parameter is limited. At the same time, increasing the air gap results in a weakening of the magnetic coupling.

Nomenclature

Acronyms

Symbol	Description
CMP	Chemical mechanical polishing
DBG	Dicing before grinding
DOF	Degree(s) of freedom
EMF	Electromotive force
FEM	Finite element method
IBE	Ion beam etching
ICP	Inductive coupled plasma
ID	Inductance Density
IRR	Inductance to resistance ratio
MEMS	Micro electro-mechanical system(s)
VID	Volumic inductance Density

List of Symbols

Symbol	Description	Units
ϵ	Security tolerance	m
μ_0	Permeability of vacuum	H.m ⁻¹
μ_m	Relative permeability of magnet	-
μ_{iron}	Relative permeability of iron	-

Nomenclature

ϕ	Reduced scalar potential	A
\vec{r}	Spatial vector	
H_0	Magnetic field generated by current sources	A.m ⁻¹
H_m	Reduced magnetic field	A.m ⁻¹
i, j	Priority coefficients	-
S	Conductor section	m ²
ϑ	Rotor angular position	rad
B	Magnetic induction field	T
B_0	Residual flux density	T
β	Viscous friction coefficient	N.m.s
q	Electrical charge	C
q_r, q_s, q_t	Phase electrical charge	C
D	Dissipation function	W
d_{avg}	Planar coil average diameter	m
D_{el}	Electrical dissipation function	W
d_{in}	Planar coil inner diameter	m
D_m	Mechanical dissipation function	W
d_{out}	Planar coil outer diameter	m
ψ	Coupled flux	V.s
ξ	Planar coil filling factor	-
Φ	Generic magnetic flux	V.s
ψ_r, ψ_s, ψ_t	Phase coupled flux	V.s
f	Frequency	Hz
F_i^v	Generalized viscous forces	
h_y	Rotor yoke thickness	m
h_m	Magnet thickness	m
t	Turn thickness	m

Nomenclature

h_t	Air gap length	m
I_e	Excitation current	A
J	Rotor moment of inertia	kg.m ²
e	Horizontal encumbrance	m
I	Phase current	A
I_r, I_s, I_t	Phase current	A
Γ	Generalized kinetic energy	J
Γ_{el}	Electrical kinetic energy	J
k	Homothetic scaling factor	-
Γ_m	Mechanical kinetic energy	J
Γ_{mag}	Magnetic kinetic energy	J
k_{ph}	Phase constant	V.s
L_e	Excitation inductance	H
l	Conductor length	m
L	Lagrangian of the system	J
L_i	Phase self inductance (single-phase)	H
γ	Magnetic path length	m
L	Planar coil inductance	H
L_r, L_s, L_t	Phase self inductance	H
w	Turn width	m
l	Turn length	m
M	Mutual inductance	H
M_{rs}, M_{st}, M_{rt}	Mutual inductance between different phases	H
n_l	Number of layers	-
n_s	Number of turns	-
f_{obj}	Objective function	
p	Magnetic pole pairs	-

Nomenclature

Λ_{δ}	Air gap permeance	H
Λ_{sh}	Rotor shaft permeance	H
Λ_e	Equivalent permeance	H
Λ	Generic permeance	H
r, s, t	Phase identifier	
Λ_{el}	External leakage permeance	H
Λ_{il}	Internal leakage permeance	H
Λ_m	Magnet permeance	H
Θ_s	Saturation magnetic potential	A.turn
Θ_e	Excitation magnetic potential	A.turn
Θ	Generic magnetic potential	A.turn
Θ_m	Magnet potential	A.turn
Λ_{ry}	Rotor yoke permeance	H
Q_i	Generalized forces	
q_i	Generalized coordinates	
r_{sh}	Rotor shaft radius	m
r_y	Rotor yoke radius	m
r_{em}	Magnet outer radius	m
ρ	Electrical resistivity	$\Omega.m$
r_{ext}	Stator outer radius	m
R_i	Phase resistance (single-phase)	Ω
r_{im}	Magnet inner radius	m
r_{int}	Stator inner radius	m
R_l	Load resistance	Ω
R_{lr}, R_{ls}, R_{lt}	Phase load resistance	Ω
r_{max}	Stator maximum outer radius	m
R	Planar coil resistance	Ω

Nomenclature

R_r, R_s, R_t	Phase resistance	Ω
δ	Skin depth	m
s	Interturn spacing	m
χ	Spacing to width ratio	-
T_{em}	Electromagnetic torque	N.m
T_{fr}	Dry friction torque	N.m
t	Time	s
T_{in}	Input torque	N.m
T_m	Overall device torque	N.m
Π	Potential Energy	J
U	Applied voltage	V
U_i	Induced voltage	V
U_r, U_s, U_t	Phase applied voltage	V
Ω	Rotor mechanical speed	rad.s ⁻¹
$V.I.$	Variational indicator	
ω_{el}	Electrical pulsation	rad.s ⁻¹
W_{nc}	Work of non-conservative forces	J
x	Optimization variables array	
Y_p	Proximity effect resistance	Ω
Y_s	Skin effect resistance	Ω

Bibliography

- [ACN⁺05] Perez Rodriguez A, Serre C, Fondevilla N, Cereceda C, Morante J R, Esteve J, and Montserrat J. Electromagnetic inertial generator for vibrational energy scavenging compatible with si technology. The 5th international workshop on Micro and Nanotechnology for Power Generation and Energy Conversion Applications, 2005.
- [ADC⁺06] D. P. Arnold, S. Das, F. Cros, I. Zana, M. G. Allen, and J. H. Lang. Magnetic induction machines integrated into bulk-micromachined silicon. *Journal of Microelectromechanical Systems*, 15(2):406–414, April 2006.
- [AKA93] C. H. Ahn, Y. J. Kim, and M. G. Allen. A planar variable reluctance magnetic micromotor with fully integrated stator and coils. *Journal of Microelectromechanical Systems*, 2(4):165–173, Dec 1993.
- [BAZG14] M. R. Baklanov, C. Adelman, L. Zhao, and S. De Gendt. Advanced interconnects: Materials, processing, and reliability. *ECS Journal of Solid State Science and Technology*, 4(1):Y1–Y4, dec 2014.
- [BC07] S. Balac and G. Caloz. The reduced scalar potential in regions with permeable materials: Reasons for loss of accuracy and cancellation. *International Journal of Numerical Modelling: Electronic Networks, Devices and Fields*, 20(4):163–180, 2007.
- [BCST03] J. Boland, Yuan-Heng Chao, Y. Suzuki, and Y. C. Tai. Micro electret power generator. In *The Sixteenth Annual International Conference on Micro Electro Mechanical Systems, 2003. MEMS-03 Kyoto. IEEE*, pages 538–541, Jan 2003.
- [Ber76] J.C. Berney. Watch movement driven by a spring and regulated by an electronic circuit, 1976. US Patent 3,937,001.
- [BF07] J.J. Born and P.A. Farine. Timepiece with a mechanical movement coupled to an electronic regulator mechanism, May 30 2007. EP Patent 1,521,141.

Bibliography

- [BH98] J.L. Béguin and P. Haefeli. Means for coupling a mechanical energy source with an electric generator in a time piece, July 8 1998. EP Patent 0,681,228.
- [BKB⁺09] V. Badilita, K. Kratt, T. Burger, J. G. Korvink, and U. Wallrabe. 3d high aspect ratio, mems integrated micro-solenoids and helmholtz micro-coils. In *TRANSDUCERS 2009 - 2009 International Solid-State Sensors, Actuators and Microsystems Conference*, pages 1106–1109, June 2009.
- [BL59] G. E. P. Box and H. L. Lucas. Design of experiments in non-linear situations. *Biometrika*, 46(1/2):77–90, 1959.
- [BL09] M. A. Batdorff and J. H. Lumkes. High-fidelity magnetic equivalent circuit model for an axisymmetric electromagnetic actuator. *IEEE Transactions on Magnetics*, 45(8):3064–3072, Aug 2009.
- [BLM⁺02] A. A. Busnaina, Hong Lin, N. Moumen, Jiang wei Feng, and J. Taylor. Particle adhesion and removal mechanisms in post-cmp cleaning processes. *IEEE Transactions on Semiconductor Manufacturing*, 15(4):374–382, Nov 2002.
- [BPF10] A. Borisavljevic, H. Polinder, and J. A. Ferreira. On the speed limits of permanent-magnet machines. *IEEE Transactions on Industrial Electronics*, 57(1):220–227, Jan 2010.
- [BTK⁺04] S P Beeby, M J Tudor, E Koukharenko, N M White, T O'Donnell, C Saha, S Kulkarni, and S Roy. Micromachined silicon generator for harvesting power from vibrations. pages 104–107, 2004. Event Dates: 28-30th November 2004.
- [Car06] P. Carazzetti. *High Quality Micromachined Inductors for Integrated Communication Systems*. PhD thesis, 2006.
- [Cha83] Jean Chatelain. *Machines électriques*. Presses Polytechniques romandes, 1983.
- [Che15] Yifang Chen. Nanofabrication by electron beam lithography and its applications: A review. *Microelectronic Engineering*, 135:57 – 72, 2015.
- [CSJL13] Jang-Young Choi, Hyeon-Jae Shin, Seok-Myeong Jang, and Sung-Ho Lee. Torque analysis and measurements of cylindrical air-gap synchronous permanent magnet couplings based on analytical magnetic field calculations. *Magnetics, IEEE Transactions on*, 49(7):3921–3924, July 2013.
- [CST06] J. Cale, S. D. Sudhoff, and Li-Quan Tan. Accurately modeling ei core inductors using a high-fidelity magnetic equivalent circuit approach. *IEEE Transactions on Magnetics*, 42(1):40–46, Jan 2006.

- [DAZ⁺05] S. Das, D. P. Arnold, I. Zana, J. W. Park, J. H. Lang, and M. G. Allen. Multi-watt electric power from a microfabricated permanent-magnet generator. In *18th IEEE International Conference on Micro Electro Mechanical Systems, 2005. MEMS 2005.*, pages 287–290, Jan 2005.
- [DBP17] B. Dehez, F. Baudart, and Y. Perriard. Analysis of a new topology of flexible pcb winding for slotless bldc machines. In *2017 IEEE International Electric Machines and Drives Conference (IEMDC)*, pages 1–8, May 2017.
- [DJJJ⁺05] Ghislain Despesse, Thomas Jager, Chaillout Jean-Jacques, Jean-Michel Léger, Andrea Vassilev, Skandar Basrour, and Benoit Charlot. Fabrication and characterization of high damping electrostatic micro devices for vibration energy scavenging. *Proc. Design, Test, Integration and Packaging of MEMS and MOEMS*, pages 386–390, June 2005. ISBN:2-84813-057-1.
- [DMLP13] A. Danisi, A. Masi, R. Losito, and Y. Perriard. Modeling of high-frequency electromagnetic effects on an ironless inductive position sensor. *IEEE Sensors Journal*, 13(12):4663–4670, Dec 2013.
- [Dow66] P.L. Dowell. Effects of eddy currents in transformer windings. *Electrical Engineers, Proceedings of the Institution of*, 113(8):1387–1394, August 1966.
- [EhGJW⁺01] M. El-hami, P. Glynn-Jones, N.M. White, M. Hill, S. Beeby, E. James, A.D. Brown, and J.N. Ross. Design and fabrication of a new vibration-based electromechanical power generator. *Sensors and Actuators A: Physical*, 92(1):335 – 342, 2001. Selected Papers for Eurosensors XIV.
- [enc06] *The New Encyclopedia Britannica (32 Volume Set) (2007)*. Encyclopedia Britannica, 2006.
- [EPCLALLC05] R. Escarela-Perez, E. Campero-Littlewood, M. A. Arjona-Lopez, and A. Laureano-Cruces. Comparison of two techniques for two-dimensional finite-element inductance computation of electrical machines. *Electric Power Applications, IEE Proceedings -*, 152(4):855–861, July 2005.
- [ER06] T.G. Engel and S.N. Rohe. A comparison of single-layer coaxial coil mutual inductance calculations using finite-element and tabulated methods. *Magnetics, IEEE Transactions on*, 42(9):2159–2163, Sept 2006.
- [ETWW11] C Eichhorn, R Tchagsim, N Wilhelm, and P Woias. A smart and self-sufficient frequency tunable vibration energy harvester. *Journal of Micromechanics and Microengineering*, 21(10):104003, 2011.

Bibliography

- [FC16] N. Felix and D. Corliss. Euv patterning successes and frontiers, 2016.
- [Fer90] J. A. Ferreira. Appropriate modelling of conductive losses in the design of magnetic components. In *21st Annual IEEE Conference on Power Electronics Specialists*, pages 780–785, 1990.
- [Fer92] J. A. Ferreira. Analytical computation of ac resistance of round and rectangular litz wire windings. *IEE Proceedings B - Electric Power Applications*, 139(1):21–25, Jan 1992.
- [Fer94] J. A. Ferreira. Improved analytical modeling of conductive losses in magnetic components. *IEEE Transactions on Power Electronics*, 9(1):127–131, Jan 1994.
- [GCS⁺93] H. Guckel, T. R. Christenson, K. J. Skrobis, T. S. Jung, J. Klein, K. V. Hartojo, and I. Widjaja. A first functional current excited planar rotational magnetic micromotor. In *[1993] Proceedings IEEE Micro Electro Mechanical Systems*, pages 7–11, Feb 1993.
- [Gen05] Giancarlo Genta. *Dynamics of Rotating Systems*. Springer, 2005.
- [Gie08] J. F. Gieras. *Advancements in Electric Machines (Power Systems)*. Springer Netherlands, 2008.
- [Giu09] Victor Giurgiutiu. *Micromechatronics : modeling, analysis, and design with MATLAB*. CRC Press, Boca Raton, 2009.
- [GL07] L. Gu and X. Li. High-q solenoid inductors with a cmos-compatible concave-suspending mems process. *Journal of Microelectromechanical Systems*, 16(5):1162–1172, Oct 2007.
- [GNV09] L. Gammaitoni, I. Neri, and H. Vocca. Nonlinear oscillators for vibration energy harvesting. *Applied Physics Letters*, 94(16):164102, 2009.
- [Gre74] H. Greenhouse. Design of planar rectangular microelectronic inductors. *IEEE Transactions on Parts, Hybrids, and Packaging*, 10(2):101–109, Jun 1974.
- [Gri17] Daniel Grivon. *Design, Modelling and Sensing Possibilities of Magneto-Rheological Based Devices*. PhD thesis, STI, Lausanne, 2017.
- [Gro46] F.W. Grover. *Inductance Calculations*. Van Nostrand, Princeton, N.J., 1946.
- [GSP⁺09] D. S. Gardner, G. Schrom, F. Paillet, B. Jamieson, T. Karnik, and S. Borkar. Review of on-chip inductor structures with magnetic films. *IEEE Transactions on Magnetics*, 45(10):4760–4766, Oct 2009.

- [Hea02] M. V. Headrick. Origin and evolution of the anchor clock escapement. *IEEE Control Systems*, 22(2):41–52, Apr 2002.
- [HJA08] F. Herrault, C. H. Ji, and M. G. Allen. Ultraminiaturized high-speed permanent-magnet generators for milliwatt-level power generation. *Journal of Microelectromechanical Systems*, 17(6):1376–1387, Dec 2008.
- [HK00] T. Hara and J. Kitahara. Electronic watch, September 19 2000. US Patent 6,120,177.
- [HMCM15] T. Heimfarth, M. Z. Mielli, M. N. P. Carreño, and M. Mulato. Miniature planar fluxgate magnetic sensors using a single layer of coils. *IEEE Sensors Journal*, 15(4):2365–2369, April 2015.
- [IDL⁺09] S. Iwasaki, R. P. Deodhar, Y. Liu, A. Pride, Z. Q. Zhu, and J. J. Bremner. Influence of pwm on the proximity loss in permanent-magnet brushless ac machines. *IEEE Transactions on Industry Applications*, 45(4):1359–1367, July 2009.
- [JKHS95] Ajay Jain, T.T. Kodas, and M.J. Hampden-Smith. Thermal dry-etching of copper using hydrogen peroxide and hexafluoroacetylacetone. *Thin Solid Films*, 269(1):51 – 56, 1995.
- [JKK12] S. E. Jo, M. S. Kim, and Y. J. Kim. Electromagnetic human vibration energy harvester comprising planar coils. *Electronics Letters*, 48(14):874–875, July 2012.
- [JKKCKH⁺12] Hong Jin Kim, Jae Kwang Choi, Myung Ki Hong, Kuntack Lee, and Yongsun Ko. Contact behavior and chemical mechanical polishing (cmp) performance of hole-type polishing pad. 1:P204–P209, 08 2012.
- [JLI⁺15] P. Janphuang, R. A. Lockhart, D. Isarakorn, S. Henein, D. Briand, and N. F. de Rooij. Harvesting energy from a rotating gear using an afm-like mems piezoelectric frequency up-converting energy harvester. *Journal of Microelectromechanical Systems*, 24(3):742–754, June 2015.
- [JPB⁺16] N. Jackson, F. J. Pedrosa, A. Bollero, A. Mathewson, and O. Z. Olszewski. Integration of thick-film permanent magnets for mems applications. *Journal of Microelectromechanical Systems*, 25(4):716–724, Aug 2016.
- [Juf95] Marcel Jufer. *Electromécanique*. Presses Polytechniques romandes, 1995.
- [JW78] O. D. Jefimenko and D. K. Walker. Electrostatic current generator having a disk electret as an active element. *IEEE Transactions on Industry Applications*, IA-14(6):537–540, Nov 1978.

Bibliography

- [KALS11] Z. Kolondzovski, A. Arkkio, J. Larjola, and P. Sallinen. Power limits of high-speed permanent-magnet electrical machines for compressor applications. *IEEE Transactions on Energy Conversion*, 26(1):73–82, March 2011.
- [KKPG98] J. Kymissis, C. Kendall, J. Paradiso, and N. Gershenfeld. Parasitic power harvesting in shoes. In *Digest of Papers. Second International Symposium on Wearable Computers (Cat. No.98EX215)*, pages 132–139, Oct 1998.
- [KL00] Yue Kuo and Sangheon Lee. A novel plasma-based copper dry etching method. *Japanese Journal of Applied Physics*, 39(3A):L188, 2000.
- [KLD15] S. Khan, L. Lorenzelli, and R. S. Dahiya. Technologies for printing sensors and electronics over large flexible substrates: A review. *IEEE Sensors Journal*, 15(6):3164–3185, June 2015.
- [KMP10] C. Koechli, S. Merzaghi, and Y. Perriard. Modeling and design of a hybrid mems motor. In *Electrical Machines (ICEM), 2010 XIX International Conference on*, pages 1–6, Sept 2010.
- [KP13] C. Koechli and Y. Perriard. Analytical model for slotless permanent magnet axial flux motors. In *Electric Machines Drives Conference (IEMDC), 2013 IEEE International*, pages 788–792, May 2013.
- [KSY⁺07] T. Kaho, M. Sasaki, Y. Yamaguchi, K. Nishikawa, and K. Uehara. Miniaturized multilayer inductors on gaas three-dimensional mmic. In *Microwave Conference, 2007. KJMW 2007. Korea-Japan*, pages 149–152, Nov 2007.
- [LA99] T. M. Liakopoulos and C. H. Ahn. 3-d microfabricated toroidal planar inductors with different magnetic core schemes for mems and power electronic applications. *IEEE Transactions on Magnetics*, 35(5):3679–3681, Sep 1999.
- [LBF⁺13] W Q Liu, A Badel, F Formosa, Y P Wu, and A Agbossou. Novel piezoelectric bistable oscillator architecture for wideband vibration energy harvesting. *Smart Materials and Structures*, 22(3):035013, 2013.
- [LC97] J. R. Long and M. A. Copeland. The modeling, characterization, and design of monolithic inductors for silicon rf ic's. *IEEE Journal of Solid-State Circuits*, 32(3):357–369, Mar 1997.
- [LFLT16] K. Liu, X. Fu, M. Lin, and L. Tai. Ac copper losses analysis of the ironless brushless dc motor used in a flywheel energy storage system. *IEEE Transactions on Applied Superconductivity*, 26(7):1–5, Oct 2016.

- [LPC⁺98] J. W. Lee, Y. D. Park, J. R. Childress, S. J. Pearton, F. Sharifi, and F. Ren. Copper dry etching with Cl₂/Ar plasma chemistry. *Journal of The Electrochemical Society*, 145(7):2585–2589, 1998.
- [Mad02] Marc J. Madou. *Fundamentals of Microfabrication: The Science of Miniaturization, Second Edition*. CRC Press, 2002.
- [MBC⁺15] Sun Mingbin, Gao Baohong, Wang Chenwei, Miao Yingxin, Duan Bo, and Tan Baimei. Non-ionic surfactant on particles removal in post-cmp cleaning. *Journal of Semiconductors*, 36(2):026002, 2015.
- [MdmHBL99] S.S. Mohan, M. del Mar Hershenson, S.P. Boyd, and T.H. Lee. Simple accurate expressions for planar spiral inductances. *Solid-State Circuits, IEEE Journal of*, 34(10):1419–1424, Oct 1999.
- [MET⁺10] Yasufumi Matsumura, Yasushi Enomoto, Takaaki Tsuruoka, Kensuke Akamatsu, and Hidemi Nawafune. Fabrication of copper damascene patterns on polyimide using direct metallization on trench templates generated by imprint lithography. *Langmuir*, 26(14):12448–12454, jul 2010.
- [MKP09] S. Merzaghi, C. Koechli, and Y. Perriard. Development of a hybrid mems bldc micromotor. In *Energy Conversion Congress and Exposition, 2009. ECCE 2009. IEEE*, pages 3595–3601, Sept 2009.
- [MKP11] S. Merzaghi, C. Koechli, and Y. Perriard. Development of a hybrid mems bldc micromotor. *IEEE Transactions on Industry Applications*, 47(1):3–11, Jan 2011.
- [MMA⁺01] S. Meninger, J. O. Mur-Miranda, R. Amirtharajah, A. Chandrakasan, and J. H. Lang. Vibration-to-electric energy conversion. *IEEE Transactions on Very Large Scale Integration (VLSI) Systems*, 9(1):64–76, Feb 2001.
- [MMST14] W. Meier, A. MICHALET, K. Straumann, and D. Taghezout. Movement for mechanical chronograph with quartz regulator, July 17 2014. WO Patent App. PCT/EP2013/069,402.
- [MPG⁺14] M. A. Migliorato, J. Pal, R. Garg, G. Tse, H. Y.S. Al-Zahrani, U. Monteverde, S. Tomić, C-K. Li, Y-R. Wu, B. G. Crutchley, I. P. Marko, and S. J. Sweeney. A review of non linear piezoelectricity in semiconductors. *AIP Conference Proceedings*, 1590(1):32–41, 2014.
- [MRW⁺15] E. Macrelli, A. Romani, N. Wang, S. Roy, M. Hayes, R. P. Paganelli, C. Ó Mathúna, and M. Tartagni. Modeling, design, and fabrication of high-inductance bond wire microtransformers with toroidal ferrite core. *IEEE Transactions on Power Electronics*, 30(10):5724–5737, Oct 2015.

Bibliography

- [MS98] C. Mencuccini and V. Silvestrini. *Fisica 2. Elettromagnetismo-ottica. Corso di fisica per le facoltà scientifiche. Con esempi ed esercizi*. Argomenti di fisica. Liguori, 1998.
- [MSS86] J. D. McBrayer, R. M. Swanson, and T. W. Sigmon. Diffusion of metals in silicon dioxide. *Journal of The Electrochemical Society*, 133(6):1242–1246, 1986.
- [MYR⁺08] P. D. Mitcheson, E. M. Yeatman, G. K. Rao, A. S. Holmes, and T. C. Green. Energy harvesting from human and machine motion for wireless electronic devices. *Proceedings of the IEEE*, 96(9):1457–1486, Sept 2008.
- [Nye85] J. F. Nye. *Physical Properties of Crystals: Their Representation by Tensors and Matrices*. Oxford University Press, 1985.
- [OF86] Fumio Ohuchi and Steven Freilich. “metal polyimide interface: A titanium reaction mechanism”. 4:1039 – 1045, 06 1986.
- [OF88] F.S. Ohuchi and S.C. Freilich. Summary Abstract: Ti as a diffusion barrier between Cu and polyimide. *Journal of Vacuum Science Technology*, 6:1004–1006, May 1988.
- [PD13] M. Popescu and D. G. Dorrell. Proximity losses in the windings of high speed brushless permanent magnet ac motors with single tooth windings and parallel paths. *IEEE Transactions on Magnetics*, 49(7):3913–3916, July 2013.
- [per03] Structural and magnetic properties of ndfeb thin films sputtered on w underlayers. *Journal of Magnetism and Magnetic Materials*, 267(3):341 – 346, 2003.
- [PHB⁺05] M. B. Pisani, C. Hibert, D. Bouvet, C. Dehollain, and A. M. Ionescu. Fabrication and electrical characterization of high performance copper/polyimide inductors. In *Research in Microelectronics and Electronics, 2005 PhD*, volume 1, pages 185–188 vol.1, July 2005.
- [PKVC12] Jin-Goo Park, Tae-Young Kwon, R Prasanna Venkatesh, and Byoung-Jun Cho. Cmp defects; their detection and analysis on root causes. *ECS Transactions*, 44(1):559–564, 2012.
- [PKW⁺88] E. Pettenpaul, H. Kapusta, A. Weisgerber, H. Mampe, J. Luginsland, and I. Wolff. Cad models of lumped elements on gaas up to 18 ghz. *IEEE Transactions on Microwave Theory and Techniques*, 36(2):294–304, Feb 1988.

- [PM08] Christian Peters and Yiannos Manoli. Inductance calculation of planar multi-layer and multi-wire coils: An analytical approach. *Sensors and Actuators A: Physical*, 145-146(0):394 – 404, 2008.
- [Pol13] J. Poliakine. Génératrice MEMS pour augmenter la précision d’une montre mécanique: pré-étude. *EPFL Master Project*, 2013.
- [PP99] Zoya Popovic and Branko D. Popovic. *Introductory Electromagnetics*. Prentice Hall, 1999.
- [PP13] Luc Pronzato and Andrej Pázman. *Design of Experiments in Nonlinear Models: 212 (Lecture Notes in Statistics)*. Springer New York, 2013.
- [Pre06] Andre Preumont. *Mechatronics : dynamics of electromechanical and piezoelectric systems*. Springer, Dordrecht, 2006.
- [PXP11] A. Pagnetti, A. Xemard, F. Paladian, and C. A. Nucci. Evaluation of the impact of proximity effect in the calculation of the internal impedance of cylindrical conductors. In *General Assembly and Scientific Symposium, 2011 XXXth URSI*, pages 1–4, Aug 2011.
- [PYH13] P. Pillatsch, E. M. Yeatman, and A. S. Holmes. A model for magnetic plucking of piezoelectric beams in energy harvesters. In *2013 Transducers Eurosensors XXVII: The 17th International Conference on Solid-State Sensors, Actuators and Microsystems (TRANSDUCERS EUROSENSORS XXVII)*, pages 1364–1367, June 2013.
- [RAS⁺95] Sudipto R. Roy, Iqbal Ali, Greg Shinn, Nobuyuki Furusawa, Raj Shah, Shelley Peterman, Kevin Witt, Steve Eastman, and Promod Kumar. Postchemical mechanical planarization cleanup process for interlayer dielectric films. *Journal of The Electrochemical Society*, 142(1):216–226, 1995.
- [RBSB17] J. Rolland, H. Walter-Le Berre, A. Saulot, and Y. Berthier. Instrumentation of a contact with the finite element method and experimental coupling: The case of the swiss lever escapement mechanism. *Tribology International*, 111(Supplement C):176 – 183, 2017.
- [Rob04] Karl Robinson. *Fundamentals of CMP Slurry*, pages 215–249. Springer Berlin Heidelberg, Berlin, Heidelberg, 2004.
- [Rot41] H.C. Roters. *Electromagnetic Devices*. Wiley, 1941.
- [RW04] S. Roundy and P. K. Wright. A piezoelectric vibration based generator for wireless electronics. *Smart Materials and Structures*, 13(5):1131–1142, 10 2004.

Bibliography

- [SBS12] G. Despesse S. Boisseau and B. Ahmed Seddik. *Electrostatic Conversion for Vibration Energy Harvesting, Small-scale Energy Harvesting*. InTech, 2012.
- [SC01] Christoph Steinbruchel and Barry Chin. *Copper Interconnect Technology (SPIE Tutorial Texts in Optical Engineering Vol. TT46)*. SPIE Publications, 2001.
- [Sch14] Mordechay Schlesinger. *Modern Electroplating*. Wiley, 2014.
- [SGA01] D. J. Sadler, S. Gupta, and C. H. Ahn. Micromachined spiral inductors using uv-liga techniques. *IEEE Transactions on Magnetics*, 37(4):2897–2899, Jul 2001.
- [Sha03] Lawrence Shampine. *Solving ODEs with MATLAB*. Cambridge University Press, Cambridge New York, 2003.
- [Sil98] Jerome P. Silverman. Challenges and progress in x-ray lithography. *Journal of Vacuum Science & Technology B: Microelectronics and Nanometer Structures*, 16(6):3137, nov 1998.
- [SKN01] E. Shimizu, K. Koike, and H. Nakamura. Electronically controlled, mechanical timepiece and control method for the same, November 6 2001. US Patent 6,314,059.
- [SM05] J. Sun and J. Miao. High performance MEMS inductors fabricated on localised and planar thick SiO₂ layer. *Electronics Letters*, 41(7):446, 2005.
- [SP01] Nathan S. Shenck and Joseph A. Paradiso. Energy scavenging with shoe-mounted piezoelectrics. *IEEE Micro*, 21(3):30–42, May 2001.
- [SSCM98] K. Sivasubramaniam, S. Salon, M. V K Chari, and I. D. Mayergoyz. Modified scalar potential solution for three-dimensional magnetostatic problems. *Journal of Applied Physics*, 83(11):6347–6349, 1998.
- [Ste06] Igor Stefanini. *Méthodologie de conception et optimisation d'actionneurs intégrés sans fer*. PhD thesis, STI, Lausanne, 2006.
- [Tad86] Y. Tada. Theoretical characteristics of generalized electret generator, using polymer film electrets. *IEEE Transactions on Electrical Insulation*, EI-21(3):457–464, June 1986.
- [TKK⁺02] R. Tashiro, N. Kabei, K. Katayama, E. Tsuboi, and K. Tsuchiya. Development of an electrostatic generator for a cardiac pacemaker that harnesses the ventricular wall motion. *Journal of Artificial Organs*, 5(4):0239–0245, Dec 2002.

- [TT89] X.M. Tu and D. Taghezout. Convertisseur d'énergie mécanique en énergie électrique, October 18 1989. EP Patent 0,239,820.
- [TWL02] Chih-Chun Tang, Chia-Hsin Wu, and Shen-Iuan Liu. Miniature 3-d inductors in standard cmos process. *IEEE Journal of Solid-State Circuits*, 37(4):471–480, Apr 2002.
- [TZJ09] A. S. Thomas, Z. Q. Zhu, and G. W. Jewell. Proximity loss study in high speed flux-switching permanent magnet machine. *IEEE Transactions on Magnetism*, 45(10):4748–4751, Oct 2009.
- [Ueh04] Minoru Uehara. Microstructure and permanent magnet properties of a perpendicular anisotropic ndfeb/ta multilayered thin film prepared by magnetron sputtering. *Journal of Magnetism and Magnetic Materials*, 284(Supplement C):281 – 286, 2004.
- [UKN⁺16] N. Uzhegov, E. Kurvinen, J. Nerg, J. Pyrhönen, J. T. Sopanen, and S. Shirinskii. Multidisciplinary design process of a 6-slot 2-pole high-speed permanent-magnet synchronous machine. *IEEE Transactions on Industrial Electronics*, 63(2):784–795, Feb 2016.
- [VC14] V. N. R. Vanukuru and A. Chakravorty. High density solenoidal series pair symmetric inductors and transformers. *IEEE Transactions on Electron Devices*, 61(7):2503–2508, July 2014.
- [Whe28] H. A. Wheeler. Simple inductance formulas for radio coils. *Proceedings of the Institute of Radio Engineers*, 16(10):1398–1400, Oct 1928.
- [Wol90] Stanley Wolf. *Silicon Processing for the VLSI Era, Vol. 2: Process Integration*. Lattice Press, 1990.
- [YRL⁺96] C. P. Yue, C. Ryu, J. Lau, T. H. Lee, and S. S. Wong. A physical model for planar spiral inductors on silicon. In *International Electron Devices Meeting. Technical Digest*, pages 155–158, Dec 1996.
- [YW00] C. P. Yue and S. S. Wong. Physical modeling of spiral inductors on silicon. *IEEE Transactions on Electron Devices*, 47(3):560–568, Mar 2000.
- [Zha11] Hui Zhang. Power generation transducer from magnetostrictive materials. *Applied Physics Letters*, 98(23):232505, 2011.

Curriculum Vitae

Jasha POLIAKINE

Born July 29, 1986

Italian Citizen

jasha.poliakine@gmail.com

Study and professional experience

- 2013 - Teaching assistant and PhD student at the Integrated Actuators Laboratory (LAI), École Polytechnique fédérale de Lausanne, Switzerland.
2017
- 2011 - Master of Science in Nanotechnology Engineering, Sapienza University
2013 of Rome, Italy
- 2006 - Bachelor of Science in Mechanical Engineering, Sapienza University of
2010 Rome, Italy.

Publications and Patents

- J. Poliakine, Y. Civet and Y. Perriard, *Modeling, Design, and Manufacturing of Microfabricated Coils With High Inductance Density*, Journal of Microelectromechanical Systems, 2017
- J. Poliakine, Y. Civet and Y. Perriard, *Microfabricated planar coils with high turns density: Design and manufacturing*, 19th International Conference on Electrical Machines and Systems (ICEMS), 2016
- J. Poliakine, Y. Civet and Y. Perriard, *Design and Manufacturing of High Inductance Planar Coils for Small Scale Sensing Applications*, Proceedings of the 30th anniversary Eurosensors Conference – Eurosensors 2016
- J. Poliakine, Y. Civet and Y. Perriard, *Modeling and characterization of a MEMS synchronous generator*, 17th International Conference on Electrical Machines and Systems (ICEMS), 2014

Curriculum Vitae

- J. Poliakine, J. C. Fiaccabrino, J. Zürcher, Y. Civet, Y. Perriard, *Microgénératrice pour pièce d'horlogerie et procédé de fabrication de microgénératrice pour pièce d'horlogerie*, European patent, 17174542.5 - 1559

